UNDERSTANDING SEASONAL CLIMATE PREDICTABILITY IN THE ATLANTIC SECTOR

A Dissertation

by

MARCELO BARREIRO

Submitted to the Office of Graduate Studies of
Texas A&M University
in partial fulfillment of the requirements for the degree of

DOCTOR OF PHILOSOPHY

December 2003

Major Subject: Oceanography

UNDERSTANDING SEASONAL CLIMATE PREDICTABILITY IN THE ATLANTIC SECTOR

A Dissertation

by

MARCELO BARREIRO

Submitted to Texas A&M University
in partial fulfillment of the requirements
for the degree of

DOCTOR OF PHILOSOPHY

Approved as to style and content by:

Ping Chang (Chair of Committee)	Benjamin S. Giese (Member)
Gerald North (Member)	R. Lee Panetta (Member)
R. Saravanan (Member)	Wilford Gardner (Head of Department)

December 2003

Major Subject: Oceanography

ABSTRACT

Understanding Seasonal Climate Predictability
in the Atlantic Sector. (December 2003)
Marcelo Barreiro, B.S., Universidad de la República, Uruguay;
M.S., Universidad de la República, Uruguay
Chair of Advisory Committee: Dr. Ping Chang

This dissertation aims at understanding ocean-atmosphere interactions in the Atlantic basin, and how this coupling may lead to increased climate predictability on seasonal-to-interannual time scales. Two regions are studied: the South Atlantic convergence zone (SACZ), and the tropical Atlantic.

We studied the SACZ during austral summer and separated its variability into forced and internal components. This was done by applying a signal-to-noise optimization procedure to an ensemble of integrations of the NCAR Community Climate Model (CCM3) forced with observed Sea Surface Temperature (SST). The analysis yielded two dominant responses: (1) a response to local Atlantic SST consisting of a dipole-like structure in precipitation close to the coast of South America; (2) a response to Pacific SST which manifests mainly in the upper-level circulation consisting of a northeastward shift of the SACZ during El Niño events. The land portion of the SACZ was found to be primarily dominated by internal variability, thereby having limited potential predictability at seasonal time scales.

We studied two aspects of tropical Atlantic Variability (TAV). First, we investigated the effect of extratropical variability on the gradient mode. We found that the intensive Southern Hemisphere (SH) winter variability can play a pre-conditioning

role in the onset of the interhemispheric anomalies in the deep tropics during boreal spring. This SH influence on TAV is contrasted with its northern counterpart that primarily comes from the North Atlantic Oscillation during boreal winter.

Second, we explored the importance of ocean dynamics in the predictability of TAV. We used the CCM3 coupled to a slab ocean as a tier-one prediction system. The ocean processes are included as a statistical correction that parameterizes the heat transport due to anomalous linear ocean dynamics. The role of ocean dynamics was studied by comparing prediction runs with and without the correction. We showed that in the corrected region the corrected model outperformed the non-corrected one particularly at long lead times. Furthermore, when the model was initialized with global initial conditions, tropical Atlantic SST anomalies are skillfully predicted for lead times of up to six months. As result, the corrected model showed high skill in predicting rainfall in the ITCZ during boreal spring.

To Paula

ACKNOWLEDGMENTS

I would like to thank my advisor, Dr. Ping Chang, for his expert guidance and kindness during the course of my Ph.D. study. He always kept the door open to discuss any ideas or troubles that I had in my research, and made working with him very comfortable and a most valuable experience.

I would like to thank Dr. R. Saravanan for serving on my committee and inviting me to work at the National Center for Atmospheric Research for six months. The time I spent at the NCAR greatly enhanced my education.

I would also like to thank Dr. Benjamin Giese, Dr. Gerald North and Dr. Lee Panetta for serving on my committee. Their suggestions and comments greatly improved the dissertation.

Late and foremost, I want to thank my mother Nerina, my sister Laura, and my brother Diego for their encouragement and unconditional support from the other side of the equator during this five-year journey called Ph.D.

TABLE OF CONTENTS

CHAPTER Page

Page

LIST OF TABLES

LIST OF FIGURES

FIGURE Page

FIGURE Page

FIGURE Page

FIGURE Page

FIGURE Page

FIGURE Page

FIGURE Page

CHAPTER I

INTRODUCTION

A. Motivation

Climate directly affects human socio-economic activities. In order to exploit beneficial climate variations and mitigate the effects of harmful ones we must first understand how the climate system works and then be able to predict it [*NRC*, 1998]. The overall goal of this work is the understanding of the predictable part (as opposed to the stochastic part) of climate in the Atlantic basin to help improving climate predictions on seasonal-to-interannual time scales.

Since the pioneering work of *Lorenz* [1963] it has been shown that the equations for weather forecasting represent a forced dissipative nonlinear dynamical system, and therefore infinitesimally small errors in the specification of the initial state of the atmosphere will grow exponentially, limiting the predictability of weather to about two weeks. Climate prediction circumvents this limit by forecasting the statistics of weather, that is, the climate. In certain regions of the globe weather regimes are strongly influenced by "external factors" through, for example, boundary conditions like sea surface temperature (SST), soil moisture, or land and sea ice extent. The fact that these external factors, such as SST, have much longer "memory" (due to slow adjustment of the oceans in this case) gives rise to the possibility of predicting weather statistics at a much longer time scale than the two-week limit imposed by the "internal dynamics" of the atmosphere. In the language of dynamical systems, these "external factors" alter the likelihood of residence of the orbit in different parts of the phase space, thus enabling a statistical forecast of the seasonal-to-interannual

---

The journal model is *Journal of Geophysical Research*.

climate mean conditions.

SST anomalies have been recognized as one of the most important external factors influencing the atmosphere. Accordingly, to predict climate we need to understand: (1) the genesis and evolution of SST anomalies, and (2) the atmospheric response to SST anomalies.

The simplest theory of SST variations is that of *Hasselmann* [1976]. He demonstrated that the low-frequency variability of the SST could be thought as the integrated response of the ocean to high-frequency stochastic atmospheric forcing. If this mechanism were the only operating, the time scale of predictability of the SST would be given by its autocorrelation (given by ocean's thermal inertia and the heat flux damping), and the best prediction would be a damped persistence forecast. This paradigm has been successfully used to describe the low-frequency variability of SST in the extratropics [*Frankignoul and Hasselmann*, 1977]. Moreover, it has been shown that in the extratropics the ocean feeds back to the atmosphere enhancing the low-frequency variance of the atmospheric internal variability without affecting atmospheric dynamics [*Barsugli and Battisti*, 1998]. To date, there has been no clear demonstration of significant air-sea coupling in the extratropics beyond this local passive thermodynamic feedback.

In the tropics ocean-atmosphere interaction is much stronger than in the extratropics and true coupled modes can develop. The existence of these coupled modes, which are partially predictable, greatly helps the feasibility of seasonal-to-interannual climate prediction. A typical example of such a mode is the El Niño-Southern Oscillation (ENSO) which involves a dynamical coupling between the wind stress and the ocean's thermocline on interannual time scales [*Neelin et al.*, 1998]. The SST anomaly associated with these coupled modes changes convection patterns re-distributing the release of latent heating in the tropical atmosphere. Consequently, climate anomalies

(or signals) are not only created locally, but also on remote locations through, for instance, the excitation of anomalous wave trains [*Hoskins and Karoly*, 1981]. These atmospheric anomalies can in turn influence the evolution of SSTs in other basins, which may also force the atmosphere. Therefore, tropical ocean-atmosphere interaction allows the prediction of SSTs beyond the time scale given by the ocean's thermal inertia. Thus, understanding the processes involved in the coupling, the evolution of associated SST anomalies and their influence on the atmosphere is a central focus of climate research.

Until very recently, most research efforts have been focused on the tropical Pacific and ENSO-related climate predictability. This research has demonstrated that ENSO-related SST anomalies can be predicted several seasons in advance using either coupled dynamical models or statistical models, and these SST predictions can improve seasonal climate forecasts in certain regions of the globe (e.g. *Cane et al.* [1986], *Barnston and Coauthors* [1994], for a review see *Goddard et al.* [2001]). Based on these successes, a number of national and international programs have been developed to seek improving and extending seasonal-to-interannual climate predictability from its present tropical Pacific and ENSO-centric basis to the global domain. This study aims at understanding seasonal predictability in the Atlantic sector as defined by (75°W-30°E, 50°S-30°N). This region is host to a very large population whose wellbeing and economic activity is directly influenced by rainfall variability (Figure 1). We focus our study on ocean-atmosphere interaction in two main areas: the South Atlantic convergence zone (SACZ), and the Tropical Atlantic region (between about 30°S-30°N).

The SACZ appears in the austral summer as a diagonal band of convective precipitation extending from the Amazon basin toward the southeast reaching the subtropical South Atlantic. It modulates the intensity and location of the summer rain in the

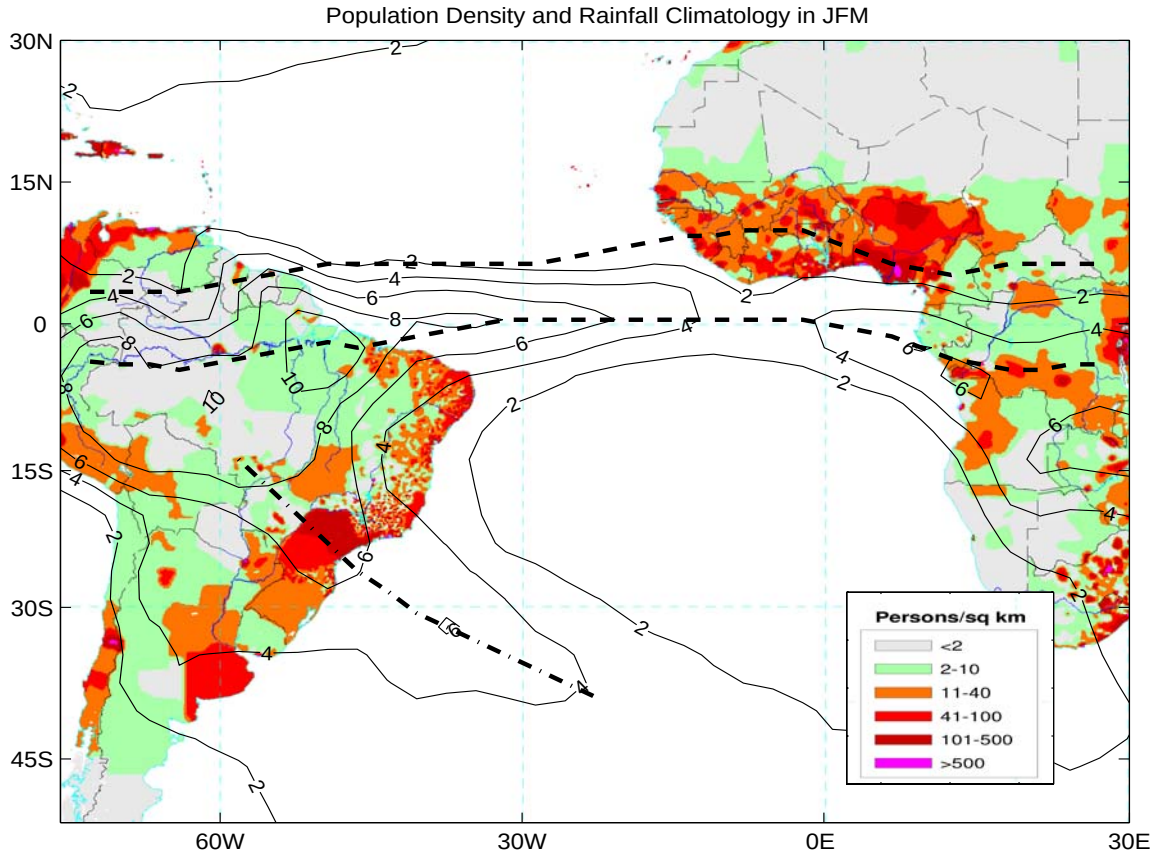

Fig. 1. Map of population density, overlaid by contours of rainfall climatology in season January-February-March. The main axis of the SACZ is indicated by a thick dashed-dotted line. Thick dashed lines indicate the northern (July-August) and southern (March-April) limits of ITCZ's annual migration. Population density data are from *Tobler et al.* [1995], http://www.nrcs.usda.gov/technical/-worldsoils/mapindx/popden.html

very densely populated area of southeastern Brazil and neighboring countries (Figure 1). Variations of the SACZ have also been connected to changes in the Plata River Basin [*Robertson and Mechoso*, 2000]. This basin is critical to local economies generating about 70% of the total Gross National Product of Argentina, Brazil, Bolivia, Paraguay and Uruguay. Thus, advances in understanding of SACZ variability and predictability will greatly benefit these countries through improved decision-making.

The socio-economic importance of Tropical Atlantic Variability (TAV), which refers to substantial variations on interannual and decadal time scales in tropical Atlantic SST with direct impact in the climates of Africa and Americas, has been recognized by the Climate Variability program (CLIVAR). The Intertropical Convergence Zone (ITCZ), a band of surface wind convergence and strong convective activity, dominates climatic variability in this region. The ITCZ is close to be zonally symmetric and moves latitudinally with seasons being closer to the equator in March-April and at about 7°N during July-August (Figure 1). Interannual changes in position and intensity of the ITCZ largely determines the variability of precipitation during the rainy seasons of Northeast Brazil [*Hastenrath and Heller*, 1977], and the Sahel [*Lamb*, 1978]. In turn, the ITCZ is strongly coupled to the cross-equatorial gradient of SST, leading to an ocean-atmosphere coupled mode of variability called the "gradient mode" [*Nobre and Shukla*, 1996; *Chang et al.*, 1997], which peaks during boreal spring. The Atlantic basin also exhibits variability akin to ENSO that reaches maximum strength during boreal summer [*Zebiak*, 1993; *Carton and Huang*, 1994]. This mode is sometimes called the "zonal mode". There is ample evidence that TAV is remotely influenced by ENSO [*Enfield and Mayer*, 1997], and by the North Atlantic Oscillation (NAO) [*Marshall et al.*, 2001]. However, recent modeling studies have also shown that tropical Atlantic SST can in turn influence the NAO [*Robertson et al.*, 1999], and induce changes in the ITCZ of the eastern tropical Pacific

[*Saravanan and Chang*, 2000]. Thus, further understanding of TAV will benefit not only the development of seasonal-to-interannual climate prediction in the region, but also the understanding of global scale climate variability.

B. Objectives

In the first part of this study we assess the influence of SST on the variability of the SACZ, and its seasonal potential predictability. We approach this problem as a predictability problem of the second kind, that is, SSTs are assumed to be known in advance and the estimation of potential predictability gives an upper limit for seasonal predictability (see Apendix A). We search for spatial structures that are optimally forced by SST anomalies from the global oceans, and study the physical mechanisms involved. To do so we use large ensembles of Atmospheric General Circulation Models (AGCMs) forced with observed SST as boundary condition.

In the second part of this study we study the variability of the gradient mode. Its evolution has been shown to be influenced locally by thermodynamic air-sea feedbacks [*Chang et al.*, 1997], and remotely by ENSO and the NAO. These remote influences act primarily on the northern tropical Atlantic. To date, the possibility of a Southern Hemisphere (SH) influence has not been addressed. Here we try to fill in the gap and explore the role of the SH atmospheric circulation in the evolution of the gradient mode, so that a more comprehensive understanding of the mode's behavior is achieved.

Recently, *Chang et al.* [2003a] coupled an AGCM to a slab ocean to predict tropical Atlantic SSTs. The model showed large skill for SST prediction in the tropical North Atlantic, but low skill in equatorial and cold tongue regions, presumably due to the absence of ocean dynamics. In the third part of the study we investigate

the importance of ocean dynamics in TAV. Here, we will approach the problem as a predictability problem of the first kind, that is, one in which the evolution of the atmosphere and the ocean is calculated at the same time (see Apendix A). A specific issue we want to address is the following: is it possible to correct the slab ocean statistically in such a way that empirically parameterizes the relevant ocean dynamics and improves the seasonal climate prediction of TAV?

CHAPTER II

VARIABILITY OF THE SOUTH ATLANTIC CONVERGENCE ZONE

A. Introduction

The South Atlantic convergence zone (SACZ) is a band of convective activity with high rainfall rates which develops in a region defined roughly by [15°S-40°S, 55°W-20°W] in a northwest-southeast line. It extends from the active convective area in the Amazon to the southeast subtropical and extratropical Atlantic Ocean [*Kodama*, 1992]. The SACZ has its largest manifestation during the summer season (January-February-March, JFM) of the Southern Hemisphere (SH).

Kodama [1992, 1993] suggested that the SACZ as well as other subtropical convergence zones, such as the South Pacific convergence zone (SPCZ), appear when two necessary conditions in the midlatitude circulation are satisfied: 1) subtropical jet flows in the subtropical latitudes (30°S to 35°S), and 2) low-level poleward flows prevail along the western peripheries of the subtropical highs. If these conditions are not satisfied, the convergence zone is weak and low rainfall rates are expected. This is because a poleward flow intensifies moisture convergence, and together with the subtropical jet they lead to favorable conditions for development of frontogenesis and convective instability. These conditions are usually met in the summer season together with the development of a heat low on the continent which increases the poleward flow in the eastern side of the continent, thus increasing moisture availabil-

---

ity.

Figueroa et al. [1995] reported the results of a regional eta-coordinate model simulation of the SACZ. Their results show that diabatic heating over the Amazon and the steep Andean topography are essential ingredients for the formation of the SACZ, while the inclusion of the climatological flow introduces modifications mainly in the location of the convergence zone. *Lenters and Cook* [1995], on the other hand, attribute the formation of the SACZ to the "continentality", i.e., the land-sea contrast in the absence of topography and longitudinal SST variations. Using a simple tropical atmosphere model, *Wang and Li* [1993] studied the formation of the SPCZ and suggested that the SST gradients could originate this convergence zone. In the SACZ case, *Figueroa et al.* [1995] argue that warm SST does not play a very important role in the generation of the SACZ because the warm SST tongue in the South Atlantic does not coincide with the location of the SACZ, but lies to the north of it (Figure 2). However, this does not necessarily exclude the possible influence of SST anomalies on the variability of the SACZ. In fact, the work of *Lenters and Cook* [1995], where the inclusion of non-zonal SST affected both the position and intensity of the SACZ, hinted the potential importance of SST influence.

In an observational and mechanistic study, *Kalnay et al.* [1986] reported the existence of a relationship between the strengthening of the SACZ and a strong eastward-shifted SPCZ in austral summer. They further speculate that this teleconnection would take place through changes in the Walker circulation during warm ENSO years. In a more recent work, *Robertson and Mechoso* [2000] found that the SACZ shows both interannual and interdecadal variability. On interannual time scales, an intensification of the SACZ and associated anomalous descent to the southwest, are accompanied by an upper troposphere cyclonic eddy in the lee side of the Andes. Accompanying these interannual variations are atmospherically forced SST anomalies of

dipole-like structure with a nodal line near 40°S. In their study interannual variability was found to be largely independent of ENSO. On interdecadal time scales, a 15-17 year component was detected, which shows correlation to SST in the subtropical South Atlantic.

The main purpose of this chapter is to examine the forced interannual and decadal variability of the SACZ. We are particularly interested in the forced part of the total variability because it is the only part that may have some predictability by knowing the changes in the boundary conditions beyond the two-week limit of weather prediction imposed by the chaotic nature of the atmosphere. We hypothesize two possible ways that variability of the SACZ may be influenced by SSTs. The first would be a remote influence in which the ENSO related variability in the tropical Pacific modifies the atmospheric circulation in the subtropical Atlantic leading to changes in precipitation. The second way is through the local influence of the Atlantic SST anomalies. A possible mechanism in the latter case, though not fully tested here, is that SST anomalies modify the stability properties of the atmospheric boundary layer producing changes in the convective activity and subsequently in the strength of the SACZ.

The chapter is organized as follows. Section B introduces the model and data sets and describes the methodology used in this work. A comparison between simulated and observational climatologies and variabilities is given in section C. In section D we investigate the preferred modes of variability in the SACZ region and search for forced responses using the signal-to-noise optimization procedure. Section E summarizes our findings and discusses their relationship with previous works. In section F we test the sensitivity of the results on model physics by comparing with the output of another model. The last section presents our conclusions.

B. Data and methodology

1. Data

The data set used here consists of monthly mean fields from 5 runs of the latest version of the Community Climate Model (CCM3) developed at the National Center of Atmospheric Research (NCAR). The model has a spectral truncation T42 in the horizontal direction and 18 vertical levels. A complete description of the model physics can be found in *Kiehl et al.* [1998]. Here we give a short summary of the physical packages that influence most the structure and intensity of precipitation anomaly: convective and land surface schemes. The CCM3 uses the scheme developed by *Zhang and McFarlane* [1995] to account mainly for the effects of deep convection, and the scheme of *Hack* [1994] to deal with shallow and mid-level convection. The Zhang-McFarlane scheme assumes that the effects of convection are to relax the convective available potential energy (CAPE) towards a specified threshold value with a specified time scale. Quasi-equilibrium states develop when large scale processes act to persistently increase local CAPE. The land surface models (LSM) used in CCM3 is the NCAR LSM 1.0, which is a one-dimensional model of energy, momentum, water and CO_2 exchange between atmosphere and land. It accounts for ecological differences among vegetation types, hydraulic and thermal differences among soil types, and allows for multiple surface types including lakes and wetlands within a grid cell *Bonan* [1998].

The 5 runs were forced with identical observed global SST from January 1950 to December 1994, but initialized with slightly different initial conditions in order to represent the internal atmospheric variability which has been shown to be fairly well reproduced by this model [*Saravanan*, 1998]. The imposed SST is that of *Smith et al.* [1996], in which a reconstruction algorithm based on empirical orthogonal functions is used to generate the data set. This set of runs has been referred to as GOGA runs,

e.g., [*Saravanan and Chang*, 2000]. The specification of SST implies that the ocean has infinite heat capacity, and does not allow for any kind of feedback between the ocean and the atmosphere in the model.

Since we are mainly interested in the SACZ variability, the analyses presented below are confined in the domain from 70°W to 20°E in longitude and from 50°S to 20°N in latitude. We analyze the variability only in the austral summer season (JFM), when the SACZ shows its mature development. Therefore, we take seasonal averages of the monthly mean data over these three months, which leaves us with an ensemble of 5 runs, each comprising 45 austral summers with a spatial resolution of roughly 2.8° x 2.8° degrees.

Two key variables are chosen to describe the state of the simulated SACZ: the precipitation field as a measure of atmospheric convective activity, and the divergence of the upper level (200mb) winds as an indication of changes in the upper level circulation of the atmosphere. To compare with observed variability, we use the Xie-Arkin data set for the precipitation [*Xie and Arkin*, 1996], and the NCEP-NCAR (National Center for Environmental Prediction-National Center for Atmospheric Research) Reanalysis data set for the upper level wind flow [*Kalnay et al.*, 1996]. Both fields have been proven useful for characterizing large scale, low-frequency variability of the SACZ, e.g., [*Robertson and Mechoso*, 2000]. Since the observed and simulated data sets cover different time periods, the comparison of observed and modeled climatology and variability was made in the common time periods, i.e. 1979-1994 for precipitation and 1958-1994 for the upper level wind divergence.

2. Methodology

Finding a forced signal, either local or remote, in the subtropical atmosphere is not a trivial task due to the large atmospheric internal variability [*Venzke et al.*, 1999;

Chang et al., 2000]. If we consider the internal variability as "noise", this problem can be overcome by applying a so called signal-to-noise (S/N) optimization procedure to an ensemble of AGCM integrations. Conceptually, this analysis is based on a pre-whitening technique commonly used in signal processing. It is related to the optimal fingerprint algorithm of *Hasselmann* [1979]. We apply this S/N optimization analysis to extract the forced signal in the SACZ variability in much the same way as done in *Venzke et al.* [1999] and *Chang et al.* [2000]. The technique is described in Appendix A and references therein. Here, we will merely touch upon what lies at the heart of the algorithm: the pre-whitening filter.

The pre-whitening filter technique requires the construction of a filter based on the empirical orthogonal functions (EOF) calculated for the "noise" (internal variability only), which can be computed as the combined departures of each ensemble member from the ensemble mean. Results may depend on the number of EOFs, i.e. truncation level, used to construct the filter. Usual values range from 15 [*Venzke et al.*, 1999] to 36 [*Chang et al.*, 2000]. *Chang et al.* [2000] found that individual seasons show some sensitivity to the truncation level. Accordingly, sensitivity tests are needed to obtain robust results. In this study we found that results are stable when truncation level varies between 30 and 60 "noise" EOFs. Therefore, all the filters were constructed using 40 "noise" EOFs and the results shown below were based on this choice of truncation. This truncation level is in agreement with the rule of thumb discussed in *Chang et al.* [2000] in which a minimum number of 5 samples per truncation level is demanded. In section F we use a modified version of this technique in which there is no need to explicitly construct the pre-whitening filter. Results are, nevertheless, independent of way the technique is implemented.

Before applying the S/N optimization algorithm, we performed a conventional EOF analysis on the precipitation and upper level wind divergence fields in order to

find the dominant patterns of circulation in the atmosphere. Since these EOFs contain not only the forced response, but also the internal variability, we expect to find differences in the patterns obtained from different ensemble members. Two limiting cases are of interest: In the case where the forced signal is dominant, conventional EOFs and S/N optimals should be very similar in the sense that both patterns would be attributed to SST forcing, and associated time series should be significantly correlated to SST time evolution. In the case where the internal variability dominates, conventional EOFs should show little connection to sea surface temperature anomaly. In the SACZ region, we expect the latter case to hold, i.e., conventional EOFs and S/N optimals are likely to be different.

In addition to EOF analysis, correlation and regression analyses were also carried out in order to find relationships between SST anomalies and the atmospheric response. A two-sided Student's t-test [*von Storch and Zwiers*, 1999] was used to assess the local statistical significance of the correlations at the 95% significance level under the assumption that summer seasons in different years are independent (no year to year persistence) so that the number of degrees of freedom is equal to the number of data points. Values below the 95% significance level ($r < 0.3$) were considered to be not significantly correlated.

C. Climatology

The climatology and RMS variability of the ensemble mean and of ensemble members are compared against observational counterparts. The RMS of the ensemble members is calculated after concatenating all 5 members to form only one time series. We expect climatologies of ensemble mean and of ensemble members to be almost identical, but the RMS of the ensemble mean to be significantly smaller due to the

reduction of internal variability. If the model was perfect, then reality would be one realization of the ensemble runs. In this case we would expect that the observed data had the same statistics as the ensemble members. Therefore, the RMS deviation of the observations should be compared to the RMS deviation of ensemble members rather than that of the ensemble mean.

Figure 2 shows the climatology and RMS deviation of the precipitation field for the ensemble mean, ensemble members and the Xie-Arkin data. Superimposed is the summertime climatology of the Atlantic SST. It is clear that the CCM3 reproduces the overall pattern of austral summertime precipitation. The SACZ appears as a northwest-southeast band of heavy precipitation extending from the Amazon basin toward off the coast of southern Brazil. The mean axis of maximum precipitation in the SACZ region is shown as a dashed line in Figure 2a. The intensity of the SACZ is somewhat overestimated compared to the observations in much the same way as in the Atlantic ITCZ region (Figures 2a, 2c and 2e). For comparison, in the Pacific sector the ITCZ and SPCZ regions are also somewhat overestimated, while in the monsoon trough the precipitation is not as large as in the observations. Note also that contrary to observations the mean modeled ITCZ axis in the Atlantic sector is located to the south of the Equator. The SACZ variability is indicated by the RMS deviation maps, which shows interannual variability of comparable magnitude as the seasonal means. As expected, although the patterns of RMS deviation look similar in all three cases, the RMS of ensemble members is in a closer agreement in magnitude with observations than that of the ensemble mean. A comparison between the RMS variability of the ensemble mean and ensemble members indicates a significant reduction of the RMS variability over South America for the ensemble mean, whereas the reduction over the ocean is much smaller. This suggests that the precipitation variability over the land is largely dominated by the internal variability of the atmosphere and land-atmosphere

interactions. Over the ocean the precipitation variability is more influenced by the surface boundary conditions, i.e. SST.

To quantify this assertion we calculate the percentage of precipitation variability due to internal dynamics as given by the difference between the variability of ensemble members and that of the ensemble mean over the variability of ensemble members. The result indicates that over land approximately 65% of the total precipitation variance may be attributed to internal variability. Over the tropical Atlantic Ocean, in the ITCZ region, internal variability accounts only for 20% of precipitation variance, while in the subtropical regions of the Atlantic it accounts for 50% of total variance. In the SACZ region indicated by the rectangular box in Figure 2, the mean explained precipitation variance by internal variability is 59%. Of particular interest is a relatively small area of the precipitation anomaly associated with the SACZ over the South Atlantic Ocean, where the internal variability explains only about 30% of total variance. The analysis presented below suggests that a significant portion of this precipitation anomaly can be explained as a forced response to South Atlantic SSTs. The potential predictability of precipitation in the SACZ region will be further examined in section F.

Figure 3 shows the climatologies and RMS variability of the 200 mb wind divergence in JFM season. The axis of mean maximum divergence in the SACZ region is shown as a dashed line in Figure 3a. Here we contrast the CCM3 results with the divergence calculated from the NCEP-NCAR Reanalysis data set. It is evident that the overall structures of the two climatologies bear certain resemblance. However, the SACZ in the CCM3 is more sharply defined and more closely connected to the convective activities over the Amazon basin and the ITCZ region than that in the NCEP-NCAR Reanalysis. The SACZ in the NCEP-NCAR Reanalysis has a particularly weak structure over the ocean (Figures 3a, 3c and 3e). This is in contrast to

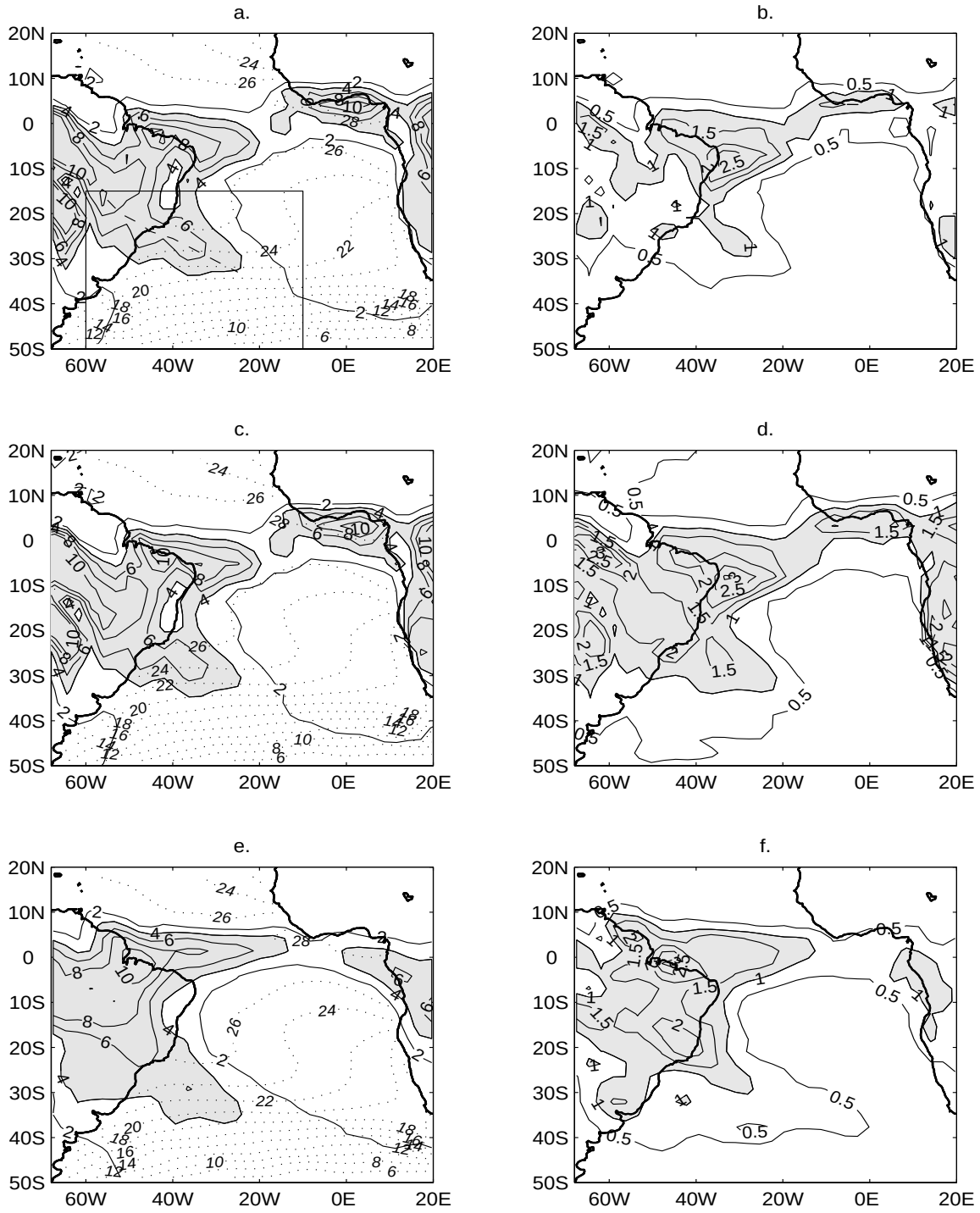

Fig. 2. JFM precipitation climatology and RMS variability for ensemble mean (a,b), ensemble member (c,d) and Xie-Arkin data (e,f). Contours are in mm day^{-1}. Superposed is the SST climatology in JFM (dotted lines). The box marks the SACZ region and the dashed line marks the mean precipitation axis of SACZ.

the ITCZ where the NCEP-NCAR climatology shows a stronger structure than the CCM3. In terms of RMS variability, the SACZ structure is not as well defined as in the precipitation field, although a clear signal can still be identified in all three cases. Again, we find that the RMS variability of the ensemble members bears closer resemblance in both spatial structure and magnitude to that of the NCEP-NCAR Reanalysis. Comparing Figures 3b, 3d and 3f, it is seen that the RMS variability of the ensemble mean is significantly weaker than that of the ensemble members and of the NCEP-NCAR Reanalysis throughout the tropical Atlantic sector, suggesting that much of variability of the upper atmosphere is governed by the internal atmospheric variability.

In summary, we can conclude that the CCM3 reproduces reasonable well the climatology and RMS variability of the precipitation and 200mb wind divergence over the tropical and subtropical South Atlantic. It has been shown by many investigators, e.g., [*Hess et al.*, 1993], that different convective parameterizations may lead to different results in precipitation variability. Therefore, although the CCM3 appears to reproduce the major features of the SACZ fairly realistically, results may be, however, model dependent. An intercomparison study with other models and with higher resolution is desirable in order to assure that results presented below are not resolution or model dependent. Section F presents an intercomparison study of the CCM3 with version 1.0 of the AGCM developed at the NASA Seasonal-to-Interannual Prediction Project (NSIPP-1 model).

D. Identification of forced responses

In this section we further analyze the precipitation and divergence fields using a number of statistical techniques to search for forced patterns of variability in the

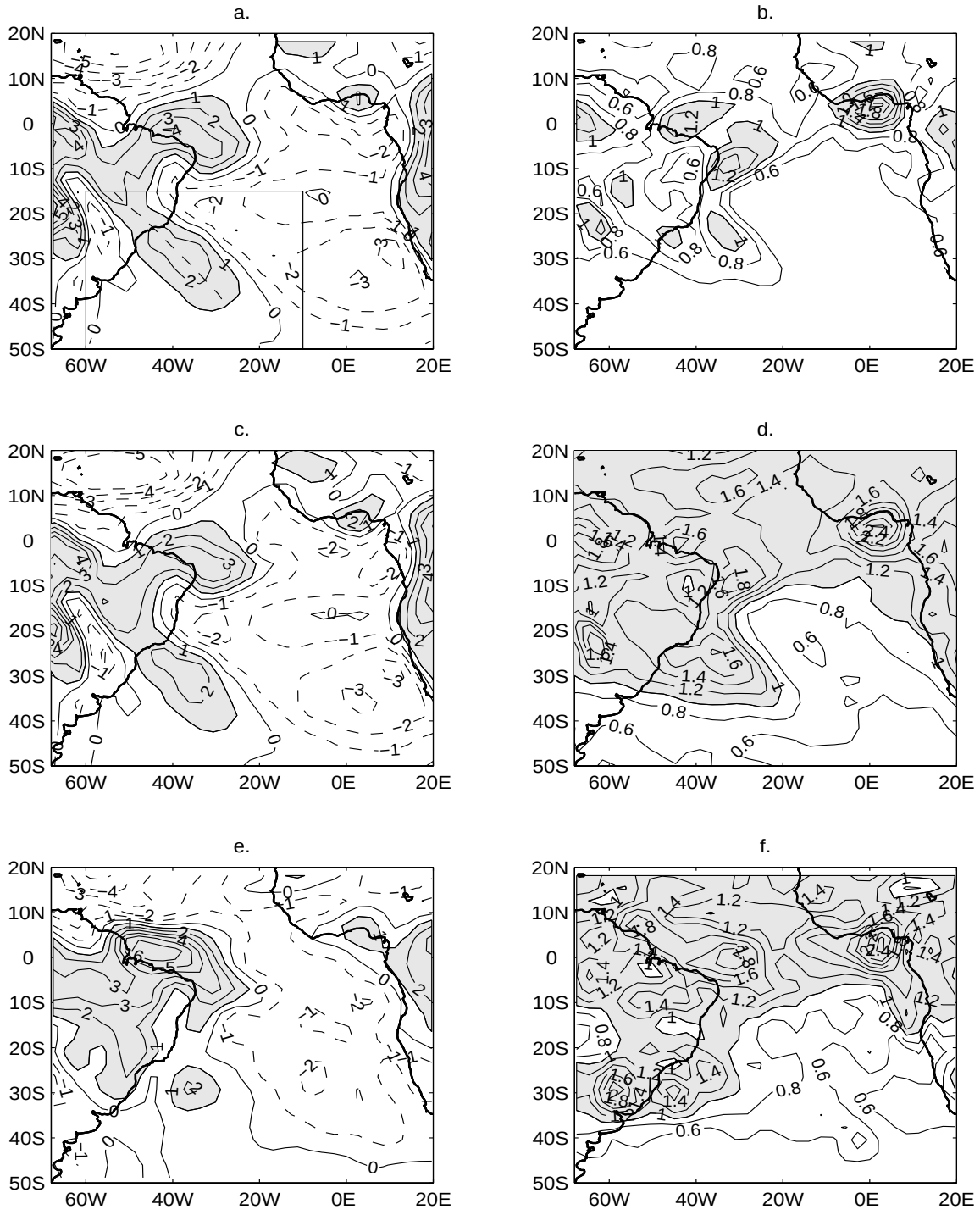

Fig. 3. JFM 200mb wind divergence climatology and RMS variability for period 1958-1994 for CCM3 ensemble mean (a,b), CCM3 ensemble member (c,d) and NCEP-NCAR Reanalysis data set (e,f). In (a) dashed line marks the mean axis of maximum divergence in the SACZ region. Contour interval is 10^{-6} s^{-1}.

subtropical atmosphere. First, we applied conventional EOF and regression analyses to the simulations and compare the results with the corresponding observations. Then we employ the signal-to-noise optimization analysis to identify the forced response of the atmosphere to SST anomalies. All the analyses were performed in the SACZ region defined as the region between 60°W and 10°W in longitude and between 50°S and 15°S in latitude (the box indicated in Figure 2a). This choice of the analysis domain is made to isolate the variability of the SACZ from other stronger features of the climate system, such as the ITCZ.

Three indices were constructed to represent the possible SST forcing from the tropical Pacific and Atlantic onto the atmosphere. The influence of ENSO is represented by the Niño3 index defined as the average of SST anomalies over 150°W to 90°W and 5°S to 5°N in JFM. To characterize the South Atlantic SST forcing, we used the principal components (PCs) of the two leading EOF modes of the SST during austral summer, shown in Figure 4. The two leading EOFs account for 37% and 23% of the total variance, respectively. The first EOF shows a dipole-like pattern of SST anomalies, whereas the second shows a monopole centered at (25°W,30°S). We use AT1 and AT2 to denote the PCs associated with the first two leading SST EOFs. Figures 4c and 4d show AT1 and AT2 (solid lines) along with Niño3 index (dotted line) time series. The three time series show little correlation among each other. It is important to note that AT1 exhibits interannual time scales before mid-1970s and decadal time scales after that, while AT2 is mostly dominated by interannual variability superimposed on a linear trend. The first SST EOF (Figure 4a) resembles the second annual EOF of the South Atlantic SST obtained by *Venegas et al.* [1997].

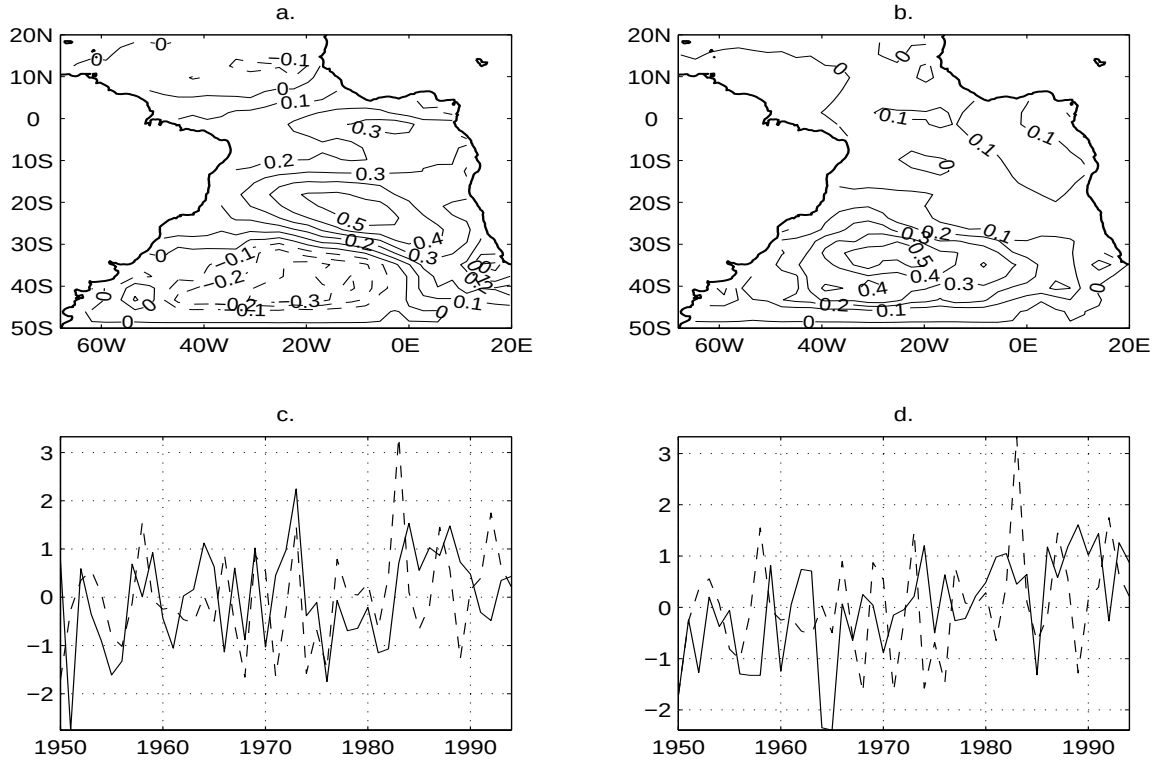

Fig. 4. The leading EOFs of South Atlantic SST variability. (a) and (b) show the spatial patterns of the first and second EOF respectively in units of °C. (c) and (d) show the associated normalized principal components (PCs) of first and second EOFs (AT1 and AT2, solid lines), and the Niño3 index (dotted line).

1. Precipitation variability

EOFs were calculated using the covariance matrix of concatenated ensemble member anomalies. Figures 5a,b show the first and second leading EOFs of the precipitation field, which explain 23% and 18% of total variance respectively. These EOFs are statistically distinct according to the rule of thumb given by *North et al.* [1982]. The first EOF consists in a northeastward-southwestward shift of the continental part of the SACZ from its climatological position (characterized by its mean axis shown as a dashed line in Figure 5a), while the oceanic part tends to strengthen/weaken. The second EOF shows the opposite behavior, i.e., a strengthening of the SACZ over land and a shift over the ocean. The fact that the SACZ does not vary as an integrated structure suggests that the processes governing the variability of the oceanic and continental parts of the SACZ may be different. Figures 2b and 2d hint that the origin of this difference may be in the role of local SST forcing onto the atmosphere. The signal-to-noise optimization analysis discussed below will confirm this finding. However, we caution that this result may depend on the sensitivity of land-atmosphere feedbacks in the model to changes in the hydrological cycle. In the CCM3, this sensitivity appears to be rather weak so that changes in SST-forced precipitation does not seem to trigger a strong feedback between the atmosphere and land, and thus the convective activities over the land region of the SACZ are largely independent of changes in SSTs. Other models may, in principle, behave differently. We will see, however, that the NSIPP-1 model, that has different physical parameterizations, shows a very similar response to SST forcing as that of the CCM3 (see section F).

Figures 5c and 5d show the principal components of leading EOFs associated with each ensemble member. Clearly, there is a large within-ensemble variability, which

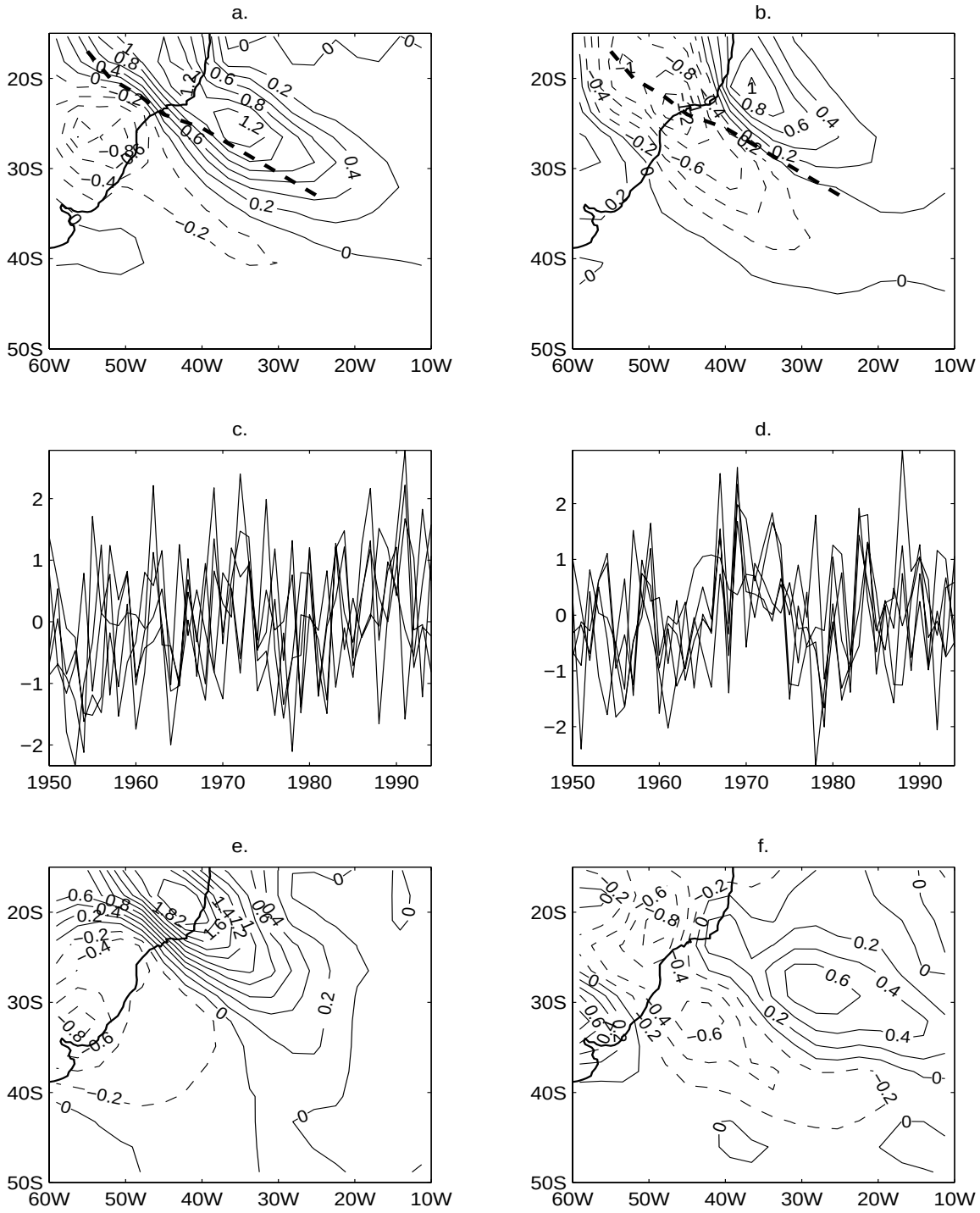

Fig. 5. Leading EOFs of precipitation for CCM3: (a) first EOF, and (b) second EOF. Principal component of each ensemble member associated to first EOF (c), and second EOF (d). Leading EOFs of Xie-Arkin data: (e) first EOF, and (f) second EOF. Units are mm day^{-1}.

Table I. Correlation between the PC time series of the first EOF of precipitation anomalies of each ensemble member and the South Atlantic indices (AT1 and AT2) and Niño3 index. PC-i denotes principal component time series associated to i-th ensemble member. '*' denotes values that are not significant at 95% level.

	PC-0	PC-1	PC-2	PC-3	PC-4
Niño3	*	*	*	*	*
AT1	0.32	*	0.41	*	*
AT2	-0.34	-0.32	*	*	*

results from a large internal variability. Tables I and II summarize the correlations between the PCs of each ensemble member and the three indices, i.e., Niño3 index, AT1 (first Atlantic SST mode) and AT2 (second Atlantic SST mode). Only those correlations that are above the 95% significance level according to a Student t-test are shown; values that are below the 95% significance level are indicated by '*'. As expected from the large within-ensemble variability, correlations with the indices vary from one ensemble to another. Interestingly, no PCs of either the first or second EOFs of ensemble members show significant correlation with ENSO. However, some of the PCs do display significant correlation with Atlantic SST anomalies. Since each ensemble member represents a particular realization of the system, there is no "a priori" reason to judge which ensemble member is more realistic. Therefore, the significant correlation shown by some PCs of ensemble members may occur by chance and does not necessarily mean that there is a real relationship between SACZ precipitation anomalies and the Atlantic SST anomalies.

Next we compare the EOF analysis of the CCM3 ensemble mean with those of

Table II. The same as Table 1, except for the second EOF of precipitation anomalies.

	PC-0	PC-1	PC-2	PC-3	PC-4
Niño3	*	*	*	*	*
AT1	0.37	*	0.34	0.44	0.47
AT2	*	*	*	*	0.33

individual ensemble members. The first EOF of the ensemble mean is almost identical to Figure 5a (not shown) and explains 28% of the total variance. The second EOF accounts for 20% of the total variance and is very similar to Figure 5b (not shown). Table III shows the correlation between the ensemble mean PCs and the three indices characterizing ENSO and South Atlantic SST variability. The two leading modes of ensemble mean again show no correlation to ENSO SST anomalies. The first EOF of the ensemble mean, on the other hand, shows a high correlation (0.64) with the first Atlantic SST mode, while the second EOF shows a correlation of (-0.52) with the second mode of Atlantic SST variability. Thus, the two leading modes of precipitation in the SACZ region seem to be related to the first two modes of variability of SST in the South Atlantic Ocean, although there are also contributions of the second South Atlantic SST mode to the first precipitation EOF and of the first South Atlantic SST mode to the second precipitation EOF (Table III).

A similar EOF analysis of the observed precipitation from the Xie-Arkin data set results in two EOFs shown in Figures 5e and 5f, each of which explains 38% and 12% of the total variance, respectively. Both EOFs exhibit similarity to the corresponding patterns of the CCM3 ensemble members or ensemble mean, particularly for the first EOF (Figures 5a and 5e). However, the observed EOFs are not significantly

Table III. Correlation between the PC time series of first two leading EOFs of ensemble mean precipitation (first two columns) and of Xie-Arkin data set (last two columns) and the South Atlantic indices (AT1 and AT2) and Niño3 index. '*' denotes values that are not significant at 95% level.

	PC1em	PC2em	PC1xa	PC2xa
Niño3	*	*	*	*
AT1	0.64	0.34	*	*
AT2	0.35	-0.52	*	*

correlated with ENSO or with South Atlantic SST modes (Table III).

The above EOF analysis reveals a considerable variability in the temporal behavior of the dominant modes among the ensemble members and ensemble mean. These differences arise because the EOFs are constructed in such a way that they simply maximize the variance explained in a given data set. Since the total variability consists of both forced and internal variability, the variance explained by these EOFs contains a large fraction of internal variability which varies significantly from one ensemble to another. The EOFs of the ensemble mean give better estimates of forced patterns because the process of averaging filters out some portion of the internal variability. The projections of the individual ensemble members onto the EOFs of the ensemble mean are spread around the time series of the ensemble mean (not shown). This indicates that even the EOFs of the ensemble mean are not common structures to all ensemble members and thus do not represent the true forced responses of the atmosphere to SST forcing.

In order to separate the forced response of the precipitation field from its internal variability, we performed the signal-to-noise optimization analysis as discussed in

section B.2. Results are displayed in Figure 6. The leading S/N-optimal shows a dipole pattern over the South Atlantic Ocean off the coast of South America with almost no loading over land (Figure 6a).

The associated principal component (PR1) shows no significant correlation to ENSO, but is highly correlated with the first Atlantic SST mode with a correlation of 0.7 which is significant at the 99% level (Figure 6c). The correlation increases to 0.77 when a Parzen filter window of 5 years is applied. This result lends support to the hypothesis that local SSTs provide a forcing onto the atmosphere. Note that the pattern is similar to the oceanic part of the second regular EOF of precipitation, i.e., positive anomalies to the north of the mean SACZ axis and negative anomalies to the south. The fact that there is almost no signal over land is in agreement with the idea that local SST forcing is an important contributor to the variability of precipitation in the oceanic part of the SACZ, but not in the continental part, i.e. it is a very localized process. This also implies that precipitation variability is mainly influenced by atmospheric internal variability and that the forced signal is hidden within the total response.

The large-scale circulation structure associated with the dominant forced mode is constructed by regressing SST, surface pressure, surface winds, precipitation and surface fluxes onto PR1. Regressions are done over the domain from 70°W to 20°E in longitude and from 50°S to 20°N in latitude to better reveal the circulation structure. Figure 7a shows the regression of surface winds and SST onto PR1. The structure of the SST anomalies shows a similar dipole structure as the first South Atlantic SST mode in Figure 4a with maximum amplitude of 0.4°C at 20°S. The maximum explained local variance by this mode is about 70% of the total variance near the maximum SST anomaly. Surface wind vectors show anomalous circulation with a maximum wind speed of 1.0 ms^{-1} flowing southward in the ITCZ region and north-

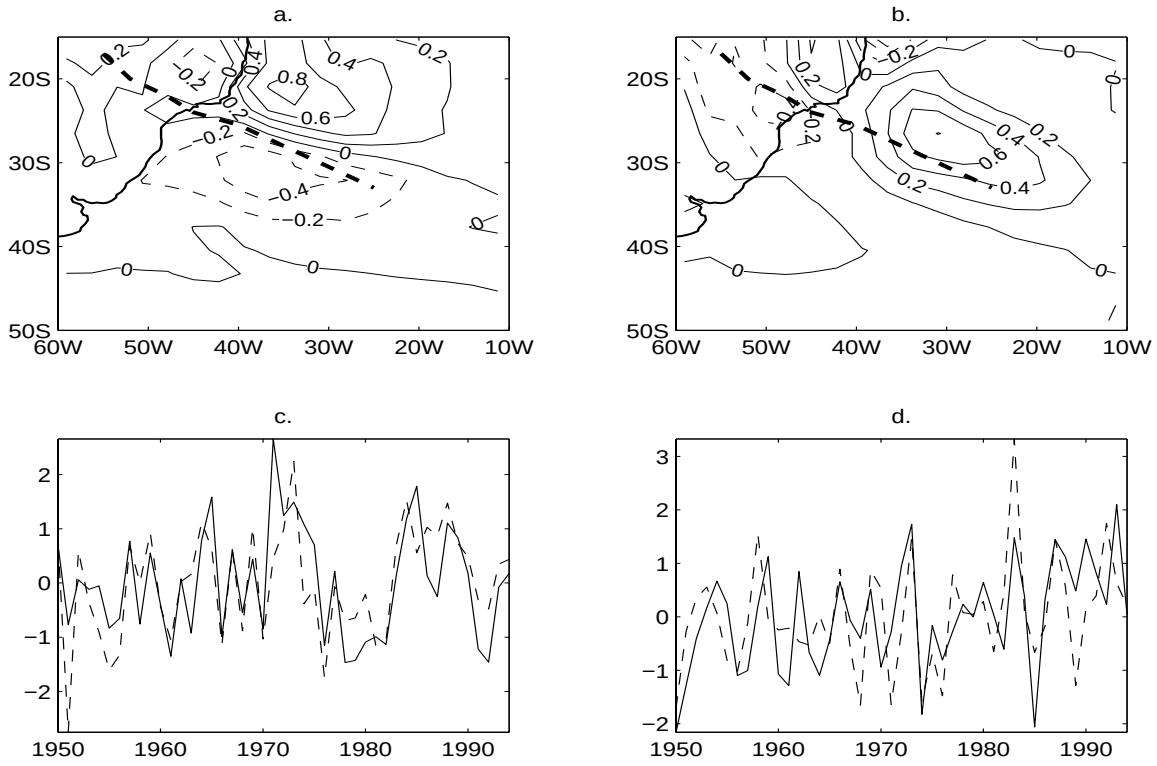

Fig. 6. Signal-to-noise optimal patterns for precipitation in mm day^{-1}: (a) the first dominant forced response, and (b) second dominant forced response. (c) PC time series of the first S/N-optimal (PR1, solid line) and of the leading South Atlantic mode of SST variability (AT1, dotted line). (d) PC time series of the second S/N-optimal (PR2, solid line) and Niño3 index (dotted line). In (a) and (b) the dashed lines marks the mean precipitation axis in the SACZ region.

westward to the south of the SACZ region. Thus, anomalous winds enhance moisture advection to the northern part of the SACZ and bring drier air to the southeastern part. The anomalous flow converges at (20°S, 30°W) and forms a cyclonic circulation largely in geostrophic balance with the surface pressure anomaly shown in Figure 7b. At upper levels the circulation anomaly consists of an anticyclonic eddy at the same location (not shown), which is consistent with a Gill-type baroclinic response to a local warm SST anomaly.

The regression of the precipitation is shown in Figure 7c. It indicates a positive correlation between precipitation and SST anomalies consistent with previous results. This mode accounts for a large portion of the total precipitation variance near the center of maximum precipitation. The location of the maximum precipitation anomaly (0.8 mmday^{-1}) also coincides with the center of convergence and of largest negative anomaly in surface pressure. Note that the center of maximum precipitation is displaced from the center of maximum SST anomalies towards the land. Figure 7d shows the regression of the net downward surface heat flux onto PR1. As can be seen, in the subtropics the heat flux anomalies have opposite signs to the SST anomalies, indicating a negative feedback in which the atmosphere damps the SST anomalies. On the contrary, in the deep tropics the SST and heat flux anomalies have the same sign, suggesting the existence of a positive feedback [*Chang et al.*, 2000]. These results support the hypothesis of local SST forcing the atmosphere through modifications of the boundary layer stability properties by enhanced atmospheric surface heat fluxes.

Heat flux anomalies in the deep tropics resemble the pattern associated to the Atlantic gradient mode [*Chang et al.*, 2000]. Also, Figures 7a and 7c suggest that when the SACZ moves northward, the ITCZ moves southward as the warm anomaly of the cross-equatorial gradient develops in the tropical South Atlantic. Therefore, the first EOF of SST anomalies in the South Atlantic Ocean seems to be related to the

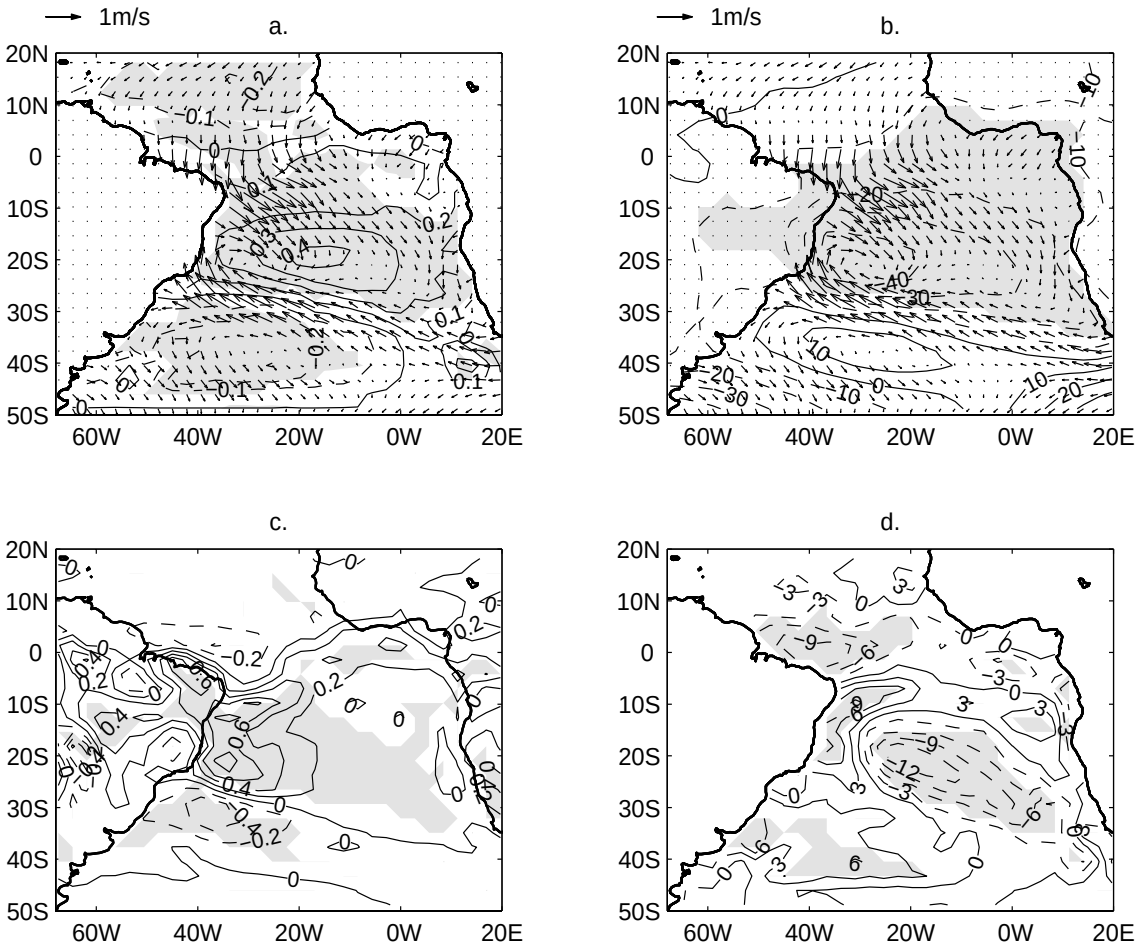

Fig. 7. Three dimensional structure of the leading S/N-optimal construc- ted by regressing (a) SST (°C) and surface winds anomalies (m s^{-1}), (b) pressure (Pa) and surface wind anomalies, (c) precipitation (mm day^{-1}) and (d) downward surface heat fluxes (W m^{-2}), onto PR1. Arrow indicates wind anomalies of 1 m s^{-1}. Shaded areas are significant at the 95% level. In (a) shaded areas indicate *SST* anomalies significant to 95% level, in (b) shaded areas indicate *pressure* anomalies significant to 95% level.

tropical Atlantic gradient mode. A further exploration of the relationship between the ITCZ and the SH atmospheric circulation and SST anomaly is done in Chapter III.

The second S/N-optimal of precipitation shows mainly a strengthening (weakening) of the northern oceanic portion of the SACZ and a shift over the land (Figure 6b), capturing some features of the first regular EOF. The associated PC (PR2) is correlated to ENSO ($r = 0.56$) (Figure 6d), and also to both the first and second Atlantic SST modes of variability with $r = 0.36$ and $r = 0.53$, respectively. Therefore, this precipitation pattern seems to result from both local and remote SST forcing. The structure of this mode is shown in Figure 8. Regressing South Atlantic SST onto PR2 gives rise to a pattern which shows two local maximums at (10°W, 25°S) and at (35°W, 25°S). Figure 8b shows that the anomalous circulation is mostly in geostrophic balance with the pressure anomaly. The regression of precipitation (Figure 8c) shows that the maximum explained variance is over the ocean. Significant precipitation anomalies also exist over the land, suggesting a northward shift of the SACZ. It is interesting to note that the anomalies in the SACZ and ITCZ regions have opposite signs. Finally, the flux anomalies appear as a dipole at both sides of the SACZ main position (Figure 8d). The northern component has the same sign as the SST, suggesting a positive feedback, whereas the southern component has the opposite sign as the SST, suggesting a negative feedback.

In order to see if the precipitation patterns found by the signal-to-noise optimization procedure are common to all the ensemble members we project each ensemble member onto the filter patterns associated with the S/N-optimals (dotted lines in Figure 9). The spread of individual members around the ensemble mean is much reduced compared to the case of conventional EOF analysis, indicating that the patterns found are common to all ensemble members. This shows that the algorithm has

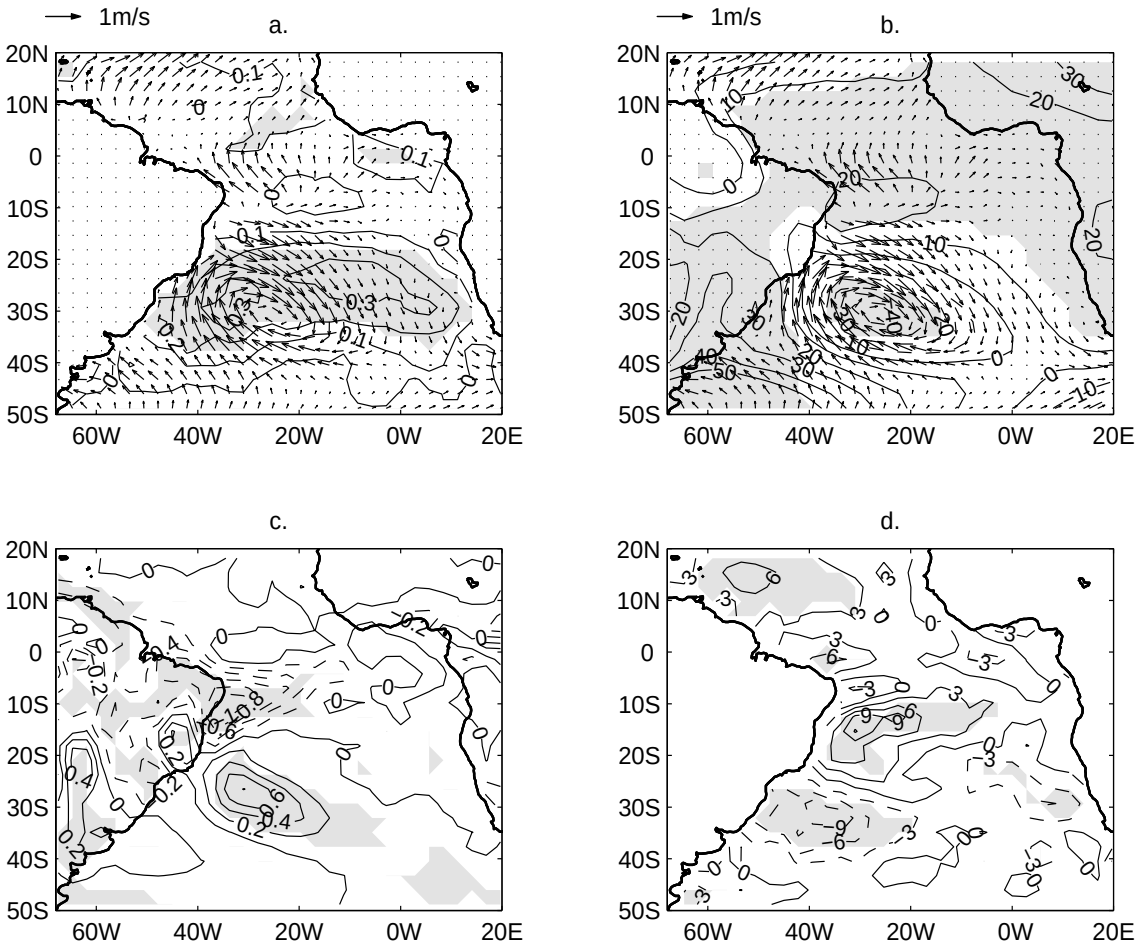

Fig. 8. Same as Figure 7 except for the second S/N-optimal of rainfall.

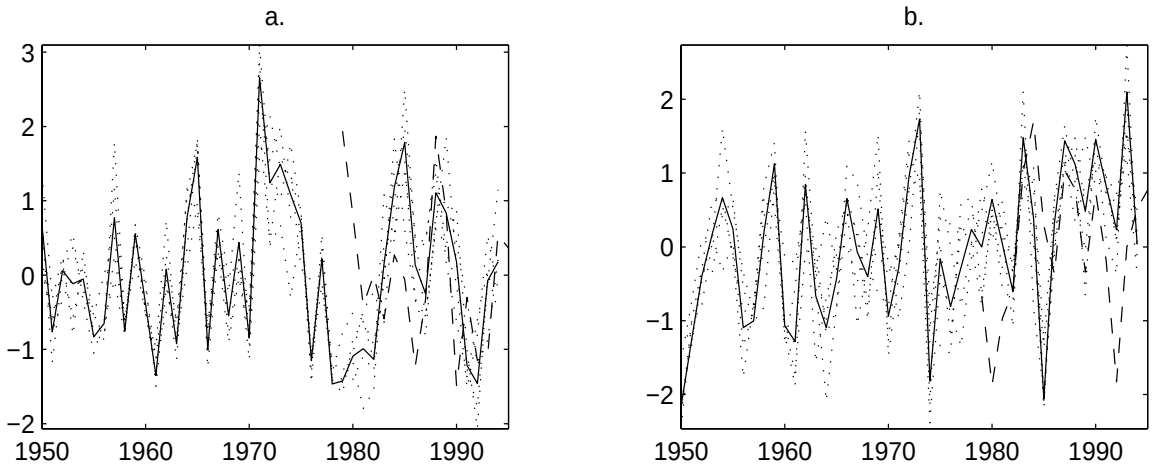

Fig. 9. Principal component time series of the forced precipitation responses (solid lines) superimposed on the projections of CCM3 ensemble members (dotted lines) and of Xie-Arkin data set (dashed line) onto the optimal filter patterns: (a) first S/N-optimal, and (b) second S/N-optimal.

been successful in extracting the true forced response and filtering out the internal variability. Projections of the Xie-Arkin data set onto the filter patterns show time series that appear to follow nicely the variations of model forced responses, especially after 1982. This implies that the model captures an atmospheric response to SST forcing that seems to exist not only in the ensemble simulations but also in the real atmosphere, although certain caution must be taken in interpreting the observations because of the shortness of record length.

2. Variability of upper levels wind divergence

Precipitation variability results from changing conditions over the whole depth of the atmosphere, i.e. it depends on lower and upper level conditions and consequently reflects an integrated effect. In this section we use the upper level wind divergence mostly as a measure of upper level variability. Precipitation and upper level divergence are not always correlated because while strong precipitation is often associated

with upper level divergence, the converse is not always true. As we will find below local responses are seen mainly in lower level fields, while remote influences are felt in upper levels. Thus, the use of upper level wind divergence, which has been often used as a proxy for the location and intensity of the SACZ [*Kodama*, 1992, 1993], is adequate to study remotely-forced perturbations in the SACZ.

Similar analyses to the precipitation were performed to the wind divergence. Figures 10a and 10b show the patterns of the leading EOFs calculated using the covariance matrix constructed after concatenating the ensemble members. The first EOF explains 29% of total variance and the second EOF explains 18% of total variance. Again, the temporal behavior of the patterns differs considerably among ensemble members, indicative of a large atmospheric internal variability (Figures 10c and 10d). In contrast with the precipitation case, the divergence EOF patterns show a consistent behavior over the whole SACZ region. The first EOF presents a northeastward-southwestward displacement of the whole SACZ from its climatological position (marked as dashed line in Figure 10a). Unlike precipitation, however, only two of these leading PCs show significant correlation to the Atlantic SST anomalies, and two of them show significant correlations to ENSO (Table IV).

The second EOF is statistically different from the first and third EOFs according to the North et al's rule. It shows a strengthening (weakening) of the whole SACZ, and the PCs do not show significant correlation with any SST index.

The first two leading modes of the CCM3 ensemble mean are similar to the first and second EOF modes shown in Figures 10a and 10b (not shown) and explain 37% and 17% of total variance respectively. The first EOF is well correlated to ENSO, but only weakly correlated to the South Atlantic SST modes (Table V). Therefore, this mode of variability seems to be mostly remotely forced and only weakly influenced by local SST. The second EOF of ensemble mean does not show significant correlation

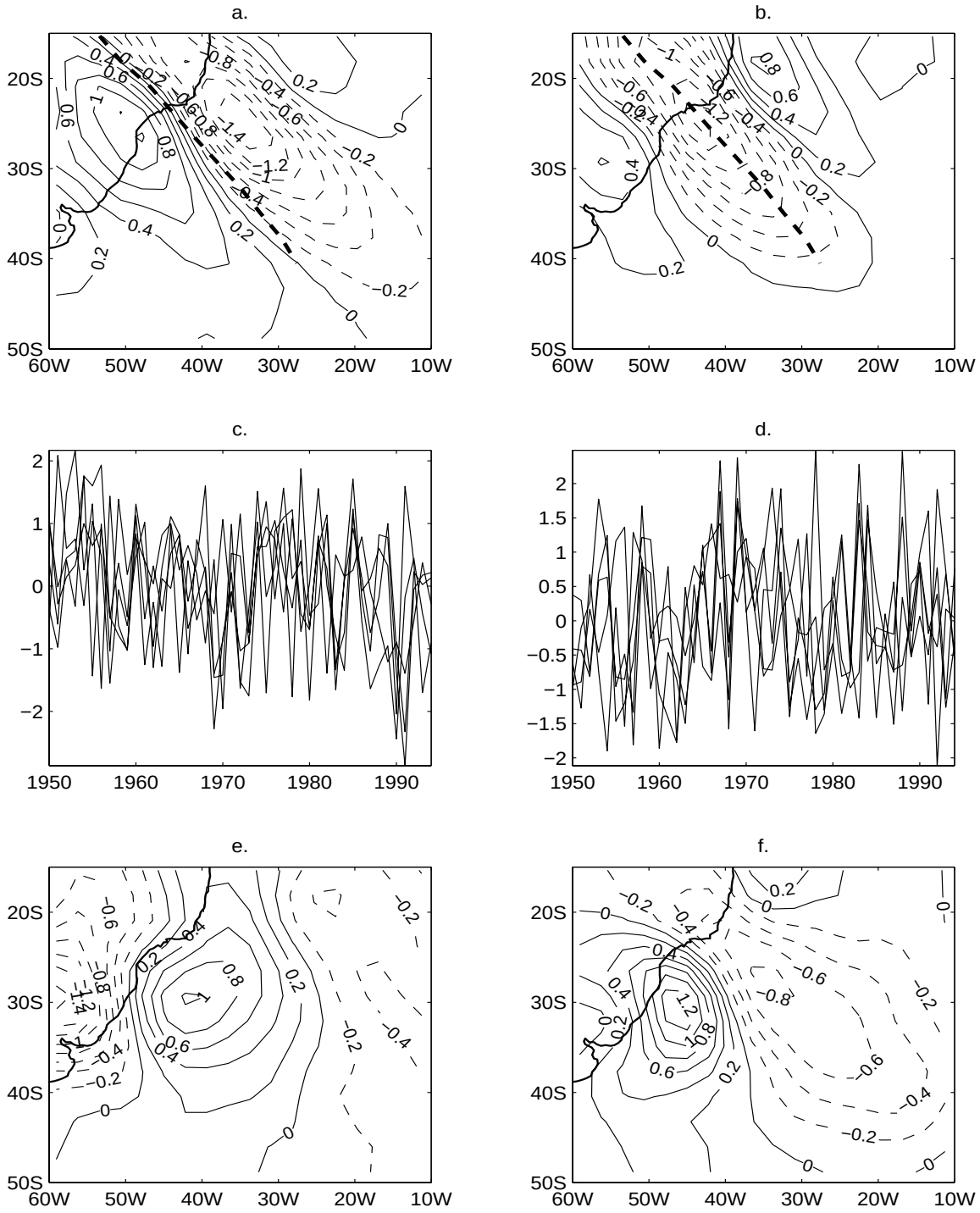

Fig. 10. Leading EOFs of 200mb wind divergence for CCM3: (a) first EOF, and (b) second EOF. Time series of each ensemble member associated with first EOF (c), and second EOF (d). Leading EOFs of NCEP-NCAR data set: (e) first EOF, and (f) second EOF. Units are 10^{-6} s^{-1}.

Table IV. Correlation between the first EOF of 200mb wind divergence anomalies of each ensemble member and the South Atlantic indices (AT1 and AT2) and Niño3 index. PC-i denotes principal component time series associated with the i-th ensemble member. '*' denotes values that are not significant at 95% level.

	PC-0	PC-1	PC-2	PC-3	PC-4
Niño3	0.42	*	0.38	*	*
AT1	*	*	*	-0.34	*
AT2	*	*	*	*	-0.35

with any SST indices according to Table V.

The two leading EOFs calculated for the NCEP-NCAR Reanalysis data set explain 25% and 20% of total variance and are shown in Figures 10e and 10f. The structure of the second NCEP-NCAR EOF shows some similarities to the first ensemble members EOFs. However, the NCEP-NCAR EOFs show no correlation to ENSO and no significant correlation to Atlantic SST modes of variability (Table V).

Projections of individual ensemble members onto the ensemble mean EOFs show large spreading around the ensemble mean (not shown), suggesting that the upper level response contains substantial internal variability. This implies that the first ensemble mean EOF does not reflect the true forced signal, despite its significant correlation to the SST indices shown in Table V.

The leading S/N-optimal shows a forced response in the form of a northeast-southwest shift of the SACZ from its climatological position (Figure 11a). The signal is particularly clear for the region of the SACZ over land. Over the ocean the pattern represents more a strengthening (weakening) of the northern part of the SACZ than a shift from its mean position. The correlation between the associated PC (DI1)

Table V. Correlation of first two leading EOFs of ensemble mean 200mb wind divergence (first two columns) and of NCEP-NCAR data set (third and fourth columns) and the South Atlantic indices (AT1 and AT2) and Niño3 index. '*' denotes values that are not significant at 95% level.

	PC1em	PC2em	PC1ncep	PC2ncep
Niño3	0.52	*	*	*
AT1	0.37	*	*	*
AT2	0.36	*	*	*

and Niño3 index is 0.70 (Figure 11c), implying that during warm ENSO events the upper part of the SACZ tends to displace northeastward over the land and strengthen over the ocean. The associated sea level pressure anomaly (Figure 11b) indicates a northward shift of the South Atlantic subtropical high from its climatological position in agreement with early studies of ENSO influence in this region, e.g., [*Peixoto and Oort*, 1992]. The anomalous surface winds show convergence to the north of the SACZ mean position which is consistent with the northeastward shift of the South Atlantic subtropical high. The regression map of precipitation onto DI1 (Figure 11d) indicates a weakening of the ITCZ, accompanied by the change of precipitation in the SACZ region. The negative rainfall anomaly in tropical regions indicates a weakening and possible northward shift of the ITCZ during warm ENSO events. The southeasterly wind anomaly in the western equatorial Atlantic supports this notion. No significant correlation between DI1 and the Atlantic SST modes of variability is found. However, DI1 shows a correlation of 0.61 with the second S/N-optimal of precipitation (PR2) suggesting that the second dominant pattern of precipitation is linked to the variability in the upper atmosphere. The similarity between the

anomalous rainfall and surface circulation fields in Figures 8b and 8c with 11b and 11d strengthens this finding. We will show below that the close relationship between the two modes can be attributed to the fact that both these modes are induced by remote ENSO influence.

The reduced spread of the projections of ensemble members onto the optimal filter associated to the leading S/N-optimal pattern of divergence confirms that the leading forced mode is in fact a structure common to all ensemble members. The projection of the NCEP-NCAR Reanalysis data set follows very closely the ensemble mean projection, implying that the forced CCM3 response of the upper level wind divergence seems to be also present in the real atmosphere (Figure 11c). The fact that the leading S/N-optimal is more significantly correlated to ENSO than to the South Atlantic SSTs suggests that the upper level divergence is primarily forced by the SST anomalies in the tropical Pacific Ocean, but is not influenced so much by the local Atlantic SST anomalies. This result contrasts sharply with the finding of the precipitation field analysis, which shows a dominant response to local Atlantic SST anomalies. Because of the strong local SST influence on the oceanic part of the SACZ, the variability of the precipitation over the ocean appears to be disconnected from its continental part. On the other hand, the upper level winds are not affected by the local SST and therefore the divergence in the SACZ region varies as one structure (Figures 5a and 5b, and 10a and 10b).

In addition to the above analyses, we have also constructed composite maps associated with the warm ENSO events by averaging all the anomalies where positive values of DI1 exceed one standard deviation. These maps reveal similar spatial patterns as shown in Figures 11b and 11d. However, the composite anomalies are stronger and more sharply defined than those in the regression analyses. In contrast, the composite anomalies of cold ENSO events are generally weaker than the regressed

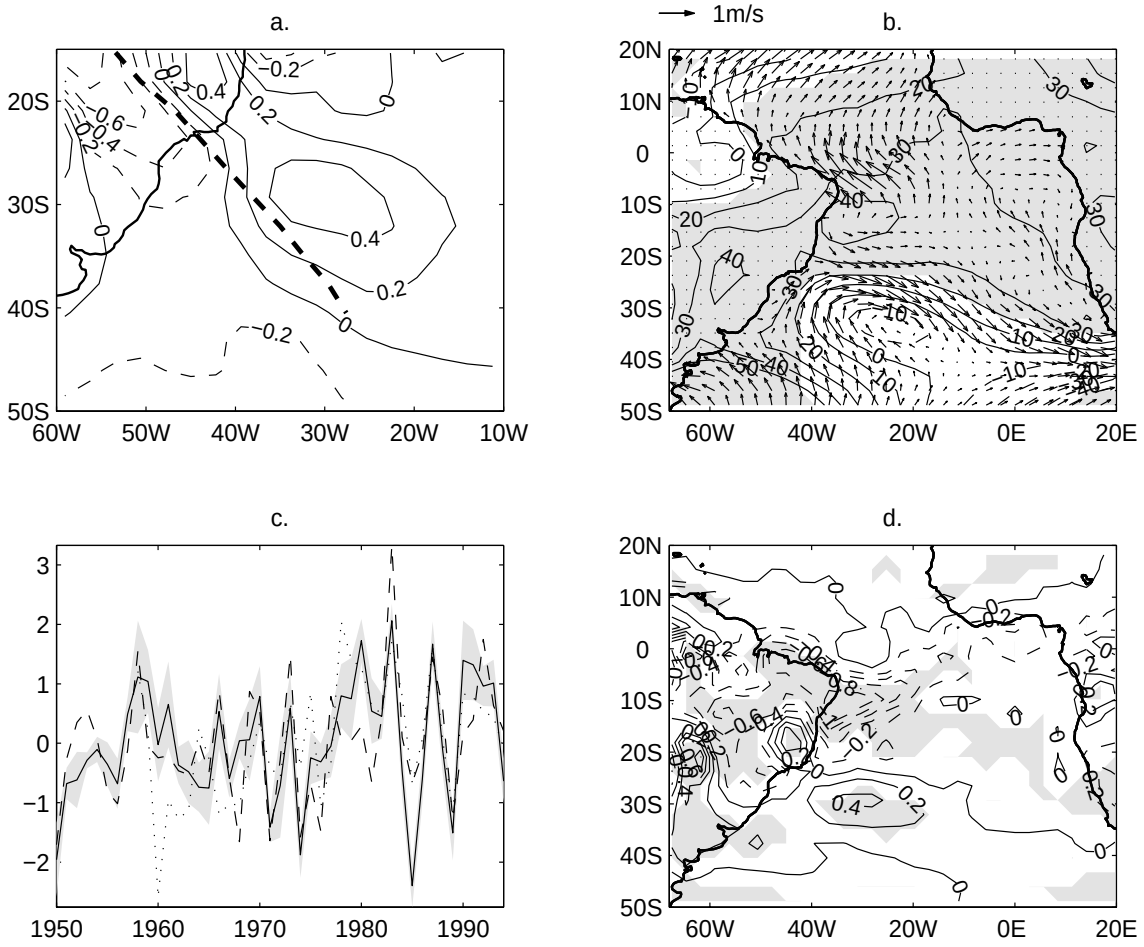

Fig. 11. (a) Leading signal-to-noise optimal pattern of 200mb wind divergence. The dashed line marks the mean axis of maximum divergence in the SACZ region. (b) The associated surface winds and surface pressure anomalies (contour interval is 20hPa). (c) The associated time series (DI1, solid line) and Niño3 index (dashed line). Superimposed is the projection of NCEP-NCAR Reanalysis data set onto the optimal filter pattern (dotted line). Shading shows standard deviation of projections of ensemble members onto optimal filter pattern about DI1. (d) The associated rainfall anomalies, and shade indicates areas significant to 95% level. Arrow indicates wind anomalies of 1 m s^{-1}, and shaded areas are *pressure* anomalies significant to 95% level.

anomalies, particularly over the oceanic portion of the SACZ (not shown). This may imply a nonlinear nature of the SACZ response to ENSO influence. Further studies are needed to understand the difference between SACZ responses to warm and cold ENSO events.

To get a global view on how ENSO forcing propagates into the Atlantic, Figure 12 shows the regression of upper level wind anomalies onto DI1 in the whole tropical-subtropical band. It clearly shows the observed anticyclone straddling the Equator forced by convective anomalies associated to warm ENSO events. The figure also reveals a propagating wave pattern emanating from the tropical Pacific. This supports the notion that a remote influence from the tropical Pacific Ocean occurs in the form of a wavetrain [*Hoskins and Karoly*, 1981]. Associated with this pattern is also a strengthening/weakening of the subtropical westerly jet between $20°S$ and $30°S$. Close to the coast of southern Brazil and Uruguay the flow tends to be organized as an upper level cyclonic eddy. Comparing with the low level winds in the same region (Figure 11b) we conclude that the eddy has a barotropic structure because anomalies have the same sign at upper and lower levels. This is in contrast with the baroclinic response of the atmosphere to local SST forcing seen in section D.1.

In order to find the coherent behavior of upper level wind divergence and precipitation, we applied the same analysis to both fields simultaneously. It was found that the leading joint mode consists of the first S/N-optimal for divergence and of the second S/N-optimal for precipitation (not shown). The joint mode also shows a correlation of 0.7 with Niño3 index. This result, together with previous findings about the similarities between the first S/N-optimal of divergence and the second S/N-optimal of precipitation, further suggest that these two patterns represent a single coherent structure of remotely forced SACZ variability by ENSO.

The picture emerging from above analyses is as follows. The precipitation anoma-

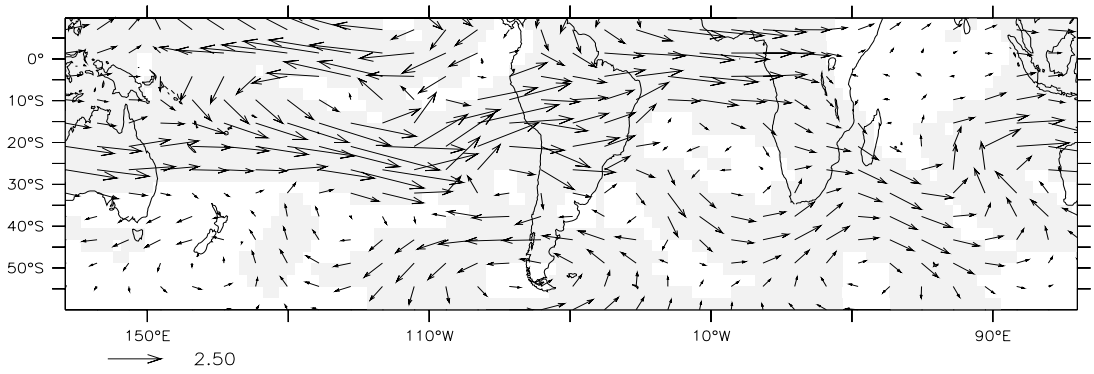

Fig. 12. Regression of 200 mb wind anomalies onto DI1. Units are m s^{-1}. Shading denotes that at least one wind component is significant to the 95% level;

lies in the SACZ region have two sources of influence: 1) a local influence due to Atlantic SST variability at interannual-decadal time scales which may be the result of modifications of the boundary layer stability properties by changes in the surface heat fluxes, and 2) a remote influence due to Pacific SST variability (at interannual time scales) which modifies the large scale upper level circulation and produces changes in precipitation. The strong tie to surface conditions can be understood by the fact that the SACZ, as the ITCZ, is a convective system that is dependent on surface SST and heat fluxes. Remote forcing from the Pacific leads to a barotropic cyclonic eddy off the east coast of South America. Although associated wind anomalies are weaker at the surface than at upper levels, they propitiate precipitation anomalies by advecting dry air to the southern part of the SACZ, and bringing moist air from the northwest to the northern part of the SACZ.

E. Discussion

The major findings can be summarized as follows:

- A significant portion of the subtropical atmosphere is governed by atmospheric internal dynamics. In the CCM3, approximately 59% of the total variance in the SACZ region can be attributed to the internal variability. For comparison, only about 20% of total precipitation variance is accounted for by internal dynamics in the ITCZ region. This suggests that the SACZ region may have much less potential predictability than the ITCZ region.

- The modeled precipitation field shows a forced response to local anomalous SST in the Atlantic Ocean on interannual-decadal time scales. It is well correlated with the first EOF of austral summertime South Atlantic SST which consists of a dipole-like SST anomaly centered at around 25°S. This pattern of SST creates a dipole-like structure in precipitation close to the coast of South America shifting the SACZ to the northeast together with a clockwise anomalous circulation of surface winds which is in geostrophic balance with the anomalous pressure. The response is localized within the South Atlantic Ocean with almost no signal over land, although there seems to be a simultaneous southward displacement of the ITCZ.

- Upper levels wind divergence shows a forced signal closely related to ENSO and is largely independent of Atlantic SST variability. This remotely forced response, which seems to exist also in the real atmosphere, has interannual time scales and produces a northeastward shift and strengthening of the SACZ during warm ENSO events. These results are in agreement with the outgoing longwave radiation (OLR) anomaly in an observational work by *Aceituno* [1988]. Model results show that the SACZ tend to shift over the land and that the northern oceanic part of the SACZ strengthens during warm events.

The above results suggest two possible interrelated mechanisms through which ENSO can exert its influence on the SACZ. First, our results show that warm ENSO events weaken the intensity of the Atlantic ITCZ in the SH summer season (Figure 11d) in agreement with *Aceituno* [1988] and *Saravanan and Chang* [2000]. In the SH summer season the Hadley cell is already weak compared with the SH winter cell. Therefore, a decrease in the ITCZ intensity during ENSO will make it even weaker. Also, the generation of a cyclonic anomaly off the coast of southern Brazil and Uruguay weakens the subtropical high locally. Consequently, the south Atlantic subtropical high becomes weaker and the poleward surface flow in its western flank diminishes. This is consistent with a northward shift of the subtropical high during warm ENSO events [*Peixoto and Oort*, 1992], as shown in Figure 11b. At the same time, the northern portion of upper level subtropical westerly jet appears to be strengthened in the Pacific sector and South American continent between $20°S$ and $30°S$ (Figure 12). According to *Kodama* [1993], the location of the SACZ is given by the convergence region between the subtropical jet in the subtropics and the low level poleward flow. In agreement with *Kodama* [1993] we found that the conditions of a weaker surface poleward flow and an anomalously strong westerly jet shifts the convergence zone to the northeast of its climatological position. This causes a decrease in precipitation in the climatological position of the SACZ which is further enhanced by the advection of dry air from the southeastward caused by the anomalous eddy. *Cook* [2000] reported a similar northeastward shift of the South Indian convergence zone during warm ENSO events.

On the other hand, the changes in the basic state associated with ENSO (Figure 12) and the shift of the mean position of the SACZ are consistent with the work of *Matthews and Kiladis* [1999]. They found that during the so called "strong (Northern Hemisphere) winters" (an index with correlation of 0.9 to Niño3.4 index) Rossby

wave-like transients are found to propagate preferentially along the strengthened subtropical jet which act as a waveguide. This finding is in line with the barotropic Rossby wave theory. *Kiladis and Weickmann* [1992] found that convection in the SACZ is modulated by upper level wave activity in the westerlies. Our analysis suggests that this mechanism may be operating on interannual time scales in the SACZ region. During warm ENSO events, we have seen evidences for the strengthening of the subtropical jet (Figure 12). Accompanying the strengthened westerly, we have observed wave-like disturbances propagating along the subtropical jet deep into the tropical South Atlantic, possibly triggering convection and shifting the mean position of the SACZ northeastward. This result seems to be consistent with the mechanism suggested by *Matthews and Kiladis* [1999]; in their Figure 3c anomalous negative OLR is seen to the north of the main position of the SACZ in a composite map of "strong winters" minus "weak winters". The result is also in agreement with the work of *Figueroa et al.* [1995] who found that inclusion of climatological flow can change the position of the SACZ.

Furthermore, *Kalnay et al.* [1986] reported observational evidence of a stationary Rossby wave during January 1979 situated at about (30°S, 50°W) associated to an intensification of the SACZ. They suggested that tropical heating could generate the waves and that a Walker type circulation associated with the SPCZ helps in their maintenance, pointing to the importance of ENSO events in modulating the convective activity in the SACZ and SPCZ. Actually, the strengthening of the SACZ in their Figures 5a and 6a seems to be accompanied by a northeastward displacement of the convergence zone from its mean position. Our findings seem to support their result that the upper level circulation in the SACZ region on interannual time scales is mainly remotely influenced by ENSO, and that warm ENSO events increase convective activity in the SACZ region.

As mentioned in the introduction, *Robertson and Mechoso* [2000] performed an EOF analysis to the NCEP-NCAR Reanalysis data set in the South American region. Their first EOF shows a strong upper level cyclonic eddy, associated with the intensification of the SACZ. The center of the eddy is situated at (30°S, 45°W) and has zonal wavenumber 6, slightly larger than the scale reported by *Kalnay et al.* [1986]. A vorticity budget analysis showed that the eddy has the characteristics of a locally forced stationary Rossby wave, and shows no correlation to ENSO. They further argue that this circulation anomaly produces a surface heat flux anomaly which generates an SST anomaly in the South Atlantic. Although they suggest that this SST anomaly may increase the persistence of the SACZ anomalies through reduced thermal damping, their results hint that changes in the SACZ are largely internally driven. *Robertson and Mechoso* [2000] also reported a second EOF which is correlated to ENSO that shows similar upper level structure as our first S/N-optimal of the divergence field, but does not seem to be connected to the SACZ variability. We can assimilate their results with ours as follows. Our results are based on a signal-to-noise optimization procedure applied to a 5-member ensemble runs to extract the dominant forced atmospheric response to local SST forcing. Accordingly, our results should give a better estimate of the forced response in the SACZ region, which is likely to differ from the leading pattern of internal variability. To check this we calculated the first EOF of the 200 mb wind field of each ensemble member and found an eddy-like pattern with similar characteristics as the "eddy" structure found in the first EOF of *Robertson and Mechoso* [2000]. We then calculated the correlations of the associated PCs with Niño3 index and found that only two of the five ensemble members showed significant correlation. This suggests that an eddy-like circulation may be a preferred mode of internal atmospheric variability at upper levels in the SACZ region (see also section F.3). This, however, does not mean that SST anoma-

lies have no impact on the variability of the SACZ. The S/N optimization procedure filters the internal variability and gives (ideally) only forced patterns. Accordingly, our first divergence S/N-optimal resembles their second EOF, and not their first one. Interestingly, these two patterns are very similar in the deep tropical area, but differ in the extratropics where internal variability is larger, suggesting that the second EOF of *Robertson and Mechoso* [2000] includes both forced and internal variability. This may be the cause why they suggest that their second EOF is not connected to the SACZ variability, while we showed above that our first divergence S/N-optimal is indeed associated to precipitation anomalies in the SACZ region.

In terms of mechanisms for local SST influence, we have presented modeling evidence that the SST anomaly in the South Atlantic can have certain influence on the SACZ variability, possibly through modifying stability properties of the atmospheric boundary layer and moisture supply needed for the development of deep convection. This local oceanic effect appears to operate on interannual-decadal time scales, and has been found quite localized, with the strongest influence region close to the coast of southern Brazil where a warm SST tongue exists during the SH summer (Figure 2a). It is possible that the thermal inertia of the ocean may act as a stabilization mechanism of atmospheric anomalies leading to an increase of their persistence [*Blade*, 1997]. This implies that the precipitation associated with the oceanic part of the SACZ region may have some predictability due to the slow SST evolution, but its land component may be mostly unpredictable. This latter result may be highly model dependent and sensitive to a different parameterization of land surface processes. It could also depend on the ensemble size. In the next section we compare a larger ensemble of SST-forced CCM3 runs to an ensemble of similar runs made with version 1.0 of the AGCM developed at the NASA Seasonal-to-Interannual Prediction Project (NSIPP-1).

F. Sensitivity of the results

The objective of this section is to address the reproducibility of the results shown before. We focus on the locally-forced precipitation signal shown in Figure 7. We are particularly interested in the extension of the precipitation anomaly toward the continental part of the SACZ, because it is highly relevant to seasonal climate forecast in a densely populated area. We shall re-examine the spatial structure of the predictable precipitation signal and quantify their strength during the peak of the SACZ in the CCM3 and NSIPP-1 models. Portions of this section have been submitted for publication [*Barreiro et al.*, 2003a].

Another major goal is to further quantify the potential predictability of the SACZ region. Identifying a forced response does not necessarily translate into high predictability, because the strength of the signal may be weak compared to the strength of the noise. Therefore, it is very important to address the issue of whether the forced response is likely to dominate the dynamics or not. A first estimate of the percentage of precipitation variability due to internal dynamics was calculated in section C. It was found that approximately 59% of the total variability in the SACZ region can be attributed to internal variability. In this section we use a different approach. We define a potential predictability measure as the ratio of the signal variance over the total variance. We further calculate the modes of precipitation associated with interannual internal variability. In this way we can compare not only the ratio of forced versus total variability, but also the spatial structure of internal variability of the two models. This allows to further compare our results with those of *Robertson and Mechoso* [2000]. We found that the precipitation in the SACZ region is largely dominated by internal variability, and that the leading modes of simulated internal variability have spatial structures that are similar to the observed leading mode of

variability in the region, e.g. *Robertson and Mechoso* [2000].

1. Data sets

To test the sensitivity of the results to ensemble size we consider a 9-member ensemble of CCM3 integrations. The four new runs of the ensemble were forced with the same observed SST as the other 5 ensemble members [*Smith et al.*, 1996], and span the same time period.

To test the sensitivity of the results to the physics of the model we use a 9-member ensemble of GOGA-type integrations made with the NSIPP-1 model. The NSIPP-1 model is a finite difference model with a resolution of 2.5 degrees in latitude and 2 degrees in longitude with 17 levels in the vertical, e.g. [*Suarez and Takacs*, Greenbelt, MD, 1995]. The output of the NSIPP-1 was regridded to a 2.5 x 2.5 grid to compare better with observations and with CCM3 output. Data for the NSIPP-1 model can be obtained via the website *http://nsipp.gsfc.nasa.gov/main.html*. As the CCM3, the deep convective parameterization used in the NSIPP-1 model is a variant of the Arakawa-Shubert (AS) [*Arakawa and Shubert*, 1974] mass flux scheme. However, instead of using the Zhang-McFarlane scheme, the NSIPP-1 model uses a Relaxed-Arakawa-Shubert scheme for penetrative convection originating in the boundary layer [*Moorthi and Suarez*, 1992]. The main difference with AS is that the state is "relaxed" toward equilibrium rather than requiring the final state to be balanced. The land surface models (LSM) used in the NSIPP-1 is also different than the one used in the CCM3 (see section B). The LSM used in NSIPP-1 is a soil-vegetation-atmosphere-transfer scheme developed by *Koster and Suarez* [1992, 1996], called MOSAIC LSM. MOSAIC subdivides each grid square of the atmospheric model into tiles of a single vegetation type, and then calculates separate one-dimensional energy and water balances over each tyle with strong stomatal control over transpiration rates.

The 9-member ensemble of NSIPP-1 integrations span the period 1930-2000, and the imposed SST (all in a 2.5 x 2 grid) were given by the Hadley Centre SST data set during 1930-1948, GISST 2.2 during 1949-1981 (reconstructed using eigenvectors of in situ observations, *Rayner et al.* [1996]), and Reynolds Optimal Interpolation SST v1.0 during 1982-2000 (combines in situ- and satellite-derived SST data, *Reynolds and Smith* [1994]). Since the three data sets have different climatologies we calculated anomalies by removing the corresponding climatology in each of the periods. This procedure should not affect the results because we will not analyze interdecadal variability.

In this section we validate model results with the observational rainfall data set given by the Global Precipitation Climatology Project (GPCP, [*Huffman et al.*, 1997]), which is on a global 2.5 x 2.5 grid, and spans the time period 1979-2000. The GPCP data set, as the Xie-Arkin, is derived from satellite- and raingauge-based observations. The global distribution of rainfall from both data sets matches each other. However, regional differences arise due to the use of different merging techniques and components. These differences can be considered as a measure of the uncertainty in the observations. A comparison between the two data sets can be found in *Gruber et al.* [2000].

Figures 13a and 13c show the climatology of rainfall during JFM season for NSIPP-1 and observations during the common period of 1979-1994, respectively. The corresponding climatology for the CCM3 is shown in Figure 2a. The connection of the SACZ with the Amazon convective region is apparent in the observations, and in the CCM3 model, but is less clear in the NSIPP-1 model. The separation between the rainfall bands associated with the SACZ and ITCZ is well captured in the models. However, contrary to observations the NSIPP-1, as the CCM3, tends to locate the ITCZ's axis south of the equator, and overestimate rainfall next to the

coast of Brazil at about 15°S, resulting in the undersizing of the Atlantic dry zone. On the other hand, the simulated SACZ does not extend as far southeastward as the observed one. The GPCP climatology shows a clear discontinuity of the SACZ band near the coastline which hints that the continental and oceanic parts of the SACZ do not vary as an integrated structure. This feature is not as clear in the Xie-Arkin climatology (Figure 2e). The NSIPP-1 model also shows this discontinuity, but is less obvious in the CCM3. The maximum precipitation in the NSIPP-1 model is over land, comparing well with observations.

The CCM3 model captures the interannual variability of the SACZ with the maximum over the continent and extending southeastward over the ocean (Figure 2d). The NSIPP-1 model, on the other hand, underestimates the precipitation variability over the continent and shows maximum variance over the oceanic portion of the SACZ (Figure 13b). The origin of the underestimation of precipitation over land is uncertain, but is likely related to the parameterization of land surface processes and their interaction with the atmosphere.

2. Detection of forced response

As in section D, we used the S/N optimization procedure to find the forced signals in the precipitation. In section D, the first two optimals with maximum signal-to-noise variance ratio were considered as the forced signals. Here we proceed in a slightly different manner which is perhaps more accurate and physically more sound: we first construct a total forced signal by summing up all the optimals that have a S/N-ratio larger than unity. The dominant forced pattern is then calculated as the first EOF of the total signal variance (see also Appendix A). The analysis below indicates that the first EOF of the total signal and the first optimal are very similar in both spatial and temporal structures. The time series are highly correlated with a correlation

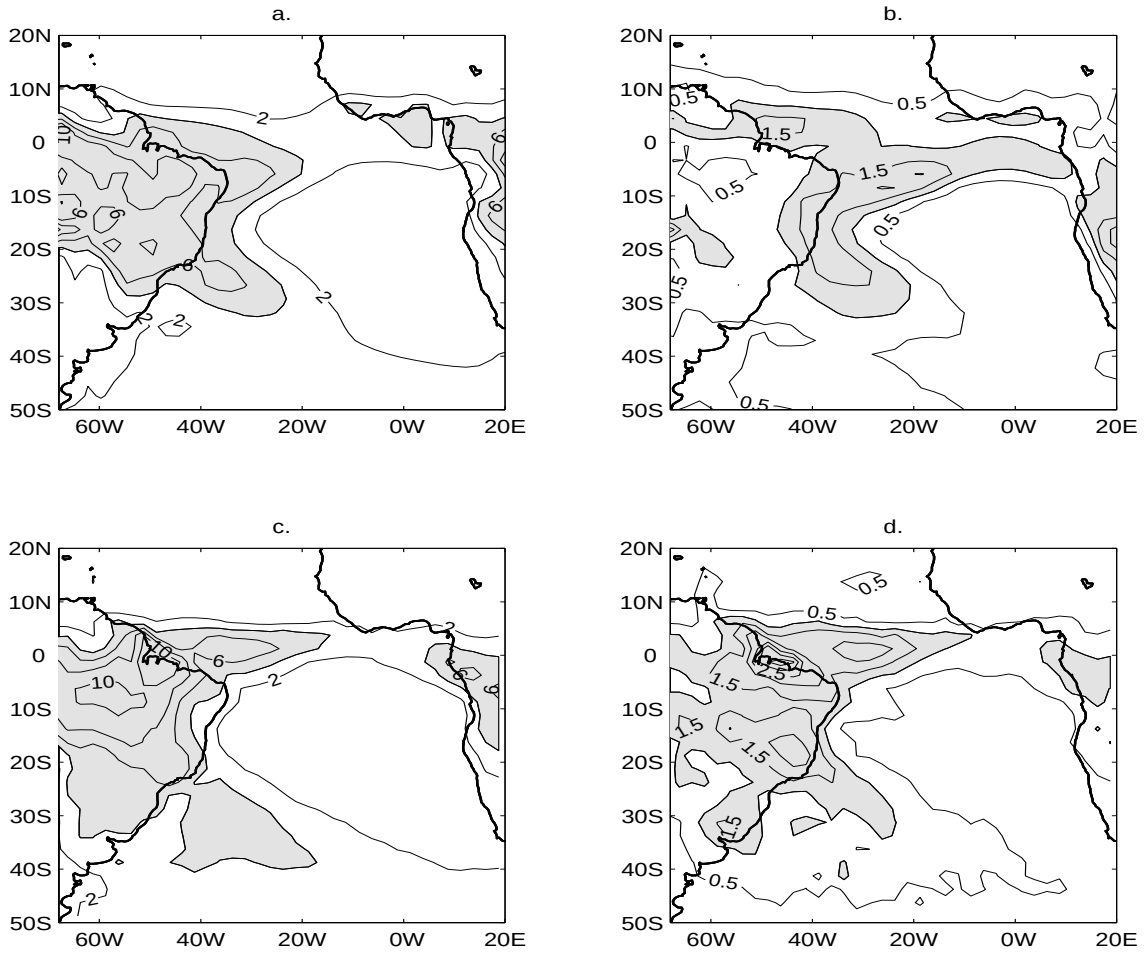

Fig. 13. JFM precipitation climatology and RMS deviation during the period 1979-1994 for: (a), (b) NSIPP-1 model, and (c), (d) GPCP, respectively. Contour interval is 2 mm day^{-1} for climatology (left panels), and 0.5 mm day^{-1} for RMS deviation (right panels). The dashed boxes mark the SACZ region.

coefficient r larger than 0.95 for the data sets we have considered.

We applied the procedure described above to the precipitation fields of CCM3 and NSIPP-1 models. The analysis is performed over their respective time periods, that is, 1950-1994 for CCM3, and 1930-2000 for NSIPP-1. We consider a longer period for the NSIPP-1 to use all the available data, and also because it overlaps the observational record. The use of NSIPP-1 data only in the common period 1950-1994 does not change the main results. For the CCM3 model the pattern of forced response in the SACZ region using the 9-member ensemble is very similar to the one calculated using a 5-member ensemble and shown in Figure 7 (not shown). The associated time series are highly correlated as well.

Figure 14 shows the dominant forced pattern for the NSIPP-1 model. Anomalies in the SACZ region are very similar in structure and amplitude to those of the forced signal found in the CCM3 (see Figure 7c). The response consist of a northwest-southeast oriented dipole in precipitation anomalies mainly located off the coast of Brazil, as was found for the CCM3. The northern lobe of the dipole is stronger than the southern lobe, indicating a northward shift of the SACZ as well as a strengthening of rainfall in that region. The time series associated with the signals show interannual-to-decadal time scales and are correlated with $r = 0.77$ over the common period 1950-1994, which is significant at 99% level.

Regression of SST onto the time series of the forced response reveal that, as in the CCM3, the enhanced precipitation is located over warm SST anomaly with a maximum of roughly 0.45°C at about 20°S (compare Figure 14b with Figure 7a). The cross-equatorial SST gradient is consistent with the weakening and southward shift of the ITCZ seen in Figure 14a (also found in the CCM3). Regression of 1000mb winds show a cyclonic eddy located over the same region off the coast of Brazil in both models, as well as northerly flow coming from the equatorial region into the SACZ.

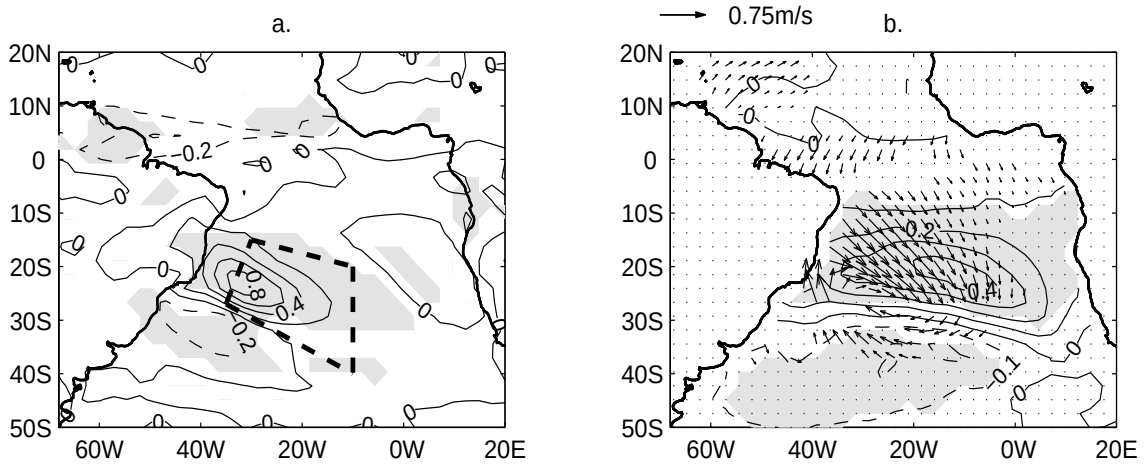

Fig. 14. (a) Dominant forced signal of precipitation for NSIPP-1 model, shown as a homogeneous regression map over a larger region. (b) Regression of 1000 mb winds and SST onto the time series of the forced signal. Contour interval for the SST is 0.1 K. Shaded areas indicate SST significant at the 95% level. Only wind vectors where the wind speed anomaly is significant at the 90% level are plotted. The dashed box in (a) marks the region used to construct the precipitation index shown in Figure 18c.

Therefore, despite the different physical parameterizations, both GCMs present a very similar forced response of the atmosphere to local SST. Anomalies are larger in the CCM3 in part because the regression for NSIPP-1 encompasses the period 1930-1960 in which the signal was relatively weak.

Figures 15a and 15b show the regression of the net heat flux into the ocean for both AGCMs (note the similarity between Figure 15a and Figure 7d). Heat flux anomalies are generally stronger in the CCM3 model. Moreover, model responses differ in the SACZ region. At about (20°S, 35°W) the CCM3 presents a net heat flux anomaly into the ocean coexisting with positive SST anomalies, suggesting a local positive air-sea feedback, which is not present in NSIPP-1. On the other hand, both models tend to suggest a positive feedback between heat fluxes and SST off the coast of Brazil at about 10°S. There, the heat fluxes tend to maintain and shift northward the SST anomaly.

To investigate further we separated the heat flux budget into four components: shortwave and longwave radiation, and latent and sensible heat fluxes. In both models the net heat flux ($Nhflx$) is approximately given by the difference between the downward solar radiation (Sw) and the latent heat flux ($Lhflx$), i.e. $Nhflx \simeq Sw - Lhflx$. The NSIPP-1 model shows a negative anomaly of downward solar radiation at the same place of increased precipitation, suggesting that the presence of clouds shadows the surface to incoming energy thus acting as negative feedback (see Figure 15d). To both sides of the negative anomaly there are areas with increased solar radiation probably consequence of compensating subsidence which inhibits cloud formation. The CCM3 shows similar behavior in shortwave radiation except for a region of positive anomaly next to the coast of Brazil which suggests positive feedback (see Figure 15c). The regression maps of the latent heat flux reveal that both models show negative anomaly next to the coast of Brazil at about 10°S. In the CCM3, however, the

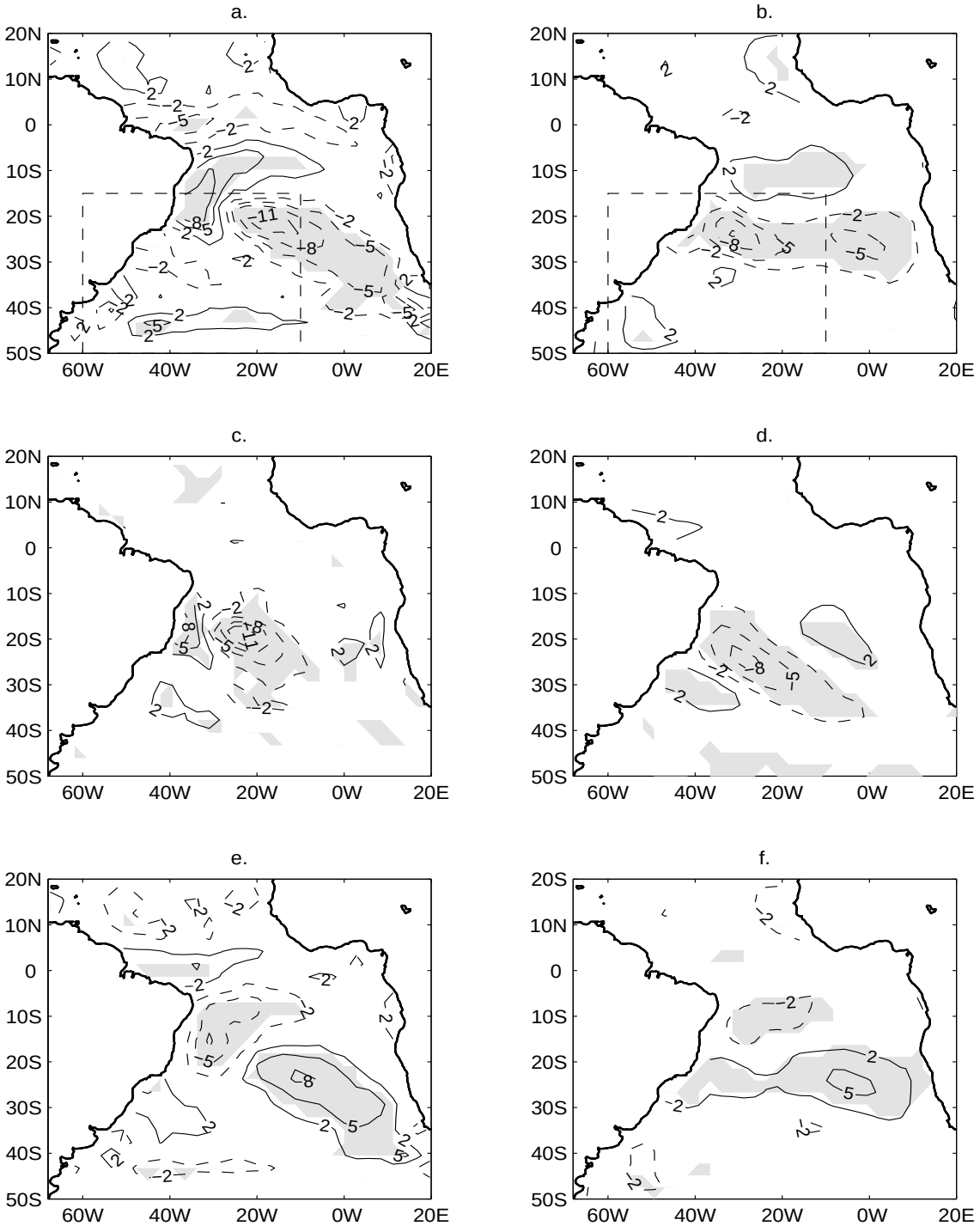

Fig. 15. Regression of heat flux onto the time series of the forced response for the CCM3 (left) and NSIPP-1 (right) models. (a), (b) net heat flux into the ocean; (c), (d) downward solar radiation; (e), (f) latent heat flux. Units are W m^{-2}. The boxes in (a) and (b) mark the SACZ region.

anomaly extends further south to 20°S contributing with the solar radiation anomaly to create the region of positive feedback in the SACZ region mentioned above (see Figures 15e and 15f). The origin of these model differences is not clear at the moment, but is expected to be related to the different parameterizations of convection, of boundary layer processes, and of cloud-radiation interaction. Sensitivity experiments are needed to further investigate this result.

3. Internal variability

We followed the procedure described in Appendix A to calculate the leading patterns of internal variability on interannual time scales. The EOF analysis is performed over the concatenated noise parts of ensemble members to enhance statistical significance.

Figures 16a and 16b show the patterns of the leading EOF of the noise (hereafter noise-EOF1) for each model. They explain 25% and 32% of total noise variance in the CCM3 and NSIPP-1 models respectively. The structures of the noise-EOF1 in both models are very similar, mainly showing an enhanced SACZ accompanied by decreased precipitation to its southwest consequence of compensating subsidence. There is also a decreased of precipitation in the ITCZ. One notable difference between the noise patterns is that in the CCM3 the maximum variance is over the continent, while in the NSIPP-1 the maximum is over the continental part. This difference in structure mimics differences in maps of RMS deviation (Figures 13b and 13d). The regression of 200mb winds onto the time series associated with noise-EOF1 in the CCM3 shows a cyclonic eddy centered at about (45°W, 30°S) accompanying a strengthened SACZ (Figure 17). Thus, the noise-EOF1s tend to have the same spatial structure as the leading mode of variability in the SACZ region found in *Robertson and Mechoso* [2000] using the NCEP-NCAR Reanalysis data set.

They also found that this mode is largely due to internal variability of the atmo-

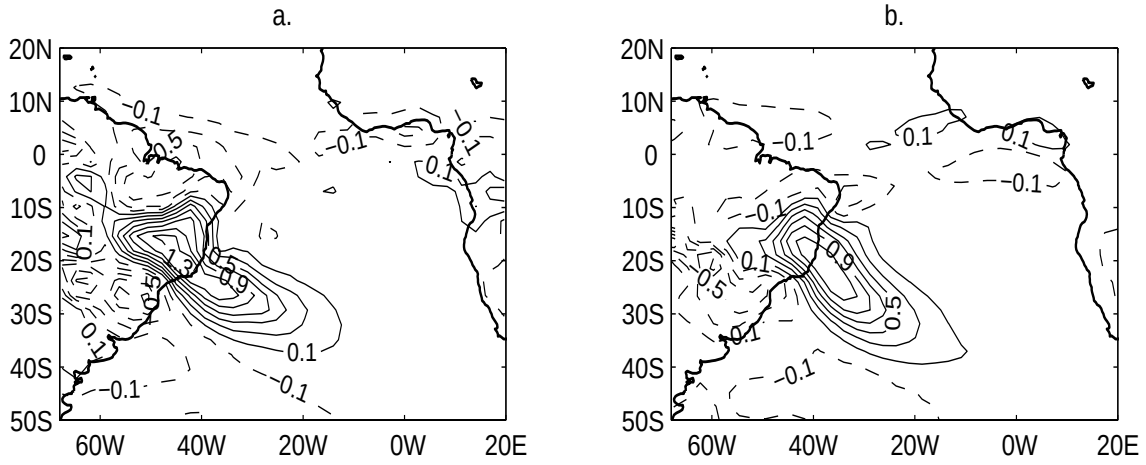

Fig. 16. The dominant mode of internal variability for precipitation (noise-EOF1) in (a) CCM3, and (b) NSIPP-1 models. Contour interval is 0.2 mm day^{-1}.

sphere, which agrees with our findings, and that the associated time series contains a periodic component of 15-17 years. The time series of the noise-EOF1s, however, have very large within-ensemble variability, showing almost no significant correlation between time series of different ensemble members (as expected for noise). Thus, it suggests that the leading noise patterns have no preferred time scale. As mentioned above the EOF technique used in *Robertson and Mechoso* [2000] is not designed to separate forced from internal variability, but to maximize explained variance. Thus, although largely due to internal variability, their leading mode will likely include also a component from forced variability, which may explain the significant periodic component in the associated time series. Also, as *Robertson and Mechoso* [2000] pointed out, the 40-year time series they used in their study is too short to conclusively reject the null hypothesis that the periodicity arises from random sampling variations.

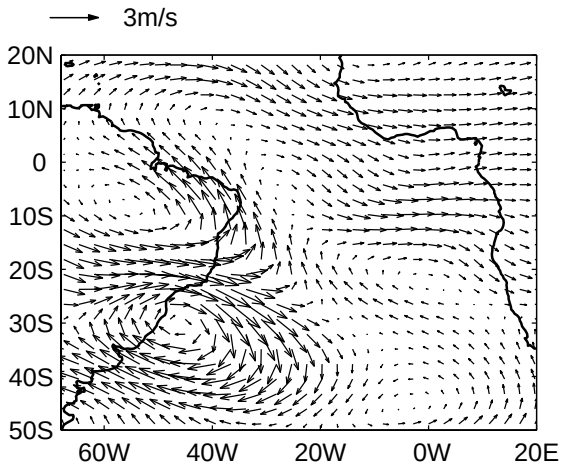

Fig. 17. Regression of 200mb winds onto the time series associated with the noise-EOF1 of CCM3.

4. Potential predictability analysis

The previous sections have focused on the temporal and spatial structures of the forced and internal variability of the precipitation in the SACZ region. In this section we investigate the issue of how predictable the precipitation is, and where the predictable region lies, assuming that SST is known in advance.

To do so we constructed the potential predictability index PP as described in Appendix A, that is, $PP = \sigma_s^2/\sigma_t^2$, where σ_s^2 is the variance of the signal and σ_t^2 is the total variance. Regions where $PP > 0.5$ are those where prior knowledge of the surface oceanic conditions may allow the prediction of precipitation anomalies in advance.

Several approaches have been developed to measure potential predictability using an ensemble of climate simulations. Some approaches define a coherence index which "reflects the ability of the SSTs to guide the time sequencing of precipitation anomalies" [*Koster et al.*, 2000], whereas others are based on "Analysis of Variance" (ANOVA) methods, e.g. [*Rowell*, 1998]. Estimates of potential predictability have

usually been of global extent, and have not focused on the SACZ region. Moreover, while ANOVA is a useful indicator of SST influence, it does not take into account of correlations between grid points, which may lead to the erroneous conclusion that there are no SST effects. The measure of potential predictability used here explicitly accounts for correlation between neighboring points because it constructs the total signal as the sum of optimal structures calculated in the SACZ region. A weakness of the technique to estimate PP is that the construction of σ_s^2 depends on the truncation of the optimals. In this work we used S/N-ratio larger than unity as a criterion for truncation. This choice of truncation is somewhat arbitrary and does not give a measure of the bias in the estimation of the true signal. This methodology of truncation may led to an under or overestimation of the true signal. Thus, there is no obvious way to calculate the statistical significance of PP. To partially address this issue we compare PP with the estimate of potential predictability given by a 1-way ANOVA model (PP_A), in which the significance level can be computed. The main idea of ANOVA is as follows: Assuming that the SST-forced variability and the internal variability are independent, ANOVA tests for the significance of SST effects on a certain atmospheric variable comparing the variance of the ensemble mean with the variance of the deviations from the ensemble mean (noise variance) at each grid point. The signal variance is estimated as the variance of the ensemble mean biased-corrected to account for a finite ensemble size. The potential predictability estimate is then computed as the ratio between the signal variance and the total variance (sum of signal and noise variances). Appendix A presents a summary of the ANOVA results used here, and provides references on the technique.

Figures 18a and 18b show the potential predictability measure PP for each model. Overall both models agree in that the variance of the predictable signal explains less than 10% of total variance over the continent, and that it is significantly

larger over the oceanic portion of the SACZ, mainly to the north of the SACZ's climatological axis. However, the potential predictability in the CCM3 model is larger than in the NSIPP-1 model in spite of the fact that the forced signals in both models are of about the same amplitude This is also true when considering the NSIPP-1 output during the period 1950-1994 only, although PP increases. The reason is related to the structure of the noise in the models. In the CCM3 the noise-EOF1 has largest variability over the land and not so strong over the ocean. In the NSIPP-1, on the other hand, the noise-EOF1 has largest loading over the oceanic part of the SACZ, thus hindering the forced response.

Estimates of potential predictability given by ANOVA (PP_A) are very consistent with those of the PP index (Figures 18c and 18d). They also tend to agree with the results of *Rowell* [1998], and of *Koster et al.* [2000] despite the slightly different season considered (they used December-January-February). Nevertheless, ANOVA estimates are larger for both models, particularly for the NSIPP-1, showing that PP gives a conservative estimate of the potential predictability.

Figures 18a and 18b indicate that over the ocean the predictable variance has a maximum value of about of 60% of total variability, but the mean over the ocean is considerably smaller than that. This suggests that the internal variability dominates in the SACZ region in agreement with previous estimates of section C, and with results of *Robertson and Mechoso* [2000]. The signal variance accounts for a relatively large portion of the total variance only in the positive lobe of the forced precipitation dipole pattern, and the maximum is shifted further away from the coast compared with Figures 7c and 14a, due to the extension of the noise variance toward the ocean.

The above results suggest that the ocean surface is a source of potential predictability to the oceanic portion of the SACZ. Also, they indicate that it is in that region where the forced signal shown in Figure 14a is likely to be an important player

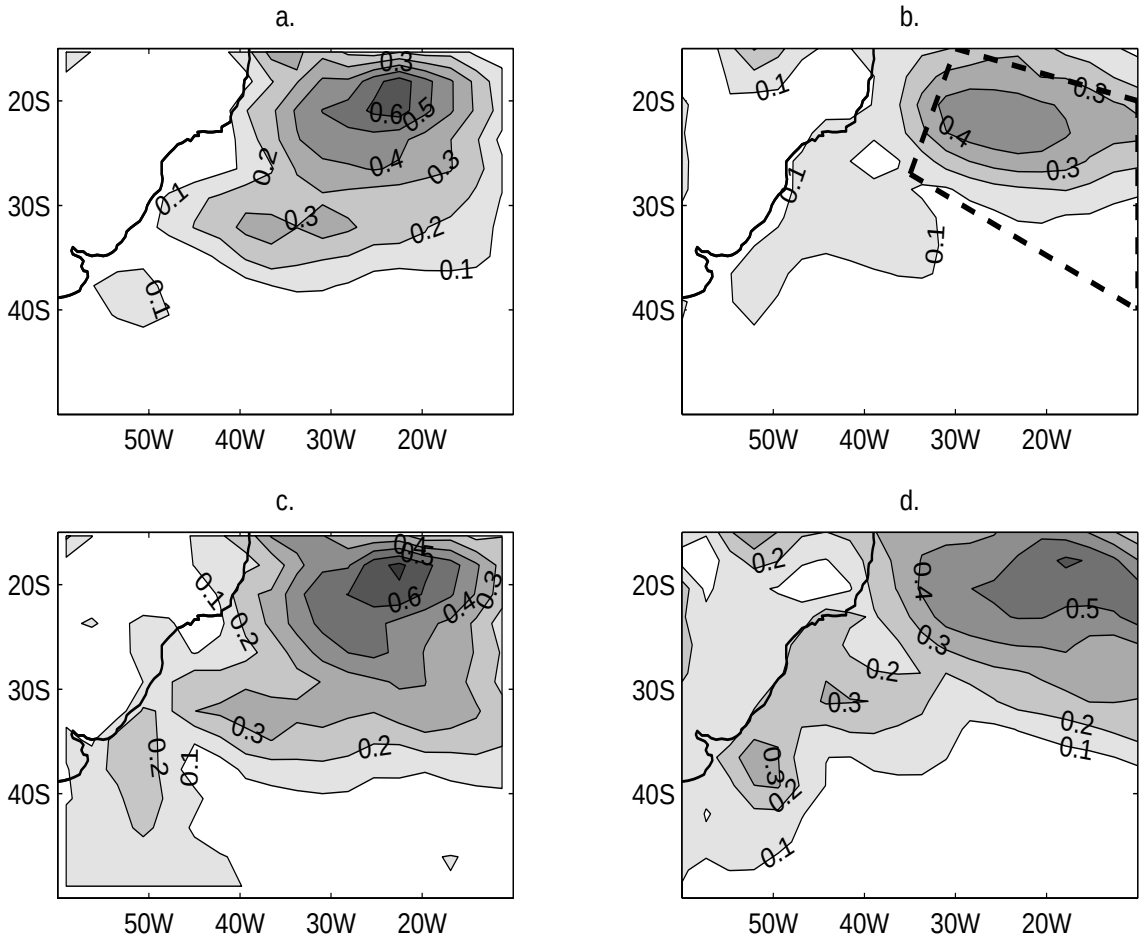

Fig. 18. Estimates of potential predictability given by PP index for (a) CCM3 and (b) NSIPP-1 models; and given by ANOVA (PP_A) for (c) CCM3 and (d) NSIPP-1 models. For PP_A contours larger than 0.1 are significant at 99% level. The dashed box in (b) marks the region used to construct the precipitation index shown in Figure 14a.

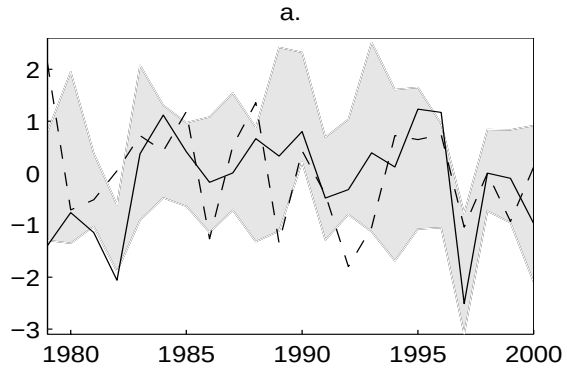

Fig. 19. Time series of forced response in NSIPP-1 (solid line) and time series of the precipitation index in the observations (dashed line). Shading shows the dispersion of the index for precipitation calculated for all NSIPP-1 ensemble members (see text).

in the dynamics. These results, however, are derived based on ensembles of model simulations, and do not address directly the issue of how skillful these models are in simulating/predicting observed rainfall in the region on interannual time scales. To address this issue we constructed a precipitation index as an average over the area shown in Figure 18b. The choice of the area is based on the criterion that the forced variance must explain at least 30% of the total variance in both models. The southern limit is defined by the axis of the forced precipitation dipole (see Figure 14b). Also, note that the area follows the shape of the positive lobe in the precipitation dipole and that it contains the region of maximum amplitude.

Figure 19 shows the index for the observational data set (dashed line) together with the time series of the forced response for the NSIPP-1 (solid line). The shaded region denotes the dispersion of the precipitation index calculated for the ensemble members. As expected due to the relatively large noise variance in the region, the index shows large intra-ensemble dispersion. Note that the dispersion interval almost always contains the time series of the forced response. The index for the observations

also generally lies within the dispersion of the ensemble members, suggesting that the model simulates well the precipitation variability in the region. Moreover, the observed precipitation index shows a correlation of 0.45 with the time series of the forced response during the period 1980-2000, which is significant at the 95% level. These results suggest that the forced response of the precipitation to SST anomalies is present not only in the models, but also in the real atmosphere. However, this also suggests that the forced signal is weak and its manifestation is confined away from the coast where internal atmospheric dynamics is weaker.

G. Summary

In this first part of the dissertation we studied the interannual and decadal variability of the SACZ during austral summer (JFM season). An attempt is made to separate the forced variability from the internal variability. This is accomplished by applying a signal-to-noise optimization procedure to an ensemble of multi-decadal integrations of the latest version of the NCAR Community Climate Model (CCM3) forced with observed SST. The result yields two dominant forced atmospheric responses: a local response to Atlantic SST anomalies with interannual-decadal time scales and a remote response to Pacific SST anomalies at interannual time scales. The latter manifests itself mainly in the upper level circulation, consisting of a northeastward shift of the SACZ with associated rainfall anomalies during warm ENSO events.

The precipitation response to local SST anomalies is localized within the South Atlantic Ocean with almost no signal over land, consisting of a dipole-like structure in precipitation close to the coast of South America accompanied by a clockwise anomalous circulation of surface winds. The sensitivity of this precipitation response on model physics was investigated by comparing the output of the NASA/NSIPP-

1 model with that of the CCM3. We found that despite the different convective and land-surface parameterizations, the two models consistently show an SST-forced signal located mainly over the oceanic portion of the SACZ, consisting of a shift and strengthening of the SACZ towards anomalous warm waters. We suggest the following mechanism to explain the forced signal: a positive SST anomaly forces the atmosphere, generating a low level hydrostatic cyclonic eddy next to the coast of South America. A northerly flow coming from equatorial regions, probably as response to the tendency of having warmer SST anomalies to the south of the equator, is also present, thereby, bringing enhanced moisture to the area. This anomalous circulation creates a convergence in the northern part of the SACZ, causing increase in precipitation. Compensating subsidence forms to its southwestern flank and creates a negative precipitation anomaly, which may further be reinforced by the low moisture southerly flow.

The leading mode of precipitation associated with the internal variability on interannual time scales is also calculated. Its structure is somewhat dependent on the model, but it tends to show an enhanced SACZ accompanied with decreased rainfall over southern Brazil, Uruguay and northern Argentina (or vice versa). This structure is very similar to the leading pattern of observed vertical velocity found in *Robertson and Mechoso* [2000].

A potential predictability analysis reveals that the maximum predictable variance in the SACZ region is about 50% of the total SACZ variance over the ocean, but the signal attenuates rapidly towards the South American continent. This feature is found in both the CCM3 and the NSIPP-1 models, and implies that the land portion of the SACZ is primarily dominated by the internal variability, thereby having a limited potential predictability at seasonal time scales. Accordingly, the only hope for prediction beyond the one-to-two weeks limit imposed by the chaotic atmospheric

dynamics may rely on the foreknowledge of the land surface moisture state [*Koster et al.*, 2000]. The coastal region may still have some predictability associated to SST anomalies, which needs to be addressed using regional high resolution models with improved land physics and convective parameterizations.

CHAPTER III

ON THE ROLE OF THE SOUTHERN HEMISPHERE ATMOSPHERIC CIRCULATION IN TROPICAL ATLANTIC VARIABILITY

A. Introduction

The variability associated with an anomalous hemispheric SST gradient coupled to a cross-equatorial atmospheric circulation and the displacement of the ITCZ during the boreal spring (March-April-May, hereafter MAM) has long been recognized as one of the most important components of Tropical Atlantic Variability (TAV), e.g. [*Hastenrath*, 1985]. This pattern of variability, which we refer to as the gradient mode, is shown in Figure 20. Clearly, rainfall over the north Northeastern region of Brazil is highly affected by this mode. Understanding and predicting the onset and development of this phenomenon is one of the central focuses of TAV research.

Hastenrath and Greishar [1993] proposed the following mechanism for the coupling between SST, winds and convection [*Chiang et al.*, 2002]: an anomalous cross-equatorial SST gradient generates surface winds from the cooler to the warmer hemisphere through the hydrostatic effect of SST on sea level pressure [*Lindzen and Nigam*, 1987]. Afterward, the anomalous cross-equatorial winds will in turn influence the position of convection. This causal linkage was later supported by observational studies [*Ruiz-Barradas et al.*, 2000], and modeling studies [*Chang et al.*, 2000]. The observed seasonality of this coupling is believed to be a result of the spatially uniform warm climatological SST condition in boreal spring that makes the Atlantic ITCZ highly sensitive to perturbations in the meridional direction [*Chiang et al.*, 2002]. These authors also argued that during this season even a small pressure gradient can drive significant cross-equatorial flow. The original SST anomalies that force the

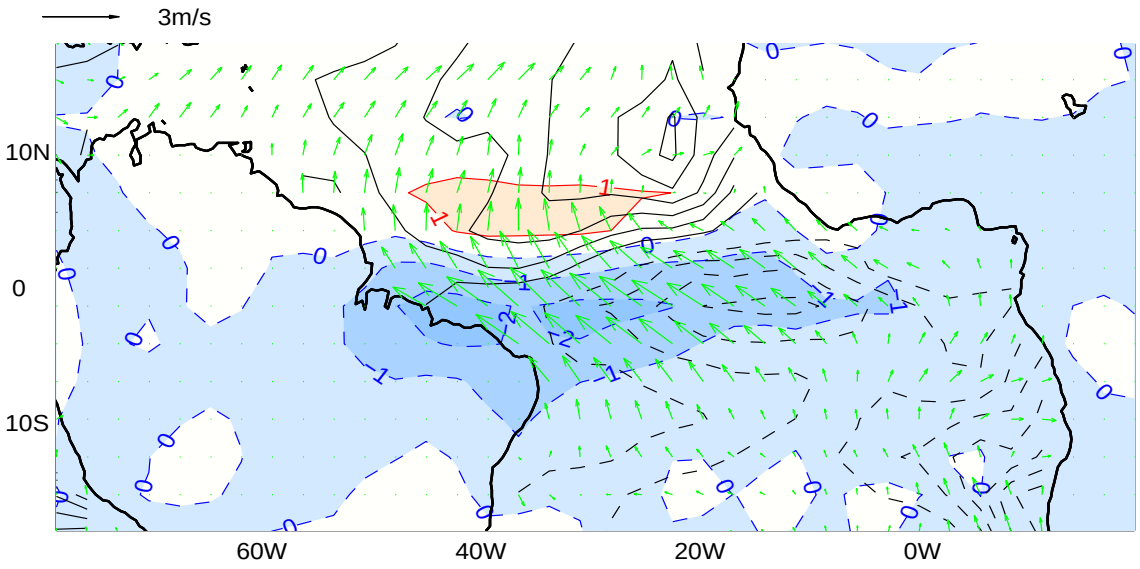

Fig. 20. The gradient mode of variability during boreal spring, calculated as the leading joint SVD of surface wind speed and SST from 1982 to 2000. The contours show the SST anomalies (contour interval is 0.1K). Arrows depict the NCEP-NCAR 925mb winds. The filled contours depict the regressed precipitation (from Xie-Arkin) in units of mm day^{-1}.

atmosphere have been shown to be preceded by changes in the trade wind system, indicating an atmospheric origin for the SST anomalies *Carton et al.* [1996]; *Nobre and Shukla* [1996].

These findings have resulted in two main paradigms for this phenomenon. Based on modeling and observational studies some investigators have proposed that the gradient mode can be explained by a merely passive response of the ocean to atmospheric forcing [*Dommenget and Latif*, 2000; *Seager et al.*, 2000]. The SST anomalies created by wind-induced heat fluxes will afterward force the atmosphere. Other studies, trying to explain a decadal spectral peak of the gradient mode suggest that there exists a positive air-sea feedback between the SST and the wind-induced heat fluxes, sometimes referred to as the wind-evaporation-SST (WES) feedback [*Chang et al.*, 1997; *Xie*, 1999]. This feedback is thought to work as follows: as the SST-driven surface winds cross the equator they change direction due to the action of the Coriolis force such that they tend to reinforce (weaken) the trade winds of the cold (warm) hemisphere. Thus, they enhance the heat flux anomalies that induced the original SST anomalies, leading to a positive feedback loop. *Chang et al.* [2000, 2001] recently proposed an alternative hypothesis that acknowledges the importance of remote forcing as well as of local air-sea feedbacks. In that view the gradient mode is a damped mode forced by atmospheric variability and the positive feedback between SST and heat flux operates only between about 15°S and 15°N. Observational evidence of the positive air-sea feedback can be found in *Chiang et al.* [2002]; *Czaja et al.* [2002].

The importance of the existence of a positive feedback cannot be overstated, because its existence may be very important for extending the dynamical seasonal prediction in the Atlantic region. From the above discussion, it is also clear that identifying and understanding sources of the origin of the SST anomalies are important aspects of TAV research. Among the known sources of the origin of SST anomalies

in the tropical Atlantic are ENSO in the equatorial Pacific, e.g. [*Curtis and Hastenrath*, 1995; *Enfield and Mayer*, 1997], and the NAO in the northern extratropics, e.g. [*Marshall et al.*, 2001]. Both of these phenomena reach their full strength during the boreal winter, thereby affecting the formation of the SST gradient during the boreal spring. Studies show that these remote influences are mostly confined to the Tropical North Atlantic (TNA). According to *Chang et al.* [2001] these remote influences play an important role in exciting local air-sea feedbacks in the deep tropical Atlantic region.

The impact of ENSO on TAV is well documented [*Enfield and Mayer*, 1997; *Saravanan and Chang*, 2000]. The wind-induced latent heat flux change in the TNA region associated with ENSO has been identified to be a plausible mechanism: During warm ENSO events diabatic heating anomalies in the eastern tropical Pacific cause the northeasterly trades in the tropical Atlantic to weaken during boreal winter. As a result of the reduced strength in the trades, the evaporational heating decreases, which in turn causes the SST in the TNA to warm up. *Chiang et al.* [2002] and *Giannini et al.* [2001] show that ENSO generally tends to aid the development of an SST gradient in the following spring. However, the anomalous gradient can also form without the presence of ENSO, as demonstrated by *Chiang et al.* [2002]. This latter result underlies the importance of local feedbacks. In fact, a recent study by *Giannini et al.* [2003] suggests that the local feedbacks can interfere with the remote influence of ENSO.

The effect of NAO on TAV has also been previously noted, e.g. [*Visbeck et al.*, 1998]. The NAO is the dominant mode of internal atmospheric variability (IAV) during winter of the Northern Hemisphere (NH), and its primary forcing mechanism is thought to be eddy-mean flow interaction on synoptic time scales [*Marshall et al.*, 2001]. The oceanic response to the NAO forcing consists of a tripole pattern of SST

anomaly, extending from the high latitudes of the North Atlantic to the northern tropics with decreasing amplitude. The maximum SST anomaly lags the NAO forcing by approximately a season and occurs during MAM. The southernmost lobe of the tripole occupies a large portion of the TNA where trade wind changes consequence of sea-level pressure fluctuations associated with the NAO are presumably responsible for the generation of the SST anomaly via latent heat flux. One interesting feature noted from both an observational analysis [*Czaja et al.*, 2002] and a modeling study [*Chang et al.*, 2001] is that the SST anomaly generated by the NAO appears to be largely confined to the north of the equator with largest SST anomaly north of 10°N.

To date, the possibility of a southern hemispheric origin of SST anomalies in the tropical Atlantic has not been explored. During austral winter (June-July-August, hereafter JJA) the Atlantic subtropical anticyclone in the SH is most energetic [*Satyamurty et al.*, 1998], and is located in its westernmost and northernmost position [*Hastenrath*, 1985]. Therefore, variability in the subtropical high during this season is most likely to have an influence in TAV. *Venegas et al.* [1997] found that the leading mode of observed coupled atmosphere-ocean variability in the South Atlantic consists of a weakened/strengthened subtropical anticyclone forcing the ocean. In this chapter we will take a further look at the variability in the South Atlantic during austral winter, and investigate how the changes induced by internal atmospheric variability can force the ocean below, and consequently influence the onset and development of the gradient mode. We analyze both observations and an ensemble of AGCM simulations. Portions of this chapter have been submitted for publication [*Barreiro et al.*, 2003b].

The chapter is organized as follows. In sections B and C we motivate the discussion by describing the observed evolution of SST and circulation anomalies during non-ENSO years characterized by significant TAV in MAM. Composites show that the anomalous spring gradient is preceded by SST anomalies in the southern subtropics

created during the previous austral winter. In section D we describe the model used to further investigate the influence of the Southern Hemisphere (SH) IAV on TAV. We describe the evolution of simulated SST anomalies generated by IAV during austral winter, and propose a mechanism to explain its influence on TAV. To compare with the remote SH winter influence on TAV, we review the evolution of SST anomalies induced by the NAO in the context of our model. Section E summarizes the results, and the last section discusses implications of our findings.

B. Evolution of the gradient mode from observations

1. SST evolution

To investigate the linkage between the Atlantic gradient mode during boreal spring and the SH atmospheric variability, we first performed a composite analysis based on the reconstructed SST data set of *Smith et al.* [1996]. The data has a spatial resolution of approximately 2.8 degrees and spans from January 1950 to December 1994. All data sets considered in this study were linearly detrended prior to analysis. To track the SST evolution that leads to the gradient development during MAM, we first derived seasonally averaged SST anomalies. We then constructed the composite of the SST anomalies for MAM (when the gradient is at its peak) and three seasons prior to that. Therefore, our composite calendar begins in the boreal summer June-July-August of year 0 (JJA0), and ends in the March-April-May season of year +1 (MAM+1). This results in a record of 44 years of SST anomalies, starting in JJA of 1950 and ending in MAM of 1994.

Since our focus is on the remote influence from the extratropics, we remove ENSO influences by eliminating all the years when there is an ENSO event in the tropical Pacific. These years are defined as those when the December0/January+1

Niño3.4 index (the average of SST anomalies in ($120-170$°W,5°S$-$5°N)) is larger than 0.75°K. This classification leads to the following warm events: 1958, 1966, 1969, 1970, 1973, 1983, 1987, 1988, 1992, and the following cold events: 1951, 1955, 1956, 1965, 1971, 1974, 1976, 1985, 1989 (years refer to the January+1 month). We remove these 18 ENSO years from the data set, and only keep the remaining 26 non-ENSO years for the analysis.

Non-ENSO years were further classified according to a gradient index (GI), which characterizes the strength of the cross-equatorial SST gradient in MAM+1. The GI is defined as the difference between averages of SST anomaly in the regions ($4°-14°$N, $60°-30°$W) and ($4°-14°$S, $40°-10°$W). Other authors have considered indices over larger regions, e.g. [*Chiang et al.*, 2002], to characterize the SST gradient. Although results do not change substantially, we choose to consider regions in the deep tropics because it is here that an SST gradient can strongly influence the ITCZ position. Throughout this study we refer the region ($4°-25°$N, $60°-15°$W) as the tropical North Atlantic, and the region ($4°-25°$S, $15°-45°$W) as the tropical South Atlantic (TSA).

We define positive/negative gradient years as those having a GI exceeding the standard deviation, that is, GI$\geq|\ \sigma\ |$ (where σ is the standard deviation of the time series excluding the ENSO years). Note that negative (positive) years correspond to a situation in which SST anomalies are warmer (cooler) south of the equator. Remaining years are classified as neutral. According to this classification, there are 5 positive gradient years (1978, 1979, 1980, 1981, 1993) and 4 negative gradient years (1964, 1975, 1984, 1986) in the observed record. The positive gradient years overlap substantially with the ones chosen by *Chiang et al.* [2002] for their gradient composite.

Assuming that the coupled system's response is linear, we further consolidate the anomalies by taking the difference between negative years and positive years with the

sign of the composites so chosen that SST anomalies are positive in the SH. These composites are referred to as the "backward composites" because the composite begins in MAM+1 and we track the origin of the anomalies back to June-July-August of the previous year (JJA0). Figure 21 shows the results for the seasons JJA0, September-October-November (SON0), December-January-February (DJF+1), and March-April-May (MAM+1). Statistical significance at the 95% level, indicated by the shading, was computed by applying a two-sided Student's t-test. As can be seen, the SST dipole observed in MAM+1 (bottom panel) is clearly preceded by an SST anomaly localized in the southern subtropics at about $15°S$. This SST anomaly originates in JJA0, grows in magnitude and "tends to move" equatorward with time. In the following section, using a modeling approach, we show that this apparent "movement", or equatorward "propagation", is the result of thermodynamical damping of subtropical SSTs and the excitation of TAV in the deep tropics that maintains SST anomalies there. In DJF+1 a negative SST anomaly begins to develop in the TNA, which peaks in the following season. The tripole observed in the North Atlantic region suggests that the NAO is, at least partially, responsible for the SST anomaly in the TNA. Note that SST anomalies in the TSA are larger than in the TNA before MAM+1.

The fact that large SST anomalies in the TSA region precede a strong cross-equatorial SST gradient suggests that a linkage may exist between the SH winter atmospheric variability and the onset of the anomalous gradient. This points to a potentially important role of the SH atmospheric variability in TAV.

2. Surface circulation

To look at the surface circulation associated with the development of the gradient mode we constructed a "backward composite" based on the 925mb winds taken from

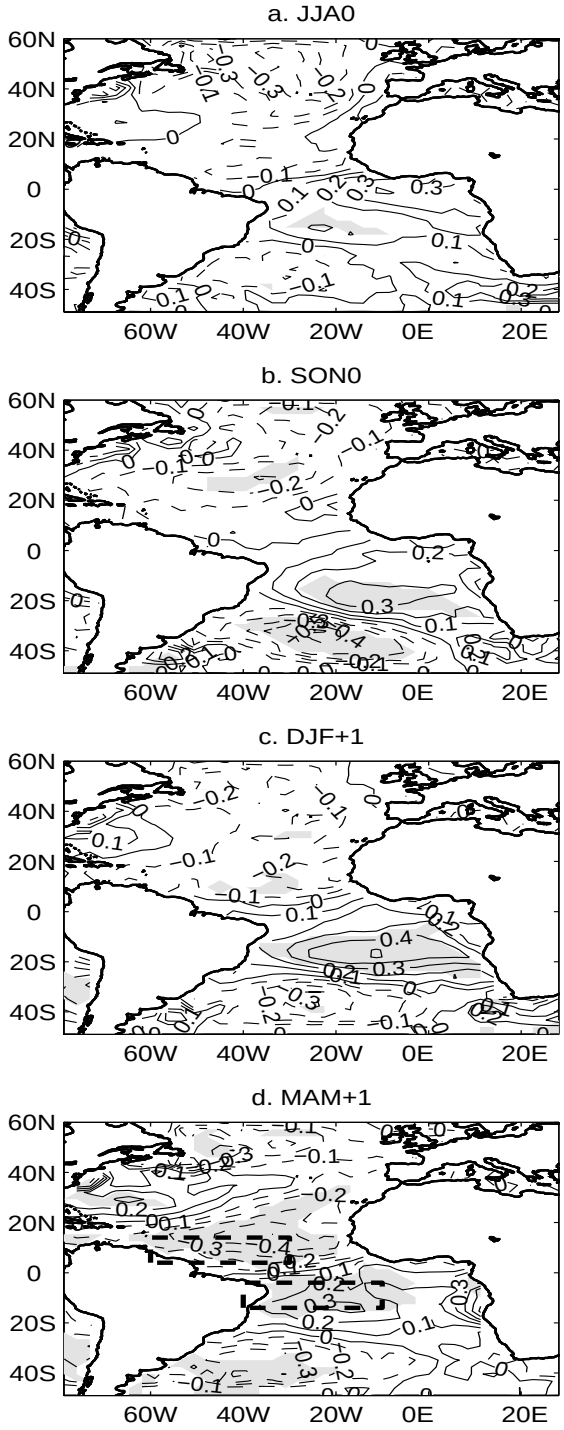

Fig. 21. Composites of observed SST, constructed as the difference between negative and positive years of the GI. (a) JJA0, (b) SON0, (c) DJF+1, and (d) MAM+1. Contour interval is 0.1K, and shading indicates statistical significance at 95% level. Boxes indicate the regions used to construct the GI.

NCEP-NCAR Reanalysis data set, for seasons JJA0 to MAM+1 using the same years as for the SST in Figure 21. Figure 22 shows that during SH winter and spring (JJA0 and SON0) there is a cyclonic circulation with westerly winds north of $\simeq 30°$S coexisting with warm SST anomalies below, consistent with the notion of atmosphere-to-ocean forcing through decreased heat fluxes. During NH winter the signature of NAO on surface winds is evident, while in the SH wind anomalies are no longer significant. In MAM+1, as expected, strong cross-equatorial winds accompany the cross-equatorial gradient of SST.

This result suggests that atmospheric variability may be responsible for the SST anomaly that develops in the TSA during JJA0 and SON0 and that precedes the dipole in MAM+1. It also points out the seasonality in the relevance of atmosphere forcing in TAV: during austral winter and spring the SH atmosphere forces the southern tropics, while during boreal winter the NH atmosphere forces the northern tropics. This is consistent with the notion that during these seasons the subtropical highs are closer to the equator and can influence the tropical regions. In this work we focus primarily on the IAV during the winter of each hemisphere, because it during this season that the IAV is most energetic and is more easily isolated from SST-forced signals. This is particularly true for observations due to the shortness of the record.

To further delineate the linkage between atmospheric variability in the SH and SST anomalies a number of important issues must be addressed: 1) Does the IAV during winter indeed force SST anomalies? If so, what is the evolution of these SST anomalies? Can an SST anomaly in the TSA alone excite TAV and create an SST dipole? 2) What are the relative contributions of the SH/NH winter atmospheric circulations to TAV?

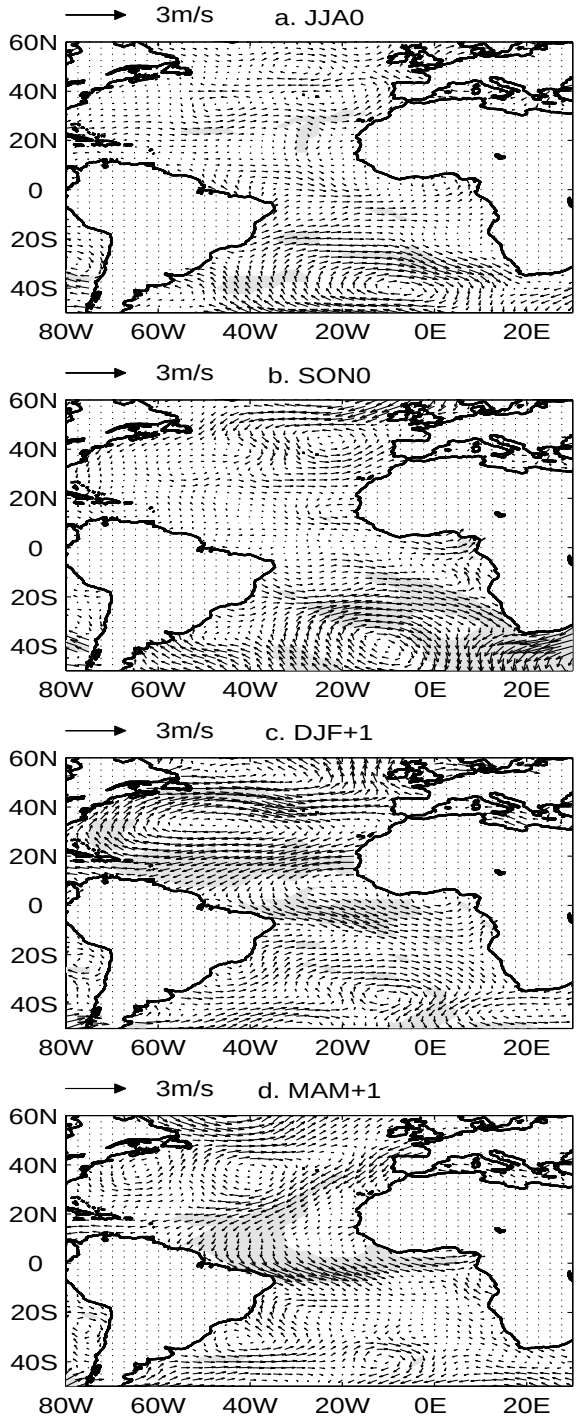

Fig. 22. Composite of observed 925 mb winds, constructed as the difference between negative and positive years of the GI. (a) JJA0, (b) SON0, (c) DJF+1, and (d) MAM+1. Shading indicates statistical significance at the 95% level.

C. Observed SH winter atmospheric circulation

In an attempt to look into the first issue, we calculated the EOFs of observed sea level pressure taken from NCEP-NCAR Reanalysis data set. The EOF analysis was performed in season JJA over the region ($0° - 50°$S, 70°W-30°E). Only the non-ENSO years were included in the EOF analysis to avoid contamination from ENSO events; thus, EOFs are likely to represent mainly the IAV during the austral winter. The leading EOF explains 40% of the total variance, and is shown in Figure 23a as a homogeneous regression map over a larger region. The pattern resembles a wave of wavenumber 3 spanning the middle latitudes of the SH. In the South Atlantic sector, the EOF represents a weakening/strengthening of the subtropical high. A weakened/strengthened subtropical high means decreased/increased southern trades (see Figure 23b), which may change the SST below through anomalous heat fluxes. As shown in Figure 23b by compositing the extreme (larger than one standard deviation) years based on the time series of the leading EOF of the sea level pressure, the wind anomalies are strong south of 10°S. The anomalous circulation patterns in Figures 22a and 23b are similar, both consisting in a cyclonic circulation with westerly winds north of 30°S. This finding lends support to the idea that the SST anomaly in the subtropical South Atlantic that precedes the gradient mode is generated by the IAV during austral winter.

As mentioned in the introduction, *Venegas et al.* [1997] found that the leading mode of coupled atmosphere-ocean variability in the South Atlantic basin consists of a weakened/strengthened subtropical anticyclone forcing the ocean. The associated time series has decadal time scales, and the corresponding oceanic response to the atmospheric forcing consists of an SST dipole with a node at about $25°S$. Results here suggest that the atmospheric counterpart of Venegas et al's coupled mode may

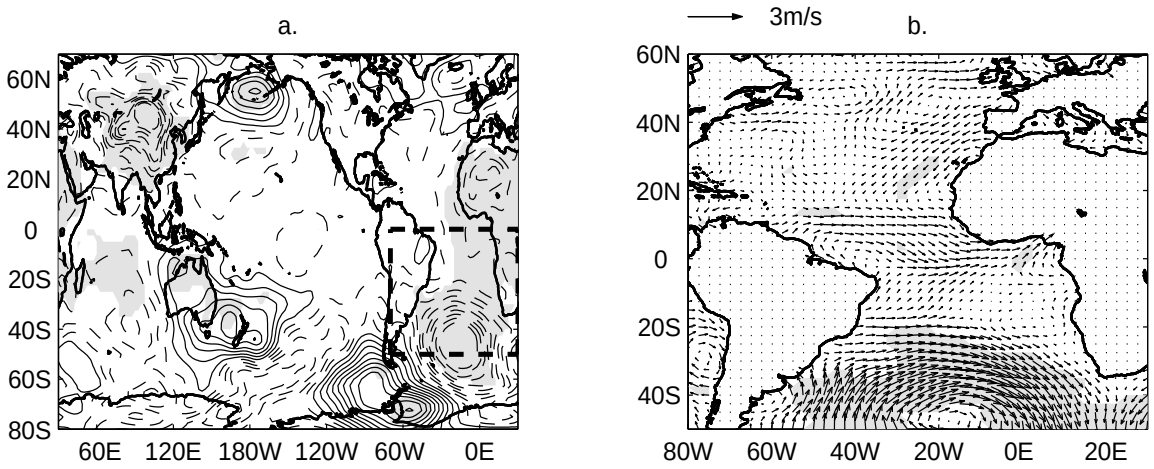

Fig. 23. (a) Spatial pattern of the leading mode of observed sea level pressure in JJA season, shown as a homogeneous regression map over a larger region. The dashed box marks the region in which the EOF analysis was performed. Contour interval is 20 Pa. (b) Composite of observed 925 mb winds constructed as the difference between positive and negative extreme years of the time series associated with the leading mode of observed sea level pressure.

be related to the pattern generated by IAV.

1. Evolution of SST anomalies forced by SH winter atmospheric circulation

We next study the evolution of SST anomalies created in the TSA by IAV during austral winter. To do so, we constructed composites for seasons JJA0, SON0, DJF+1 and MAM+1 taking as index the principal component of the first EOF of sea level pressure shown in Figure 23a. The extreme years identified and used in the composite were (1952, 1979, 1993) and (1960, 1962, 1963, 1964, 1986) when the sea level pressure was anomalously high and low respectively (years refer to MAM+1). We call this composite the "forward composite" in contrast to the backward composite shown in Figure 21, because it begins from austral winter (JJA0) and ends the following fall (MAM+1). Results are shown in Figure 24. Although anomalies are generally weaker

in the forward composite, the shape and evolution of SST anomalies in the SH are very similar to the ones in Figure 21. Figure 24 reveals that the maximum SST anomaly occurs during SON0, after which it weakens in the subtropics (presumably by heat flux damping), whereas in the deep tropics SST anomalies tend to persist longer (although they are just significant at 95% level). In the following boreal spring, a dipole is generated with weak anomalies in the northern tropics. Statistically significant low-level northerly cross-equatorial winds accompany the SST gradient during this season (not shown), indicating that even weak SST gradients can generate an atmospheric response in the deep tropics (as in *Chiang et al.* [2002]).

The tripole of SST anomalies in the NH is weaker than in Figure 21. According to the classification of *Czaja et al.* [2002], among the eight extreme years used in the composite, only one coincides with a strong NAO year that tends to generate in the TNA SST anomalies of opposite sign from those already existent in the TSA. Thus, it is unlikely that the NAO is completely responsible for the SST dipole. These results suggest that an SST anomaly created during austral winter in the southern subtropics may be able, by itself, to induce a dipole in the following MAM season.

A particularly important feature that is evident from the composites is that SST anomalies tend to persist for a long time in the region (5°-20°S) from the coast of Brazil to 10°W. To better quantify this assertion we calculated the decorrelation time scale of SST anomalies as given by the characteristic time scale of a first order autoregressive process fitted at each grid point. We found that in this region the decorrelation time scale is from 6 to 9 months. One possible reason for the long persistence is that the ocean mixed layer is relatively deep for a tropical mixed layer, having an annual mean of about 40 meters.

The composite analyses presented in this section were based on a very small sample of years because of the shortness of the observational record. Therefore, sta-

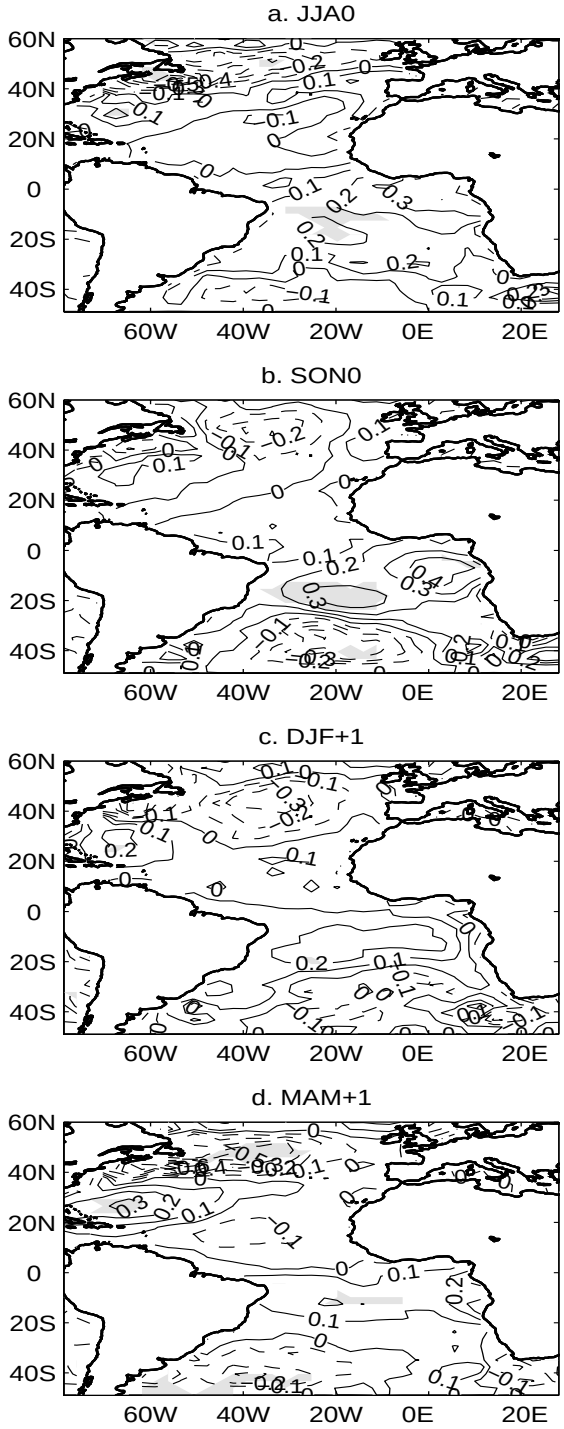

Fig. 24. Forward composite of SST for extreme years of the leading mode of observed sea level pressure in JJA. (a) JJA0, (b) SON0, (c) DJF+1, and (d) MAM+1.

tistical robustness becomes an issue, making it difficult to draw a definite conclusion. Moreover, it is impossible to clearly isolate the SH influence from the NH based on such a small sample size, and the "forward composite" is likely to include the NAO influence.

To further look into these issues, we turn to AGCM simulations. Since we are looking for the response in the tropical Atlantic to forcing due to IAV, a large enough ensemble of AGCM simulations should allow for a clean separation of the SH remote influence from the NH influence. In the following section, we present results based on an ensemble of runs using an AGCM coupled to a slab ocean. This coupled system allows thermodynamic air-sea interactions and thus is capable of presenting variability with the same characteristics as the gradient mode.

D. Analysis of simulations of an AGCM coupled to a slab ocean

1. Model description and experimental design

The AGCM used is the CCM3 model described in Chapter II. Here the CCM3 is coupled to a slab ocean model with annual mean mixed layer depth [*Levitus*, 1994]. The coupling is performed everywhere outside of the tropical Pacific (from 18°S to 18°N) where observed SST [*Smith et al.*, 1996] is imposed as the boundary condition. Thus, the model generates its own SST in the tropical Atlantic by thermodynamic coupling between the atmosphere and the slab ocean. To assure the correct simulation of the annual cycle of SST the slab ocean uses a Q-flux correction that accounts for the missing climatological ocean dynamics in the model. We refer to this simulation as a POGA-ML experiment, following the terminology of *Lau and Nath* [2001]. It is worth pointing out that since the slab ocean does not contain any explicit dynamics, it is expected that it will tend to exaggerate the importance of feedbacks between SST

and surface heat fluxes. Thus, results presented here have to be further investigated using a more comprehensive ocean model.

We constructed a 12-member ensemble of POGA-ML runs spanning the period from January 1950 to December 1994. This large ensemble of integrations allows the application of the signal-to-noise optimization technique to separate forced (from the Pacific Ocean) and IAV in the winter season of both hemispheres.

2. Reproduction of observations

In this subsection we validate the model against observations by repeating on model output the analysis shown in Figure 21. We show that the simulation reproduces the evolution of observed anomalies, suggesting that the simple coupled model is a useful tool to study TAV.

As in the observational analysis, we first partitioned the model SST output into ENSO and non-ENSO years. Once the ENSO years are removed from the data set, we classify the non-ENSO years according to the modeled GI. It is important to keep in mind that whereas ENSO years are the same for observations and all ensemble members, positive/negative gradient years can vary from one ensemble member to another, and do not necessarily coincide with observed positive/negative years. This is because TAV can be excited by IAV, and IAV is chaotic in nature. This means that although the statistics of IAV is the same in all ensemble members, the actual realizations differ from one run to another due to different initial conditions in each run.

Figure 25 shows the composites constructed considering the positive and negative gradient years over all ensemble members. Clearly, the simulated behavior of SST and wind stress is very similar to observations. The SST anomaly in the TSA seems to originate in JJA0 due to the subtropical branch of an eddy-like circulation and

the maximum "moves" towards the equator with time. In DJF+1 the NAO influence manifests itself as an SST tripole in the North Atlantic, with its southernmost lobe generating negative SST anomalies in the TNA. In the SH, on the other hand, there are no significant circulation anomalies. In agreement with observations, the tropical SST gradient is maximum in MAM+1, and is accompanied by a large cross-equatorial surface flow. It is interesting to note that during SON0 the circulation anomalies occupy all the tropical region, and are likely to include both IAV during the season as well as a response of the atmosphere to the SST anomalies created the season before (see also next section). The model reproduced the seasonality of IAV forcing the TAV seen in observations: Tropical SSTs in the boreal spring are only influenced by SH extratropical atmospheric anomalies during the previous austral winter and spring.

The simulated results in Figure 25 are statistically more significant than the observed results in Figure 21 because the record is 12 times longer. We conclude that the model captures realistically the evolution of SST anomalies in the tropical Atlantic, and thus proceed to further analyze the model output to shed light on the issues raised in the previous section.

3. SH Winter IAV as an external forcing to TAV

In this section we corroborate the conjecture from observational analysis that the SH winter IAV can generate a subtropical SST anomaly that subsequently evolves into an SST gradient in the following boreal spring.

a. Separation of IAV from Pacific-forced variability

The internal variability of the SH atmosphere during local winter is isolated using the signal-to-noise optimization technique described in Appendix A. In the methodology, the time evolution of a simulated model variable is divided additively into two parts:

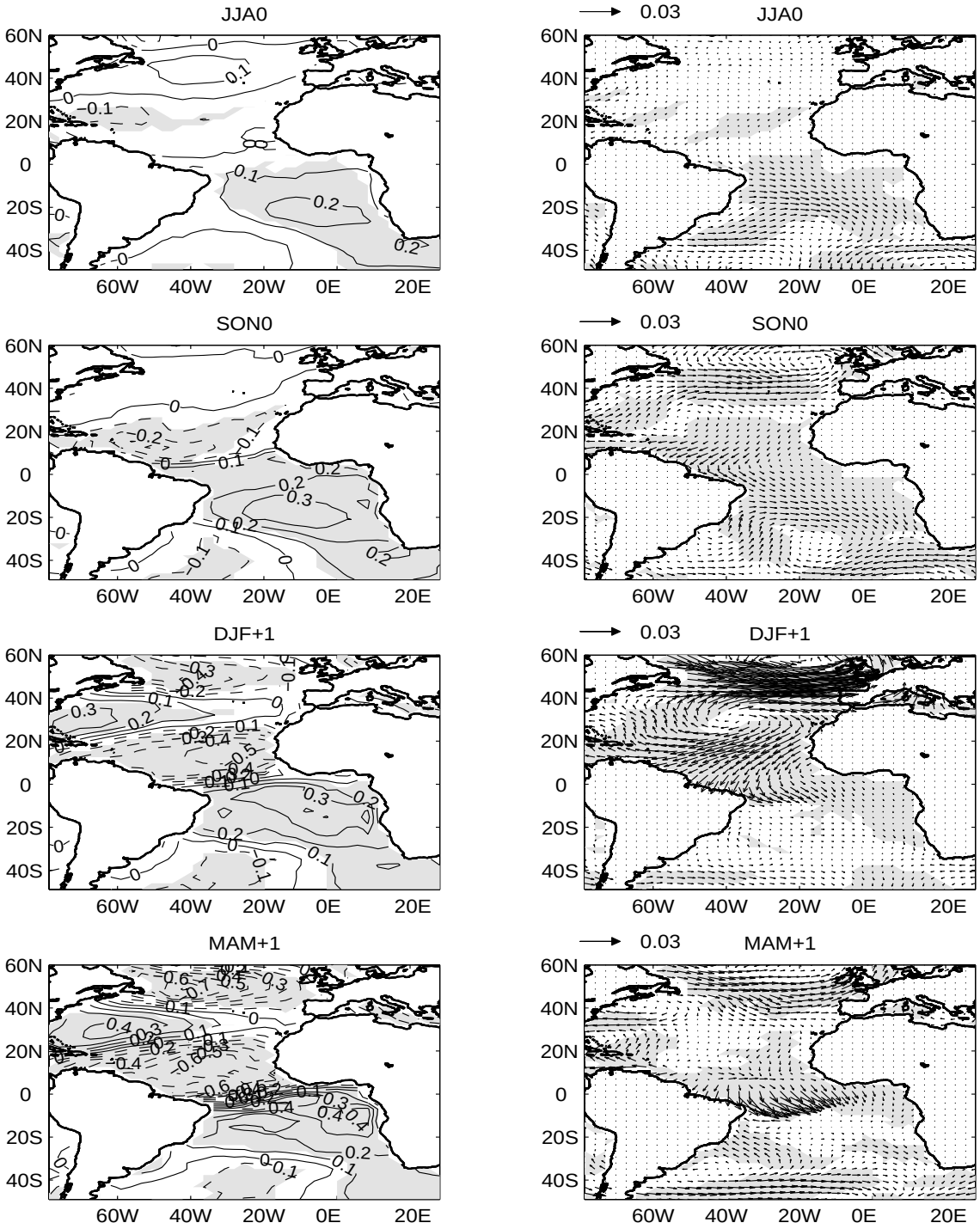

Fig. 25. Composites of model SST (left panels) and wind stress (right panels), according to simulated GI. Contour interval is 0.1 K for SST, and arrow scales are in Nm^{-2}. Shading indicates regions where either component of the wind stress is significant at 95% level.

an internal part due to intrinsic atmospheric dynamics (or IAV), and an external part due to imposed boundary conditions (forced variability). Here the goal is to separate the IAV from the ENSO-forced signal in the Atlantic basin. The IAV is constructed as the residuals of removing the forced signal (which is common to all ensemble members) from each ensemble member. In principle, the residuals may represent not only IAV, but also ocean-atmosphere coupling within the Atlantic basin. We assume that in winter the subtropical and extratropical atmosphere force the ocean but are not sensitive to the SST anomalies, and therefore the residuals are considered as only IAV. This is a good assumption because it is during winter that the IAV is largest. During the other seasons this assumption may not hold, and the residuals may include atmosphere-ocean coupling. An EOF analysis performed on the residuals provides the spatial structures and temporal evolution of the dominant modes of winter IAV in the model. Here we performed this analysis over the concatenated residuals of the surface pressure field from all the ensemble members over the region (50°-0°S, 70°W-30°E).

b. Forcing of the South Atlantic by IAV

Figure 26a shows the dominant mode of IAV in the South Atlantic (hereafter referred to as model-EOF1) as a homogeneous regression map over the globe. It explains 37% of total internal variability, and is very similar to the leading EOF calculated using the observed sea level pressure and shown in Figure 23a. This lends support to our previous assumption that the first observed EOF of sea level pressure represents IAV during the austral winter. The time series associated with model-EOF1 shows large within-ensemble variability, and no particular time scale (Figure 26b).

We form a "SH winter index" by concatenating the twelve PC time series associated with the model-EOF1 shown in Figure 26b, and use it to characterize IAV

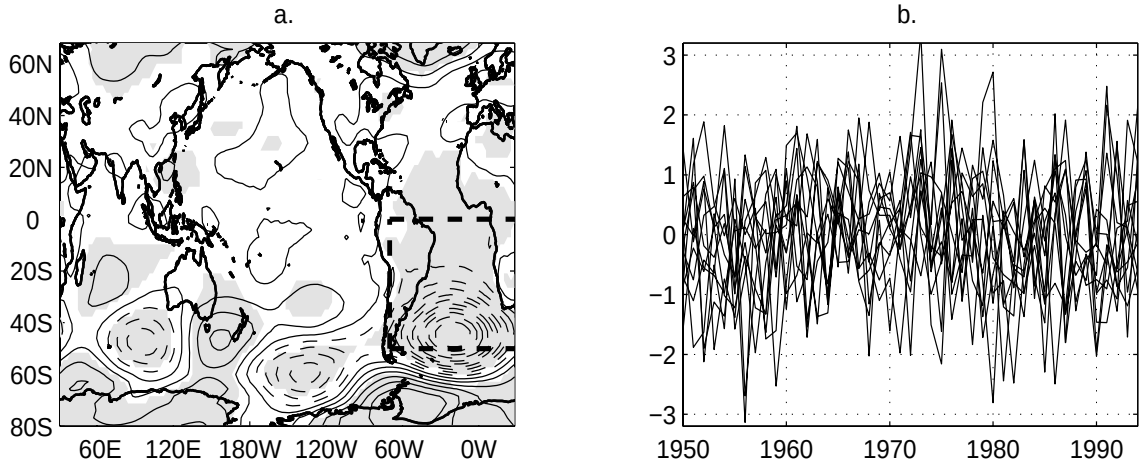

Fig. 26. (a) Spatial pattern, and (b) time series for the leading mode of IAV in the model during JJA. The dashed box marks the region in which the analysis was performed. Contour interval is 20 Pa, and shading indicates statistical significance at 95%.

during austral winter. Years with amplitude larger/smaller than $+\sigma/-\sigma$ (with σ the standard deviation of the SH winter index) are classified as positive/negative years. The composite of positive minus negative anomalies represents a situation in which the subtropical high is anomalously weak, allowing direct comparison with results of the previous sections.

To study the air-sea interaction in the tropical-subtropical Atlantic region we constructed composites for the SST, wind stress and net surface downward heat flux. To avoid contamination from the NH, we removed the extreme NAO years (when the NAO index is larger than one standard deviation, see below) that create SST anomalies in the TNA of opposite sign as those created in the TSA by the IAV during JJA. Composites are shown in Figure 27, and they depict the scenario explained below.

In JJA0, consistent with a weakened subtropical high, we observe a southeastward wind stress anomaly in the SH subtropics mainly south of 10°S. This wind

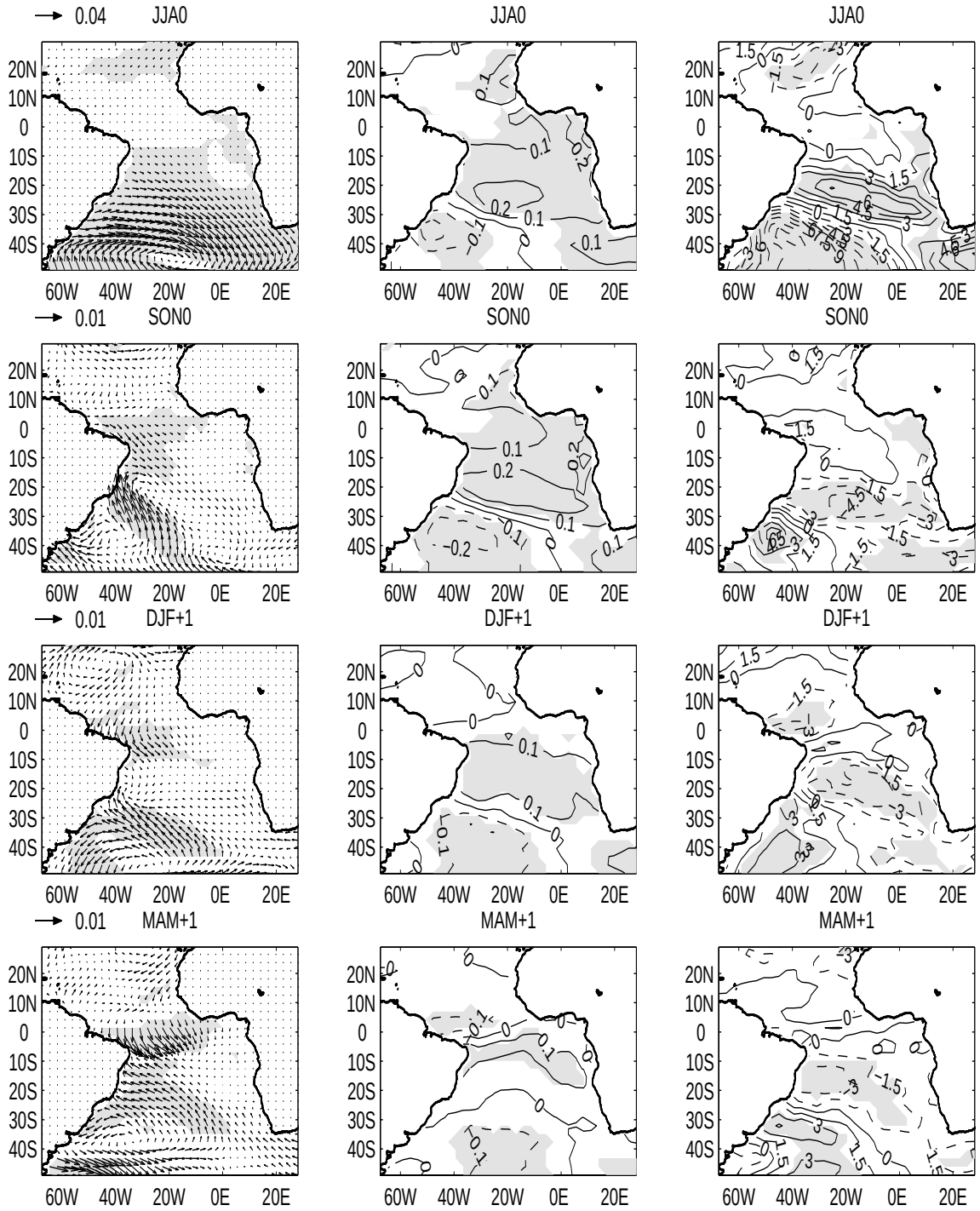

Fig. 27. Composite of wind stress (left panels), SST (middle panels) and net surface heat flux (right panels) constructed as the difference between positive and negative years of the SH winter index. In left panels arrow scales are in Nm^{-2}, and shading as in Figure 25.

anomaly induces a large net downward heat flux anomaly, which produces a warm SST anomaly north of 30°S. A cold SST anomaly south of 30°S is also created by the wind-induced heat fluxes. The positive SST anomaly has the same shape seen in Figures 21 and 24, and attains its maximum magnitude off the coast of Brazil at about 20°S in SON0. The net heat flux anomaly is largely due to the decrease in evaporative cooling, with relatively small contributions from sensible and radiative fluxes. The dominance of the latent heat fluxes holds for all seasons except MAM+1, when the shortwave fluxes are of comparable magnitude (see below). In SON0 southeastward cross-equatorial winds develop in the western side of the basin presumably as response to the positive SST south of the equator, and represent a decrease in the southern trades. At the same time the SST anomaly south of 20°S begins to weaken, due to heat loss to the atmosphere at a rate of about $12 W m^{-2} K^{-1}$. Equatorward of 15°S the heat flux anomaly is close to zero, except in the equatorial band at about 40°W where there is a small area of positive heat flux anomaly.

In DJF+1 northerly cross-equatorial winds in the western side of the basin have developed a curvature which is reminiscent of the climatological equatorward shift of the ITCZ. As the ITCZ moves closer to the equator, the northern branch of the trades is also affected by the existent cross-equatorial SST gradient, creating northwesterly wind anomalies in the deep tropics. In the southern tropics, the southern trades are still weakened by the SST gradient. As a result, heat fluxes of opposite sign develop across the equator cooling the SST to the north and sustaining the warming to the south through a positive air-sea feedback. Meanwhile, in the subtropics the SST anomaly has decreased substantially due to thermodynamical damping. In MAM+1 an SST dipole emerges, with statistically significant SST anomalies on both sides of the equator. SST anomalies are now concentrated in the deep tropics, and are accompanied by northerly cross-equatorial winds, as seen in Figures 21

and 25. There, the net surface heat flux is negligible because of a counterbalance effect between the latent heat flux and the shortwave radiation: Wind-induced latent heat fluxes tend to strengthen the SST anomalies through a positive feedback, while decreased (increased) insolation over warm (cold) waters opposes it (not shown). Insolation changes coincide with regions of anomalous precipitation. Hence, in the near-equatorial region, the shift of the ITCZ due to the anomalous SST gradient provides a negative feedback by preventing incoming solar radiation from reaching the surface.

The combination of subtropical damping and a positive air-sea feedback in the deep tropics results in the apparent "motion" of the SST anomaly towards the equator. Thus, the analysis supports the existence of a positive, large-scale feedback in the western deep tropical Atlantic basin, as found in previous works, e.g. [*Chang et al.*, 2000; *Chiang et al.*, 2002]. In JJA+1 net heat flux anomalies tend to damp SST anomalies everywhere, including the deep tropics.

The forward composite of Figure 27 presents smaller SST anomalies than the backward composite of Figure 25 (as also seen in observations). The main reasons are the absence of circulation anomalies in the SH during SON0 and of the NAO during boreal winter, and the enhanced air-sea coupling that associated SST anomalies would induce. We address the role of the NAO in the next section. Comparison of Figures 25 and 27 suggests that during austral spring both IAV and an atmospheric response to SST forcing play a role in the development of the gradient mode. Assuming that the IAV is much larger than the SST-forced part, we calculated the leading mode of IAV during spring in the SH. The spatial structure is very similar to that of the leading EOF in JJA. Then, to look at the role of the IAV during SON0 we constructed an analogous composite to Figure 27, but only considering the subset of years in which the leading mode of atmospheric circulation in SON0 is such that it

tends to reinforce the SST anomalies already created by the atmospheric circulation in JJA0. We found that the evolution of SST anomalies is dictated by the same processes described for Figure 27, but the resultant SST gradient in MAM+1 is stronger and occupies a larger area (not shown). Thus, this suggest that the main role of the SH winter IAV is to pre-condition the SSTs south of the equator for the development of a strong SST gradient in the following boreal winter and spring seasons. Results also show that austral winter IAV may be able, by itself, to excite TAV the following year: SST anomalies in tropical latitudes, mainly a consequence of evaporative heating anomalies associated with changes in wind speed, tend to persist until a favorable season for the excitation of TAV, and grow into a cross-equatorial dipole in boreal spring. Circulation anomalies during season SON0 may further enhance (weaken) the SST anomaly induced by IAV during winter, thus assisting (interfering) the development of a larger gradient in MAM+1.

4. NAO as an external forcing to TAV

To compare the SH influence on TAV with the NH influence, we repeated the same analysis to the data in the NH. We define the northern winter season as January-February-March (JFM), which coincides with the most active NAO season [*Marshall et al.*, 2001], and apply the same procedure of section 3c to surface pressure in the region defined by (70°W-30°E, 20°-70°N).

The leading mode of internal variability is shown as a homogeneous regression map over an extended domain, encompassing the Pacific basin. As expected, the dominant mode is an NAO-like circulation (Figure 28). It consists of a dipole in surface pressure, with one center of action west of Portugal, and the other one, of opposite sign, located north of Iceland. A secondary maximum in surface pressure is found in the North Pacific, in agreement with the literature [*Marshall et al.*, 2001;

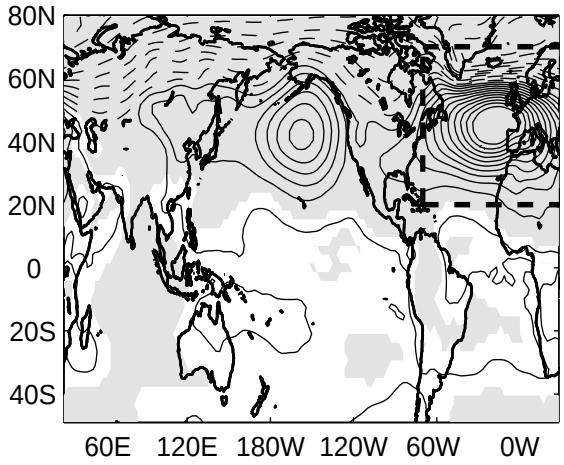

Fig. 28. Spatial pattern of the leading mode of IAV in the model during JFM season. The spatial pattern is shown as a homogeneous regression map over a larger region. EOF analysis was performed in the region marked by the dashed box. Contour interval is 20Pa, and shading indicates statistical significance at 95%.

Thompson and Wallace, 1998]. The time series associated with this pattern, which we will use as an index of NAO, shows large intra-ensemble variability and no preferred time scales.

Composites of SST and net heat flux anomalies were constructed using the NAO index in the same way as in the case of the SH. The only difference is that we shifted the calendar from DJF+1 to SON+1 to capture the evolution of SST anomalies generated by the NAO during boreal winter.

In agreement with previous studies, e.g. [*Marshall et al.*, 2001], the composite of SST anomalies shows the tripole characteristic of NAO forcing in the North Atlantic Ocean, reaching maximum amplitude in MAM+1 (left panels, Figure 29). In this season SST anomalies are mostly confined to the north of 10°N. The DJF+1 net heat flux composite reveals a net heat input into the ocean mixed layer with the same structure and sign as the composite of SST anomalies (right panels, Figure 29). In MAM+1 the net heat flux anomalies change sign, damping SST anomalies almost

everywhere. During the same season, in the northwestern tropics, between $0° - 20°$N, the sign of the heat flux anomaly tends to be the same as that of the SST anomaly (both negative), hinting at the existence of a positive feedback there. Both, the latent heat flux and solar radiation contribute to the cooling of the SST. As result, the SST anomaly appears to "move" equatorward, reaching the equator in JJA+1. In this season the wind-induced latent heat flux cooling in the northwestern tropics is almost balanced out by increased insolation. Hence, the net surface heat flux is close to zero, and the SST anomalies persist until SON+1. As in the previous section, and in agreement with previous studies [*Chang et al.*, 2000], the positive feedback is seen to occur only on the western side of the equatorial Atlantic basin.

There is a tendency for the TSA to show SST anomalies of sign opposite to that in the TNA, but they do not become significant. We conclude that the NAO can create large SST anomalies in the TNA, and in the northern deep tropics with the help of a positive feedback (thus creating a large SST gradient). The influence of the NAO on the TSA is, however, very weak and not consistent with the emergence of an SST dipole in the tropical Atlantic. These results agree with the diagnostic study of [*Czaja et al.*, 2002], where they find evidence, in observations, of a positive feedback within the northern deep tropics. They also note, however, that no SST anomaly develops south of the equator when regressing SST onto an index of the TNA in MAM.

E. Summary

The dominant mode of climate variability in the tropical Atlantic is characterized by an interplay between SST, winds and evaporation, with largest manifestation in boreal spring. This mode of variability has been shown to have interannual-to-decadal time

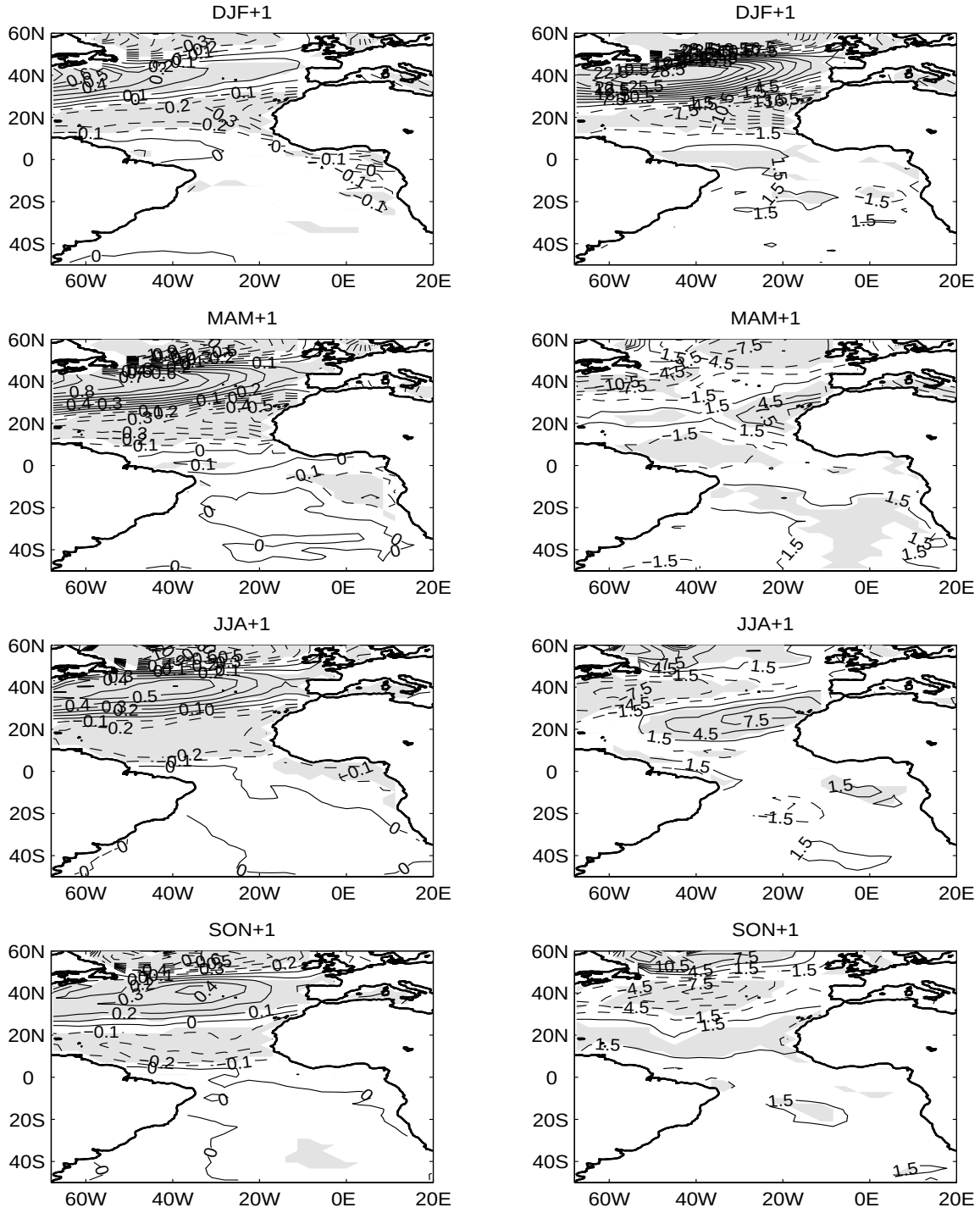

Fig. 29. Composite of SST (left panels) and net downward surface heat flux (right panels), constructed as the difference between positive and negative years of the NAO index.

scales, and is commonly thought to be externally excited by atmospheric anomalies acting on the TNA.

We studied, using both observations and model output, the evolution of SST anomalies in the Atlantic basin for those years during which the ENSO phenomenon is absent, but a significant cross-equatorial SST gradient develops in the boreal spring. A particular emphasis was placed on the role of the SH winter IAV in the development of a tropical SST gradient. We also contrasted the SH influence on TAV with the influence of the NAO using a large ensemble of POGA-ML runs. Ocean dynamics, such as currents and wave propagation, are not taken into account in these experiments. The working hypothesis is that ocean-atmosphere interaction in the tropical Atlantic primarily involves a thermodynamic coupling between SST and heat flux.

The results indicate that the SH winter IAV plays a pre-conditioning role in the onset of strong SST gradients in the boreal spring of the following year. The modeling study provides a plausible mechanism through which the SH winter IAV may excite TAV and lead to the development of the gradient mode. The scenario can be described as follows: in JJA0 a weakened South Atlantic subtropical high leads to weakened southeasterly trade winds, which, in turn, remove less heat from the ocean, thus generating a warm SST anomaly north of 25°S. This SST anomaly appears to have maximum amplitude around 20°S. In the subsequent seasons, the subtropical part of the SST anomaly is damped by anomalous latent heat fluxes, but not the tropical part. The SST anomaly equatorward of 10°S is created by a wind change in response to a cross-equatorial SST gradient, and maintained by a weak positive air-sea feedback. The expected interplay between SST, heat flux and winds characteristic of TAV creates a negative SST anomaly in the northern tropics and sustains the existence of the SST dipole through MAM+1. The thermodynamic feedback in the near-equatorial region is opposed by the negative feedback provided by anomalous

cloud cover due to the shift of the ITCZ toward anomalous warm waters. This result is consistent with the observational work of *Tanimoto and Xie* [2002]. In agreement with observations, the model further indicates the disappearance of the dipole by boreal summer, when the positive feedback ceases to exist.

In contrast, the NH winter IAV, as characterized by a NAO-like circulation, has a large impact on the TNA SSTs, in agreement with the literature. These SST anomalies are mainly confined north of 10°N in boreal spring. During the following seasons the SST anomalies move equatorward as a result of a positive air-sea feedback in the deep northern tropics. There is a tendency in the TSA to develop an SST anomaly of opposite sign during northern summer and fall, but it does not become statistically significant.

F. Discussion

In this chapter we investigated the influence of SH winter IAV on the origin and evolution of SST anomalies in the tropical Atlantic. As is the case for the NAO, we show that the SH winter IAV can possibly excite TAV and produce tropical anomalies during the following austral summer and fall seasons. The time lag of about 6 to 9 months appears to be related to the time scale of response of the mixed layer to atmospheric forcing, and to the time scale associated to the "movement" of the initially subtropical anomaly towards the deep tropics. However, model results suggest that there is an asymmetry in forcing the deep tropical SST anomalies from both hemispheres. While SST anomalies in the TSA affect TAV in the deep tropics and can produce SST anomalies of opposite sign in the TNA, the NH winter IAV does not seem to be able to generate an SST anomaly of opposite sign in the TSA. This asymmetry could be a consequence of the missing ocean dynamics in the slab ocean

used here, or, more fundamentally, of asymmetries in the geographical distribution of continents in the equatorial region. Note that the positive feedback in the TNA occurs in a longitudinal band which is occupied by land to the south of the equator (Figure 29), whereas the reverse is not true for the TSA.

The role of the thermodynamic air-sea coupling in the deep tropics seems to be that of maintaining and "moving" towards the equator the SST anomaly created in the subtropics. This mechanism could be fundamentally important for enhancing seasonal predictability in the deep tropics, which would allow prediction of SST anomalies, and thus of the ITCZ location, up to 9 months in advance. In the absence of this process the lifespan of SST anomalies would be much shorter, on the order of a season or less, given the shallow depth of the mixed layer in the deep tropics.

The TAV excited by the southern tropical SSTs leads to the generation of a dipole in MAM that is confined to the deep tropical region. Although SST anomalies are weak, they may still be relevant to ITCZ variability, because it is during that season that the ITCZ is closer to the equator and the associated convective activity is very sensitive to the SST within the 10°S-10°N band [*Chiang et al.*, 2002]. On the other hand, the NAO induces a large SST anomaly north of 10°N during that same season. Accordingly, a stronger SST gradient would be created (in MAM+1) during those years in which the NAO acts constructively to generate a larger dipole than the one that would be created in the absence of NH circulation anomalies (recall that IAV in the SH and NH winter are assumed to be independent). Not only would the SST anomaly in the TNA encompass a larger area, but the anomalies in the deep tropics would last longer because they can be sustained by a stronger coupling. A composite of the evolution of SST anomaly in such years suggests that this is in fact the case (Figure 30). In other years, however, the NH winter circulation anomalies may act in an opposite way, disrupting the generation of the SST gradient. In addition, the SST

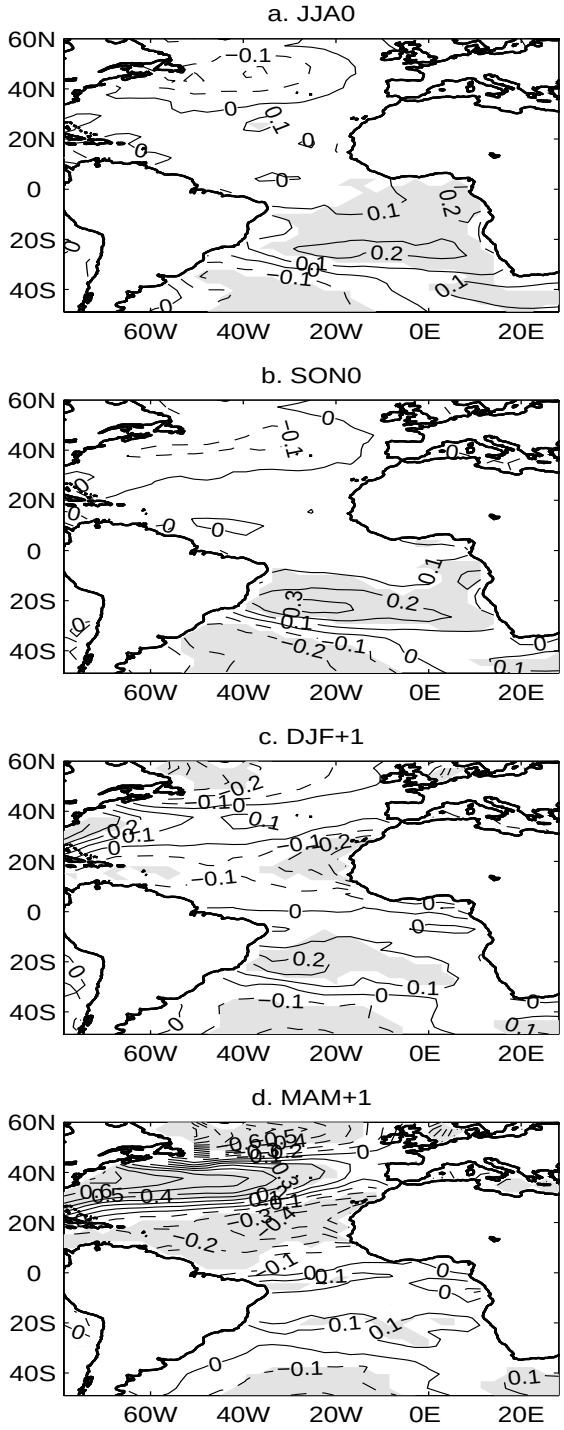

Fig. 30. Composite of SST, constructed considering only those years in which the NAO forces SST anomalies on TNA with opposite sign than those created in the TSA by the SH winter circulation in JJA0. (a) JJA0, (b) SON0, (c) DJF+1, and (d) MAM+1.

anomaly created by the SH IAV during austral winter in the TSA may be further reinforced by circulation anomalies during the next spring, creating a larger anomaly that will help the development of a larger dipole.

We want to stress, however, that results support the view that the gradient mode is not just the sum of SST anomalies created independently at both sides of the equator by IAV and the ocean responding passively. Atmosphere-ocean thermodynamic coupling in the deep tropics plays a fundamental role in the development of the mode. Based on these findings, we propose that to understand the TAV it is necessary to consider not only the remote influence of ENSO and the NAO, but also the atmospheric circulation in SH. We anticipate that the consideration of the SH winter atmospheric circulation as a pre-conditioning process for the state of the tropical Atlantic in the following seasons will aid in predicting and understanding TAV.

CHAPTER IV

PREDICTION OF TROPICAL ATLANTIC SST USING AN AGCM COUPLED TO A SLAB OCEAN

A. Introduction

Several studies have shown that AGCMs have high skills for seasonal climate prediction in the tropical Atlantic, provided the SSTs are known in advance. One particular region in which AGCMs have shown large potential predictability is the Northeastern region of Brazil during the rainy season (see Figure 42 below). However, current seasonal predictions of tropical Atlantic SSTs are based on statistical approaches and the skill of these forecasts is usually not better than the prediction given by persistence forecasts. One of the reasons for the low skills is the poor understanding of the complex underlying dynamics in TAV. The majority of current-generation of fully coupled general circulation models (GCMs) contain large systematic biases in the climatic mean state of the Atlantic region, and have not been able to realistically simulate TAV, particularly the covarying pattern of cross-equatorial SSTs and overlying atmospheric circulation characteristic of the gradient mode (see Figure 20). To bypass the large systematic errors encountered by fully coupled GCMs, we explore an alternative way for prediction of SSTs and climate in the tropical Atlantic region using an AGCM coupled to a slab ocean model.

In the previous chapter we demonstrated the relevance of thermodynamic air-sea coupling in the evolution of SSTs within the tropical Atlantic basin. From the results of the previous chapter, it is likely that this positive feedback will increase the persistence of SST anomalies (thus enhancing the predictability) by opposing other negative feedbacks.

In addition to the local thermodynamic feedback, there is at least one more process that can enhance the predictability of tropical Atlantic SSTs: the remote ENSO influence. As mentioned in Chapter III, the atmospheric circulation anomalies associated with ENSO are known to generate SST anomalies in the TNA with maximum amplitude during boreal spring through changes in the surface heat flux. TNA SST anomalies lag the Pacific SSTs by about a season. The delay is given by the time that it takes the atmosphere to respond to equatorial Pacific SST anomalies, and the tropical Atlantic Ocean response to these circulation anomalies. Thus, knowledge of the SST conditions in the Pacific during the previous December is useful for predicting TNA SST anomalies during the boreal spring following an ENSO event. Moreover, since ENSO itself has been shown to be predictable a few seasons in advance, this predictability translates to the SST predictability in the Atlantic basin.

Based on this reasoning *Chang et al.* [2003a] recently carried out sets of prediction experiments using the CCM3 model coupled to a slab ocean. This coupled model can be viewed as the simplest tier-one global dynamical seasonal prediction system. Using global observed initial conditions in December, *Chang et al.* [2003a] run the coupled model in prediction mode until mid-September of the following year. A 10-member ensemble of prediction runs was constructed for the period from 1981 to 1996. Their results show that the predicted SSTs in the Caribbean and TNA regions have correlation skills higher than 0.5 for lead time of up to six months. Since the SST persistence is short in these regions (due to a shallow mixed layer), this skill is attributed to the remote influence of ENSO and the local feedbacks. On the other hand, the model shows much reduced skill in the equatorial region where the correlation skill drops to a non-significant value after a lead time of two months. Low skills were also found in the Atlantic cold tongue region. The reason for the model's low skills in these regions is hypothesized to be due to the absence of ocean dynamics

in the slab ocean. These results are confirmed by an extended prediction experiment from 1959 to 2000.

The goal of this chapter is to test the hypothesis of the importance of ocean dynamics in the predictability of TAV. A second objective is to improve the prediction of SSTs by including the relevant ocean processes to the CCM3 coupled to the slab ocean. In the following section we describe the prediction experiments. In section C we present a way to statistically correct the slab ocean so that it includes a parameterization of the ocean dynamics relevant to TAV. Prediction experiments with the corrected coupled model are shown in section D, and are compared to prediction experiments without the correction, focusing on two variables: SST and precipitation. Section E analyzes the patterns and temporal evolution of the leading modes of SST variability in the different setups of the model and compares them to observed ones. In section F we summarize our findings, and in the last section we discuss the results.

B. Model and data sets

The CCM3 is coupled to a slab ocean as in Chapter III (hereafter CCM3-ML). Here, however, the CCM3-ML is run in prediction mode, that is, it is initialized with observed initial conditions and then let run freely for 9 months. Note that the slab ocean only needs to be initialized with SSTs, and does not need any subsurface ocean data.

Four different prediction experiments were carried out using the CCM3-ML.

- Prediction with Global Initial Conditions (PGIC): The CCM3-ML was initialized with global observed December SSTs during 1959 to 2000.

- Prediction with Atlantic Initial Conditions (PAIC): The CCM3-ML was initialized with observed SSTs only in the Atlantic basin within 30°S and 60°N.

Outside the basin December climatological SST was used as initial condition. The prediction was performed from 1959 to 2000.

- Corrected Prediction with Global Initial Conditions (CPGIC): Analogous to GPIC but the slab ocean included a correction designed to take into account some of the effects of linear ocean dynamics on SST evolution. The prediction was performed starting from December of 1981 to 2000.

- Corrected Prediction with Atlantic Initial Conditions (CPAIC): Analogous to PAIC but the slab ocean included a correction designed to take into account some of the effects of linear ocean dynamics on SST evolution. The prediction was performed starting from December of 1981 to 2000.

Each prediction experiment consists of 10 ensemble members. Each ensemble member was initialized with a different atmospheric initial condition, which corresponds to actual December days taken from NCEP-NCAR Reanalysis data set around December 15th. The slab ocean was initialized with the observed SST averaged over the week of December 15th. All prediction experiments were run from December 15th to September 15th. We analyzed the experiments from January to August with a particular attention to the boreal spring that is the peak season of the gradient mode. In what follows we will refer PGIC and PAIC to as the non-corrected experiments. The corrected prediction experiments (CPGIC and CPAIC) were conducted only for the period 1981 to 2000 because of the sparsity of the data in the SH in the earlier period (before the advent of satellite-derived SST), and because of our focus on the equatorial Atlantic where the ocean dynamics is believed to be most active.

We validated predictions against observations by focusing on two very important climatic variables: SST and precipitation. We use the reconstructed data set of *Smith et al.* [1996] for SST, and the Xie-Arkin data set for precipitation. Surface wind stress

and 925 mb winds taken from the NCEP-NCAR Reanalysis data set were also used in this study. All data sets were projected onto a T42 grid, which has a horizontal resolution of roughly 2.8° x 2.8°.

C. Statistical correction of the slab ocean

1. Methodology

The approach consists of introducing a new term to the SST equation of the slab ocean that parameterizes some of the effects of linear ocean dynamics on the SST evolution. The derivation is summarized as follows.

In a slab ocean the evolution of SST is completely determined by the surface heat fluxes. After removing the annual cycle we can write $\frac{\partial T}{\partial t} = Q$, where T is the sea surface temperature anomaly, t denotes time, and Q is the net surface heat flux anomaly into the ocean divided by the heat capacity of the mixed layer. We assume that Q can be divided additively into two parts: one that is related to the surface temperature ($Q_S(T)$), and a second part that is independent of the temperature, which we will consider as noise (Q_N) (see Appendix B). Thus, the SST equation of the slab ocean reads

$$\frac{\partial T}{\partial t} = Q_S(T) + Q_N, \tag{4.1}$$

where variables denote ensemble mean quantities of a non-corrected prediction (PAIC or PGIC). We also assume that the observed SST anomaly obeys a similar equation, i.e.,

$$\frac{\partial \hat{T}}{\partial t} = \hat{Q}_S(\hat{T}) + \hat{Q}_N, \tag{4.2}$$

where the "hat" denotes observed quantities. Moreover, we assume that the heat flux

anomaly is linearly related to the temperature anomaly

$$Q_S(T) = AT, \quad \hat{Q}_S(\hat{T}) = \hat{A}\hat{T}, \tag{4.3}$$

where A and $\hat{A}$ are the linear operators (matrices) in the model and in the observation, respectively. These two operators are of course different because $\hat{A}$ includes not only ocean-atmosphere feedbacks, but also a contribution from ocean dynamics (see Appendix B). Our goal is to derive a linear operator B, such that $A+B$ approximates $\hat{A}$ as close as possible. After the operator B is determined, we can incorporate it into the equation of the slab ocean. The new term BT will represent an anomalous ocean heat transport.

To find B we proceed as follows: Taking the difference between equations (4.1) and (4.2), and rearranging the terms, we get an equation for the prediction error $\epsilon = \hat{T} - T$,

$$\frac{\partial \epsilon}{\partial t} = \hat{A}\epsilon + BT + \zeta, \tag{4.4}$$

where $\zeta = \hat{Q}_N - Q_N$. Since the initial prediction error is zero ($\epsilon(0) = 0$), evaluating equation (4.4) at $t = 0$ leads to

$$\left.\frac{\partial \epsilon}{\partial t}\right|_0 = BT(0) + \zeta(0). \tag{4.5}$$

Equation (4.5) states that the tendency of the prediction error at the initial time is linearly related to the initial temperature, and the operator that links the two quantities is the undetermined linear ocean dynamics. In reality, B represents not only the missing ocean dynamics, but also systematic errors in the atmospheric fluxes of the model. We assume that the latter is smaller than the former, so that B represents, to a large extent, the missing ocean dynamics. Integrating equation (4.4)

between zero and a small lead time τ ($\tau \rightarrow 0$) gives

$$\epsilon(\tau) \simeq \tau B T(0) + \int_0^\tau \zeta(t) dt. \tag{4.6}$$

Since by definition the noise part of the heat flux does not covary with the temperature, B can be calculated as the coefficient matrix of a multivariate linear regression,

$$B = \frac{1}{\tau} < \epsilon(\tau) T(0)^t >< T(0) T(0)^t >^{-1}, \tag{4.7}$$

where the brackets denote a time average. Equation (4.7) is formally valid only for small lead time prediction τ, and the inclusion of B in the equation of the slab ocean tends to correct for the initial tendency errors of the model. In our case, the minimum value of τ we can use is one month, because we use monthly data. Once B is determined, we incorporate it into the model as a linear correction. Thus, in a linear framework the SST equation reads,

$$\frac{\partial T}{\partial t} = AT + BT + Q_N \simeq \hat{A}T + Q_N. \tag{4.8}$$

The corrected slab ocean is no longer driven by atmospheric heat fluxes only. Changes in temperature can occur due to the action of matrix B on SST anomalies. Since B is generally non-diagonal, it connects different grid points within the corrected region. Therefore, changes of SST in one location may depend on SST anomalies in other locations. This property is essential to represent dynamical ocean processes, which can affect remote areas through advection or wave propagation. It is worth noting that the evolution of grid points outside the corrected area may also be indirectly influenced by B. Since the evolution of grid points within the corrected region is different in corrected and non-corrected experiments (due to BT), these changes may translate to other regions through, for example, heat fluxes due to wind

anomalies responding to an SST gradient. Thus, the evolution of SSTs in the Atlantic basin in corrected and non-corrected experiments may be different.

In principle this methodology can be applied globally. Since our focus is in the tropical Atlantic, we consider a relatively small ocean region defined by (50°W-20°E,20°S-5°N). This area encompasses the equatorial Atlantic as well as the Atlantic cold tongue region, and thus, it is a region where ocean dynamics is likely to play an important role, e.g., *Carton and Huang* [1994]. We hereafter refer this region to as the equatorial-tropical South Atlantic (ETSA).

2. Correction matrix B for the ETSA

The methodology to calculate B involves finding the inverse of the December SST covariance matrix (equation (4.7)), which in our case is singular. A way to solve this problem is to work in a reduced state space using EOFs as basis functions. Here we used EOFs of December SST as the basis. We first calculated the EOFs, and then projected $T(0)$ and $\epsilon(\tau)$ onto them, so that B can be determined in the EOF space. In general, B can depend on two parameters: one is the EOF truncation that determines the dimension of the EOF space where B is calculated, and the other is the lead time τ. As noted in section C.1, τ should be small for equation (4.7) to be valid. In practice, however, we allow it to vary from 1 to 5 months to find the best correction B. We show that the best correction B is found for the smallest possible τ in the available data, that is, for $\tau = 1$ month.

We applied the technique to the set of prediction experiments initialized with observed SSTs in the Atlantic basin only (PAIC). This is to avoid possible contamination from the remote influence of Pacific SST onto the ETSA. The Pacific SSTs may generate circulation anomalies that create a heat flux signal in the ETSA region. If this is the case, the total heat flux signal would depend not only on the local SSTs,

but also on remote SSTs, thus compromising the assumption stated in equation (4.3). Results show, however, that the characteristics of the correction B are very similar regardless of the choice of the non-corrected prediction set.

We now describe the criteria used to find the best correction B in the parameter space of EOF truncation and lag time τ. Assuming the evolution of the SST obeys equation (4.8), the SST at time t, $T(t)$, can be predicted from the initial condition $T(0)$ using the matrices A and B as [*Penland and Sardesmukh*, 1995]

$$T(t) = e^{(A+B)t}T(0). \tag{4.9}$$

The matrix A represents the linear relationship between the SST and heat fluxes in the absence of ocean dynamics. It can be calculated for the CCM3-ML following a Linear Inverse Modeling approach outlined in *Penland and Sardesmukh* [1995]. That is,

$$A = \frac{1}{l} * log(C_l * C_0^{-1}), \tag{4.10}$$

where C_0 is the covariance matrix of December SST, and C_l is the lag covariance matrix between December SST and SST at lag=l. In this study we used a control run to calculate matrix A. In the control run the CCM3-ML is integrated for 100 years, which provides a reliable independent data base to estimating A. Once A is calculated, we calculated B in the parameter space spanned by τ and the EOF truncation number. The predicted SST for January to August using equation (4.9) was then compared to the observed SST. We choose matrix B such that the prediction is the best according to the following two measures of prediction skill: the normalized error variance of predicted SST, and the correlation between prediction and observations during April-May-June. These skill measures are calculated over the entire corrected (ETSA) region. This criteria leads to the following choice of parameters: an EOF truncation

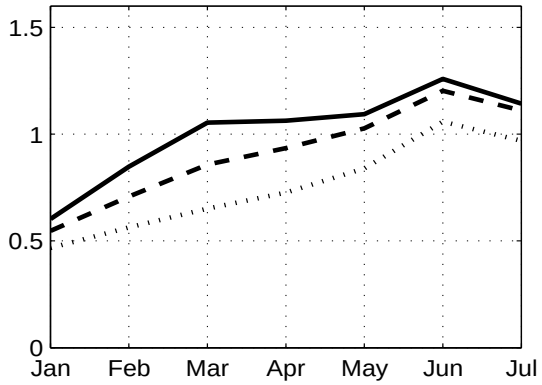

Fig. 31. Normalized error variance of predicted SST for CCM3-ML (solid line), linearized model (dashed line), and linearized corrected model (dotted line). The horizontal axis indicates lead time in months.

number of four (which explain 82% of the total variance), and a lead time τ of one month. The "a posteriori" result that the best B is found for the smallest possible value of τ is encouraging because, as said above, equation (4.7) was derived in the limit of very small τ.

Figure 31 shows the normalized error variance of predicted SST for the CCM3-ML, the linear model (equation (4.9) without B), and the corrected linear model (equation (4.9) with B). Clearly, the normalized error variance is smallest in the latter case. The correlation between the observed and predicted SST averaged over the corrected region during April-May-June is also consistent with this finding. It shows a correlation skill of $r = 0.31$ for the linear model ($B = 0$), and of $r = 0.51$ for the corrected linear model. Only the latter correlation skill is significant at the 95% level.

Results of Figure 31 were found using all the years from the period 1959-2000. We repeated the same analysis using a jackknifing procedure, where estimates of the correction matrix B were calculated leaving out the years for validation. The normalized error variances of predicted SST are, in this case, very similar to those

shown in Figure 31. Moreover, the correlation skill did not change significantly. The leading eigenmodes of B also have similar spatial and temporal characteristics with and without jackknifing (not shown). Furthermore, as noted before, results are not sensitive to the prediction set (PAIC or PGIC) used to calculate B. Therefore, we conclude that the characteristics of matrix B are robust, and we will use the correction B calculated using all available years as the linear correction to include the missing dynamics in the slab ocean.

We would like to stress that since the best correction matrix B is calculated using the prediction error at lead time $\tau = 1$, only the predicted January SST from PAIC is used. Moreover, the correction only accounts for the prediction error that is linearly related to the SST anomaly. Thus, the prediction experiments with the corrected slab ocean (CPAIC and CPGIC) are not simply hindcast experiments.

D. Dynamical predictions

To detect the coupled ocean-atmosphere signal, and therefore the predictable part of the dynamics, we calculated the ensemble mean of each experiment. The ensemble mean is considered the best climate prediction because it filters out the noise that is always present in the system. In the following we analyze the ensemble means of the prediction experiment unless otherwise noted.

1. Prediction of SST

a. Non-corrected prediction experiments

In this section we summarize the results of PAIC and PGIC experiments performed with the CCM3-ML during the period 1981 to 2000. Figures 32 and 33 show the correlation maps of PAIC and PGIC, respectively, from January to August in the

tropical Atlantic. Figure 34 shows the correlation map for the persistence forecast, which is taken as the reference forecast during the whole study.

During January and February PAIC and PGIC show very similar skills. Off equatorial regions are predicted well above the 95% level of statistical significance, but in the equatorial region the skill of the predictions is already below that level in February. The skill in the TNA region is higher than that of the persistence forecast, while in the ETSA the skill is comparable.

During March-April-May (MAM) the PGIC and PAIC perform much better than the persistence forecast in the TNA. The fact that PAIC shows higher skill than persistence indicates the importance of local thermodynamic air-sea feedback in the dynamics of the TAV. Note that skills are generally larger in the western side of the TNA where the feedback is believed to be operating. Also, the PGIC shows larger skill than the PAIC in the TNA demonstrating that remote influences from the Pacific Ocean are very important for the evolution of the region, in agreement with previous works [*Enfield and Mayer*, 1997]. In the equatorial and cold tongue regions, however, persistence is a better forecast model. These results are consistent with those of *Chang et al.* [2003a]. However, their experiment with Atlantic-only initial conditions presents higher skill in the deep tropical northern region. This difference may be related to the fact that we used weekly SST to initialize the experiment, while they used December monthly mean SST.

During June-July-August the PGIC and PAIC still show large skill in the TNA of comparable magnitude, while the skill of the persistence forecast is negligible. In the ETSA region the PGIC shows a skill comparable to persistence, but both are low. The PAIC shows almost no skill in the ETSA.

These findings indicate that SST predictability in the TNA has two sources, one due to local thermodynamic air-sea feedback, and the other due to remote influences

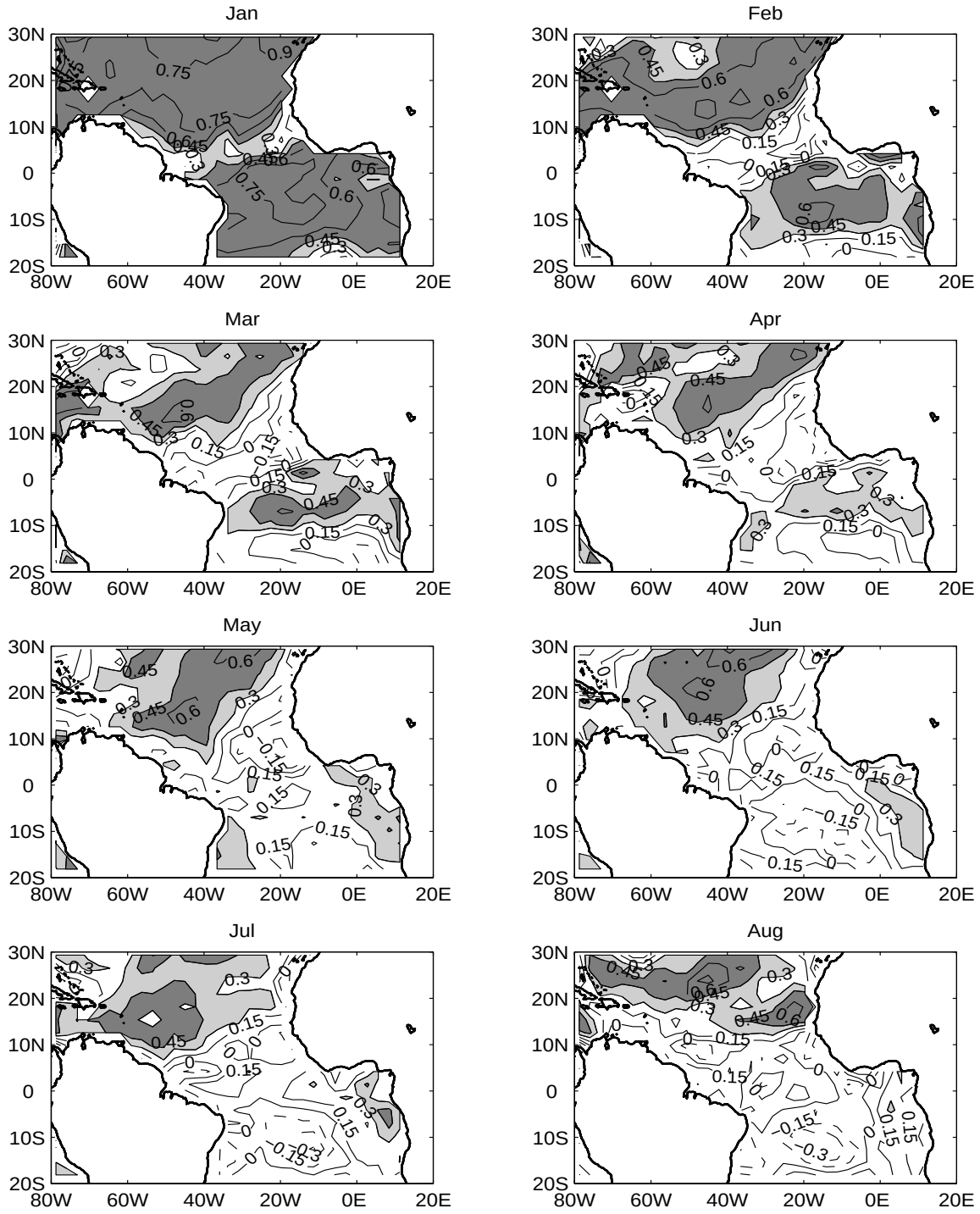

Fig. 32. Correlation between SST predicted by PAIC experiment and observed SST for different months. Correlations larger than 0.3 are in light shading, and correlations larger than 0.45 (95% significance level) are in dark shading.

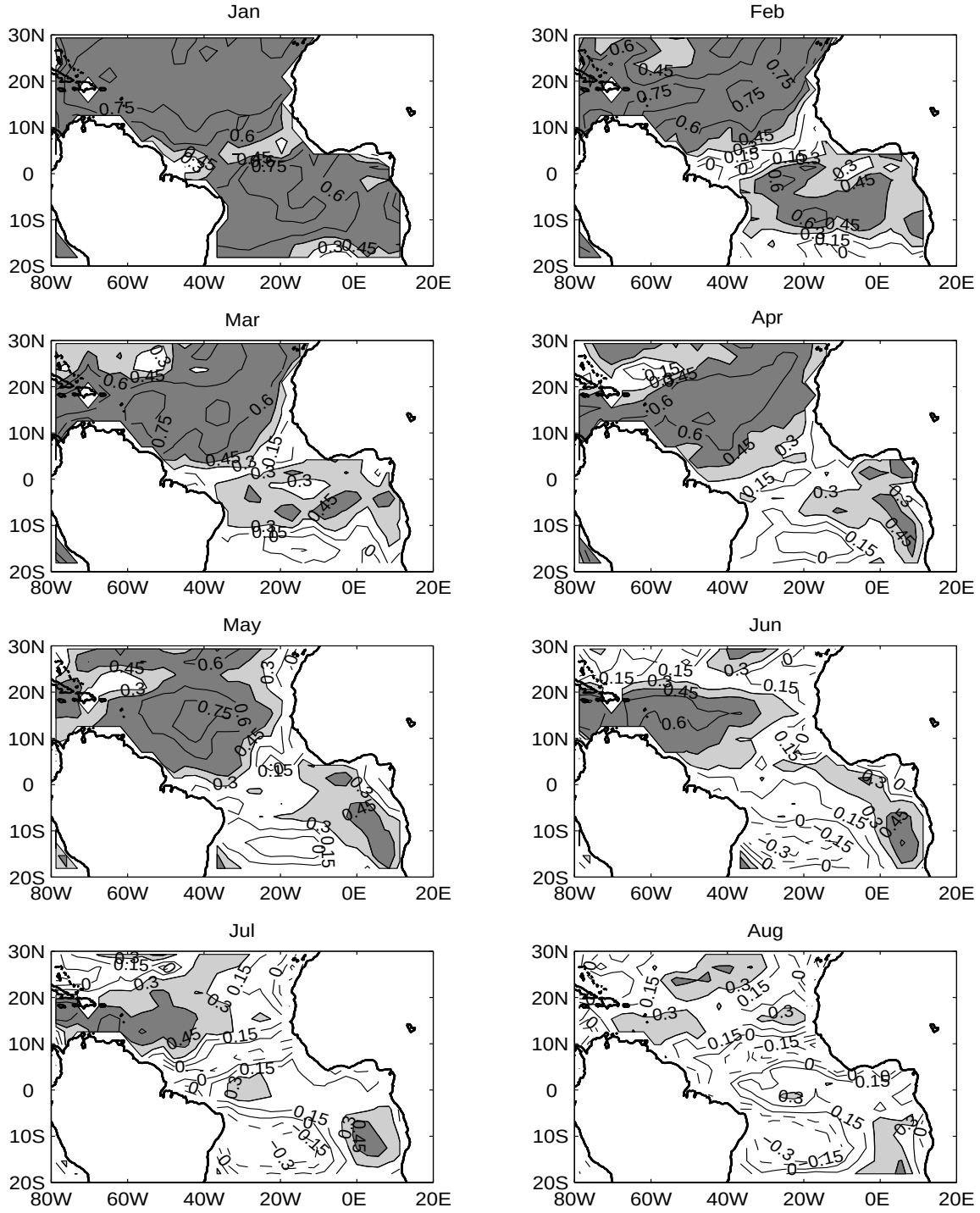

Fig. 33. Correlation between SST predicted by PGIC experiment and observed SST for different months. Shading as in Figure 32.

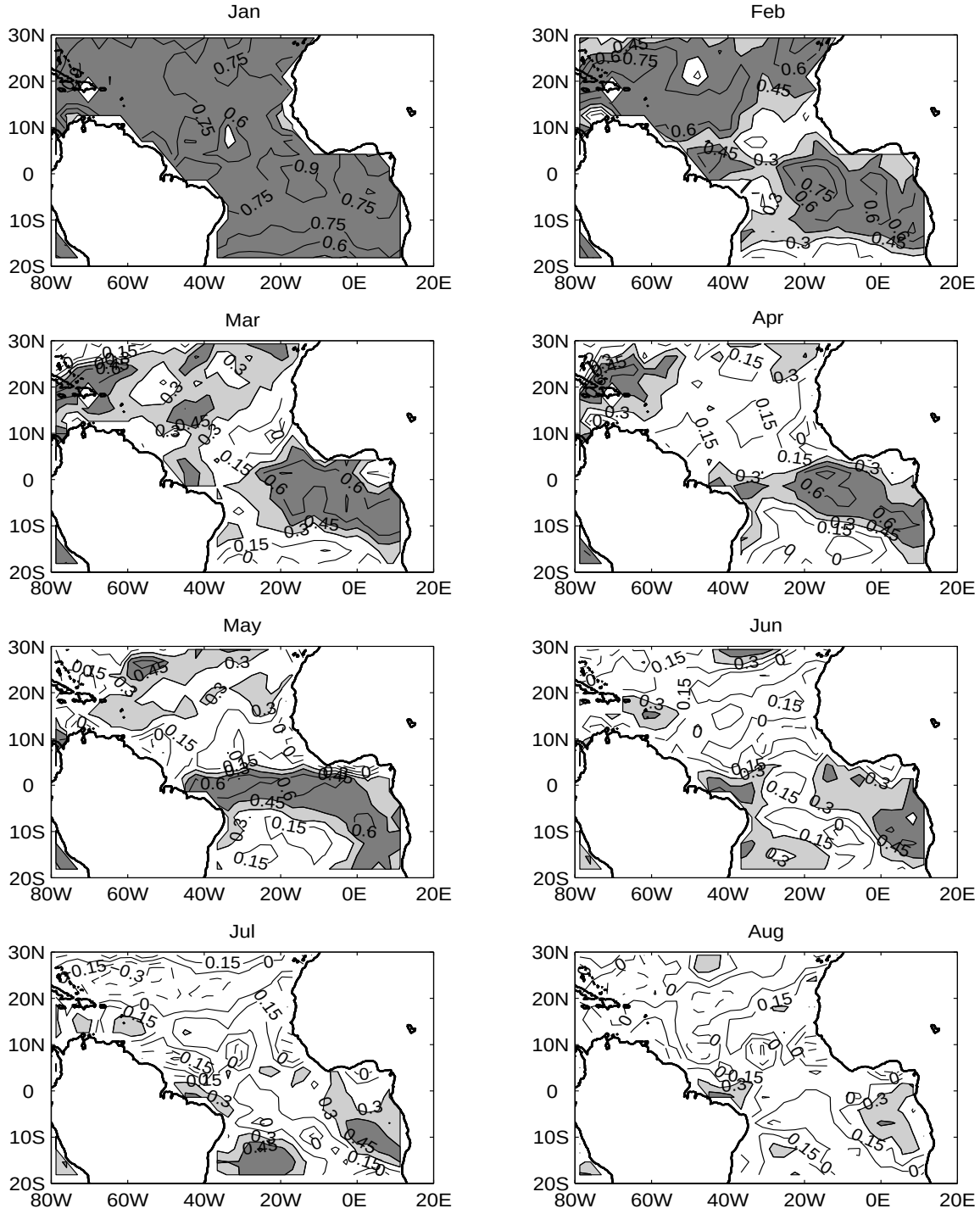

Fig. 34. Correlation between SST given by a persistence forecast and observed SST. Shading as in Figure 32.

from the tropical Pacific. *Chang et al.* [2003a] propose two ways in which the air-sea feedback may lead to the SST predictability, and they imply different conceptual models of ocean-atmosphere interaction. The first way is through reduced thermal damping of anomalous SST. In this case the coupled system can be described by a 1-dimensional mixed layer model with an adjusted damping coefficient, like a Hasselmann model. A second possibility is that the air-sea feedback makes the system non-normal, that is, the normal modes are not orthogonal. In this latter a 1-dimensional energy balance model can no longer describe the coupled system. *Chang et al.* [2003b] explored the role of the non-normality in the prediction of SSTs in a simple model of TAV. They found that the predictability can arise from the interaction between the gradient mode and other coupled modes. The CCM3-ML is a very good model for prediction of SSTs in the TNA. In the ETSA region, on the other hand, the CCM3-ML does a poor job and cannot beat persistence. We assume this is because of the absence of ocean dynamics in the slab ocean, and will show below that the correction introduced to the slab ocean improves the forecast. It is interesting to note that PGIC has higher skill than PAIC in the ETSA region after March, hinting a possible role of remote influence in forcing the evolution of SSTs not only in the TNA but also in the ETSA SSTs.

b. Corrected prediction experiments

Figures 35 and 36 show the SST correlation maps for the CPAIC and CPGIC experiments, respectively. These are to be compared with Figures 32, 33 and 34. During January and February the corrected predictions show similar skill as the non-corrected ones. During MAM corrected and non-corrected predictions show generally similar skills. There is a tendency, however, for the corrected experiments to show higher skills in the eastern side of the deep northern tropics and reduced skill in the western

side. This is particularly true during April, and suggests an interaction between the eastern deep northern tropics and the central equatorial Atlantic. In the ETSA the corrected predictions are clearly superior to the non-corrected ones. Both the CPGIC and the CPAIC show large areas with skill above the 95% level which are absent in PGIC and PAIC. Comparison with Figure 34 shows that the corrected predictions show similar skill as persistence in the ETSA. In the next season, however, the corrected predictions outperform the non-corrected predictions as well as the persistence in the ETSA. In the TNA, on the other hand, the CPAIC shows lower skills than the PAIC, while the CPGIC shows comparable, if not lower, skill than PGIC. Thus, the correction is seen to improve the prediction in the ETSA during all months. In the TNA, the corrected predictions show similar skill as the non-corrected ones up to May, and tend to degrade skills afterwards for reasons that are not fully understood.

To test the sensitivity of the results to changes in the correction matrix B we run an additional experiment. We repeated the corrected prediction using global initial conditions with a correction matrix $B' = 2 * B$. A 10-member prediction set was constructed for the same period 1981 to 2000. The correlation of predicted SST with observed SST for this experiment reveals similar characteristics as for CPGIC (not shown). The skill in the ETSA is enhanced respect to the PGIC, although not as much as in CPGIC. In the TNA the skill is very similar to that of CPGIC. Thus, according to this test, the results of the corrected prediction are not highly sensitive to changes in the correction matrix B.

To further compare the corrected predictions with the non-corrected ones we constructed an index to characterize the gradient mode. This so-called gradient index is defined as the SST difference between the regions defined by (50°-20°W,4°-14°N) and (35°-5°W,4°-14°S). Figure 37a shows the correlation of the gradient index constructed for each prediction experiment with the observed gradient index. Clearly, the pre-

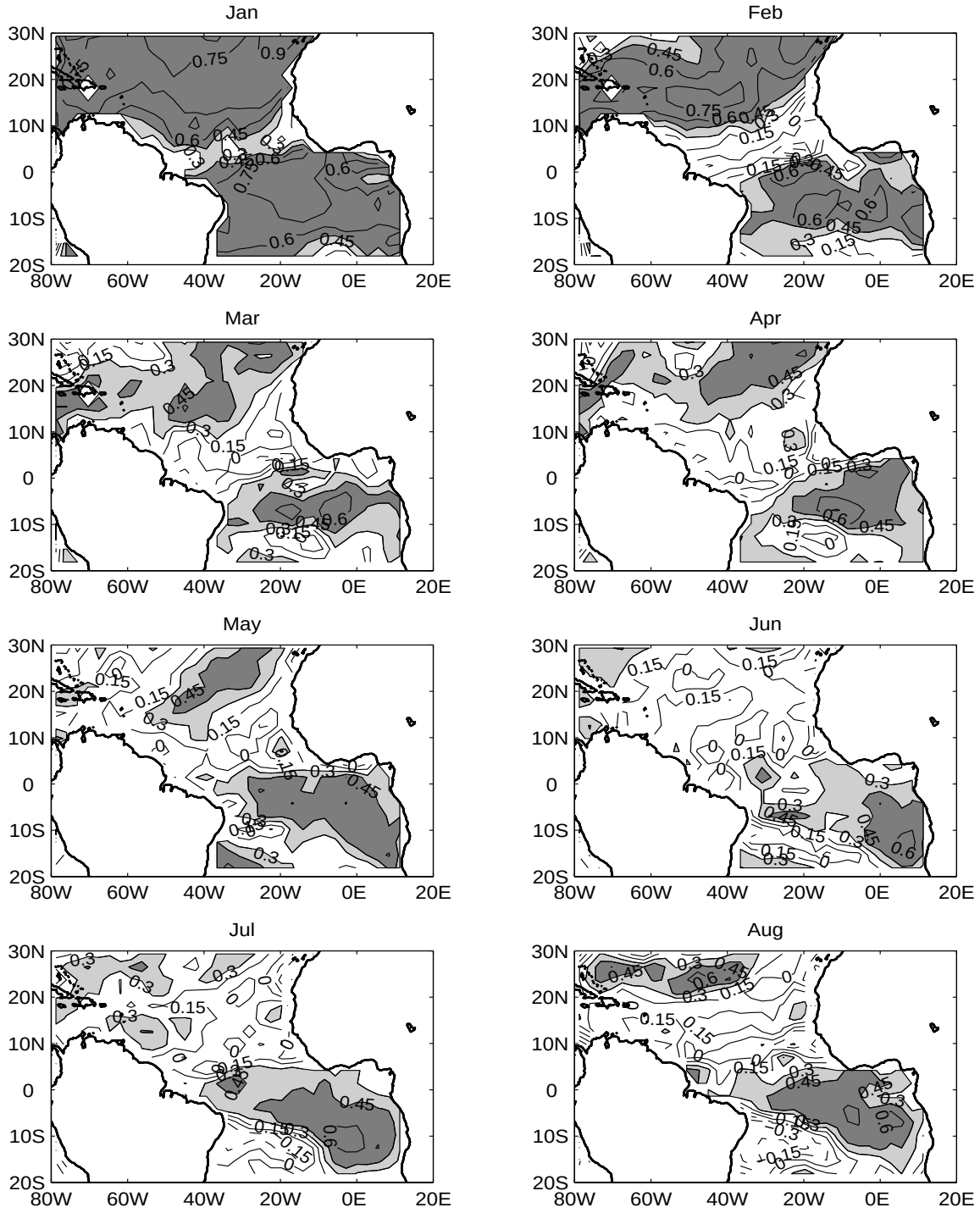

Fig. 35. Correlation between SST predicted by CPAIC experiment and observed SST for different months. Shading as in Figure 32.

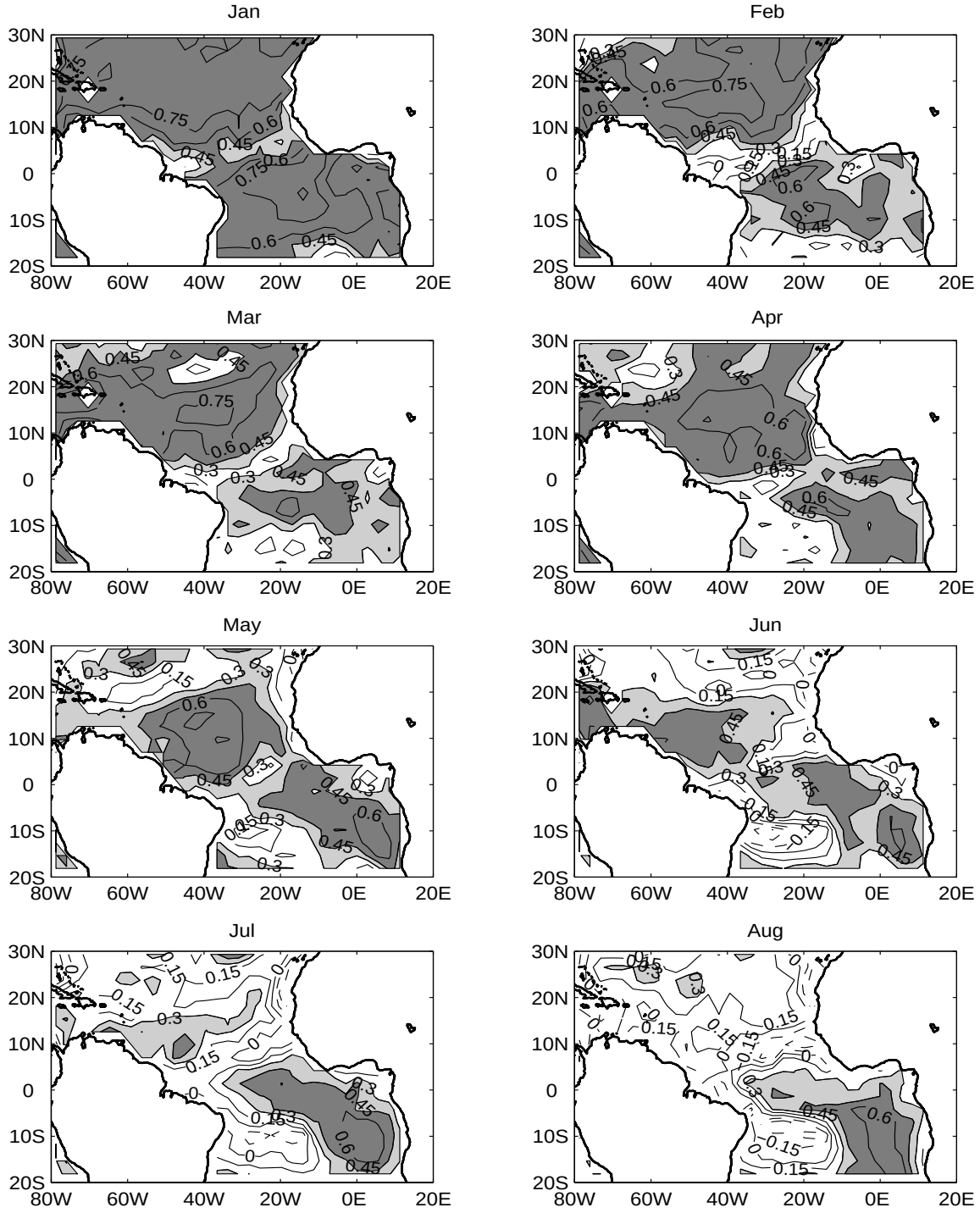

Fig. 36. Correlation between SST predicted by CPGIC experiment and observed SST for different months. Shading as in Figure 32.

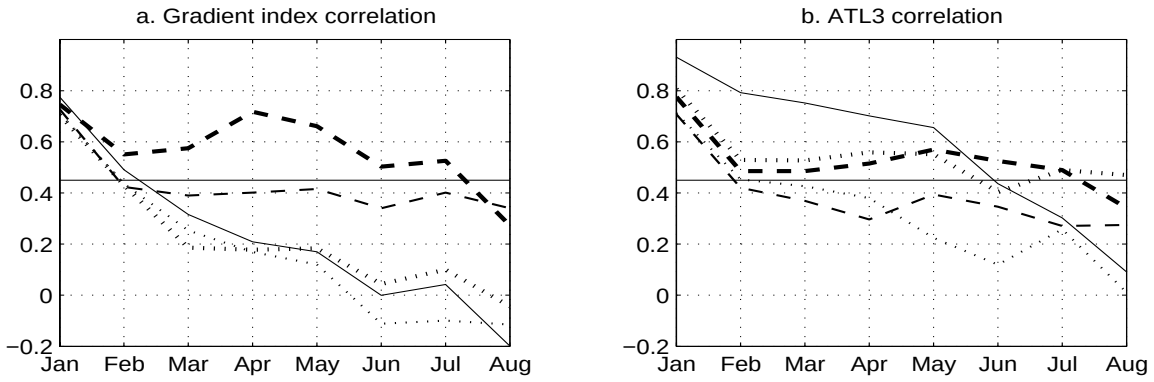

Fig. 37. Correlation between predicted and observed (a) gradient index, and (b) ATL3 index for each prediction experiment: PAIC (dotted line), PGIC (dashed line), CPAIC (bold dotted line), and CPGIC (bold dashed line). Persistence of the index is shown as a solid line. The horizontal line denotes the 95% significance level.

dicted gradient index is closer to observations when the CCM3-ML is initialized with global initial conditions. When the model is initialized with Atlantic initial conditions, the predicted gradient index is not better than the one given by the persistence forecast. These predictions have different skills in the two areas defining the gradient index, but none of the predictions is able to forecast both areas with high skill.

On the other hand, both predictions with global initial conditions (PGIC and CPGIC) beat the persistence after February. The non-corrected prediction (PGIC), however, shows a correlation skill of about $r = 0.4$ from February to July that is below the 95% significance level. The corrected prediction (CPGIC), on the contrary, is able to predict the gradient index with a correlation well above the 95% significance level up to July with a peak correlation value of $r \simeq 0.7$ during April-May. This value is significant at the 1% level. The enhanced correlation during March-April-May coincides with the peak season of the gradient mode suggesting that the corrected CCM3-ML initialized with global observed SSTs captures the dynamics of this mode much better than any other prediction.

The temporal evolution of the gradient index calculated from observations and from CPGIC is shown in Figure 38. In agreement with the high correlation skill, the sign of the dipole predicted by the ensemble mean is correct most of the times, although the amplitude is smaller because the average operation smoothes the anomalies. There are some years, however, in which the predicted dipole shows the opposite sign as the observed one; these are 1988, 1991, 2000 and 2001. The first two years are characterized by a rapid evolution toward a negative dipole that the model cannot capture. In years 2000 and 2001 the initial dipole was very weak (so as in 1991) and the model apparently is unable to determine its evolution. Unless remotely forced from the Pacific Ocean, initially small dipoles are generally very difficult to predict because the thermodynamic feedback is weak and thus SST anomalies are very sensitive to atmospheric perturbations. As a measure of the uncertainty in the prediction, Figure 38 also shows the spread of the ensemble members for each year. As expected, the spread (relative to the climatological noise) increases with lead time, thus decreasing the signal-to-noise ratio of the prediction.

The TAV also contains a zonal mode of variability characterized by a dynamical coupling between the winds and the SST in the equatorial region. It is believed to be akin to ENSO and peaks during boreal summer [*Zebiak*, 1993]. This mode is often characterized by the ATL3 index, which is the average of SST in the region (20°W-0°E,3°S-3°N). The correlation of the predicted ATL3 index with observations is shown in Figure 37b. Persistence is very high in this region and none of the prediction experiments is able to beat it until June. However, the corrected coupled model shows higher skill than the non-corrected ones, which show non-significant skills after a lead time of two months. The corrected model shows a skill of $r \simeq 0.5$ during almost all months. The absence of significant differences in skill between the corrected predictions (with the exception of June) suggests that this region is

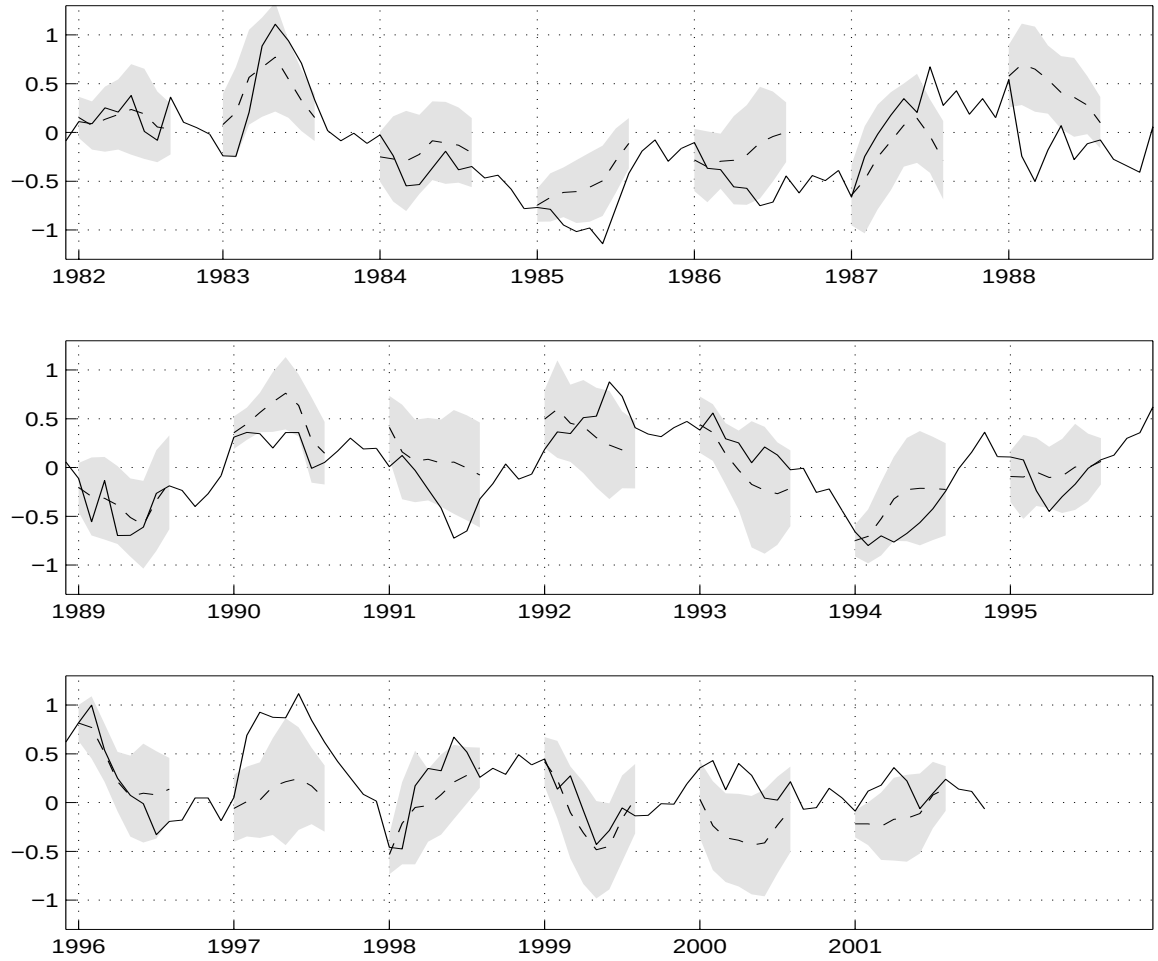

Fig. 38. Time evolution of the gradient index for observations (solid line), and from the ensemble mean of CPGIC (dashed line). The shading marks the standard deviation of the ensemble spread around the prediction for each year. Predictions are plotted only for months January to August. Label positions correspond to January of the particular year.

not affected by remote influences, or that the models do not capture correctly the governing dynamics even with the inclusion of the correction. The mechanisms that give so large persistence to the ATL3 region deserve further study.

c. Anomaly correlation

Another useful way to validate the predictions is to calculate the anomaly correlation between the predicted and the observed fields (hereafter AC, *Anderson et al.* [1999]). The AC measures the degree of spatial similarity between the predicted and observed fields at a particular time. Here, we report the results when the regional mean anomaly is subtracted from each grid point before the calculation of the AC. This favors comparison between dipole-like structures. We repeated the calculation without removing the regional mean and general conclusions do not change significantly, but the AC may change greatly for a particular year.

Figure 39 shows the AC in the region (60°W-20°E, 15°S-15°N) for the predicted SST of each prediction experiment as an average over all years. We consider this region because it encompasses the two indices that characterize the TAV. According to this measure, a model has a good skill if the anomaly correlation is larger than the AC of the persistence forecast. Clearly, using this measure, the PAIC has very limited skill over this region (Figure 39c). The AC of PAIC is always less than the AC of persistence and it shows large scatter among ensemble members with many of them showing negative AC at long lead times. The CPAIC experiment has more skill than PAIC mainly after May reinforcing the idea that the correction includes some local oceanic process (Figure 39a). The non-corrected prediction with global initial conditions (PGIC) is better than persistence during May-June. Finally, CPGIC has the best AC score, which is superior over the persistence after two months into the prediction. The scatter among ensemble members is relatively small, and in only two

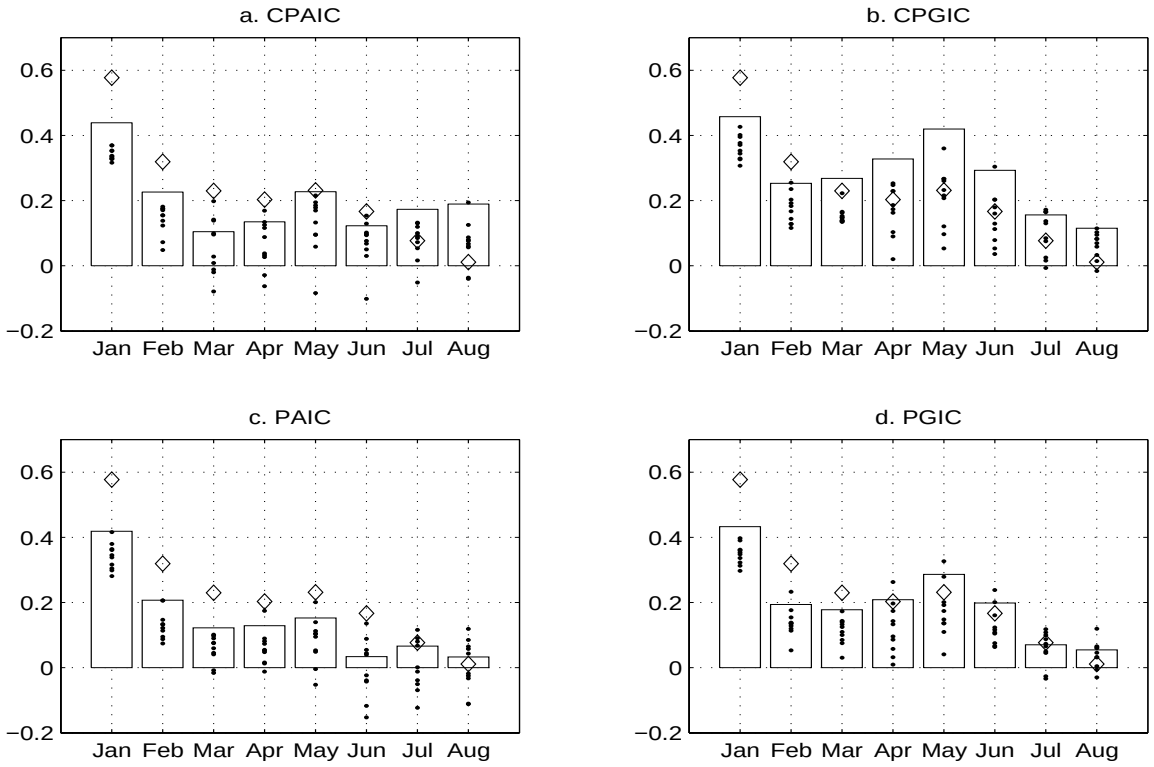

Fig. 39. Anomaly correlation for each prediction experiment as an average over all years. Bars denote the AC for the ensemble mean, and the dots are the AC for each ensemble member. The diamonds indicate the AC for the persistence forecast.

cases the AC becomes negative for long lead times (Figure 39b).

The AC peaks in April-May, again suggesting that the CPGIC can capture the dynamics of the gradient mode during boreal spring better than any other prediction experiment. This hints that the local process included in the correction can interact with the remote influence from the Pacific. To further investigate this issue we calculated the AC of SST for each year averaging over March to June for PGIC and CPGIC. The resultant time series for the two experiments characterize the degree of spatial similarity between the predicted and observed SST for each of the years during the period 1981 to 2000. Figure 40 shows the difference of AC between the

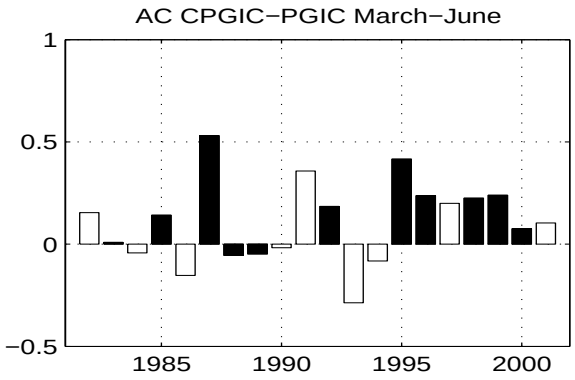

Fig. 40. Difference of AC between CPGIC and PGIC (ensemble means). The AC is calculated from March to June of each year. Black bars indicate ENSO years.

two experiments. The corrected prediction is better than the non-corrected in the majority of the years with the exception of 1986 and 1993. Also, during ENSO years the corrected prediction has a better or equal skill than the non-corrected prediction. Thus, this analysis supports the idea that the dynamics included in the correction can interact with remote effects through anomalous atmospheric circulations.

2. Prediction of precipitation

As mentioned above, the peak season of the gradient mode is MAM. It is during MAM that the ITCZ is closest to the equator bringing the rainy season to the north Northeastern region of Brazil, which extends over (35-45°W, 2-10°S) [*Hastenrath*, 1985]. In this and the following section, we shall explore how the improvement in the prediction of SST, and particularly in the cross-equatorial SST gradient, is translated to the prediction of precipitation in the tropical Atlantic.

Figure 41 shows the correlation between predicted and observed rainfall for each experiment during MAM in the period 1982-2000. Clearly, the corrected experiment with global initial conditions is the only one able to predict the variability of the Atlantic ITCZ across the whole basin with significant skill (Figure 41b). The corrected

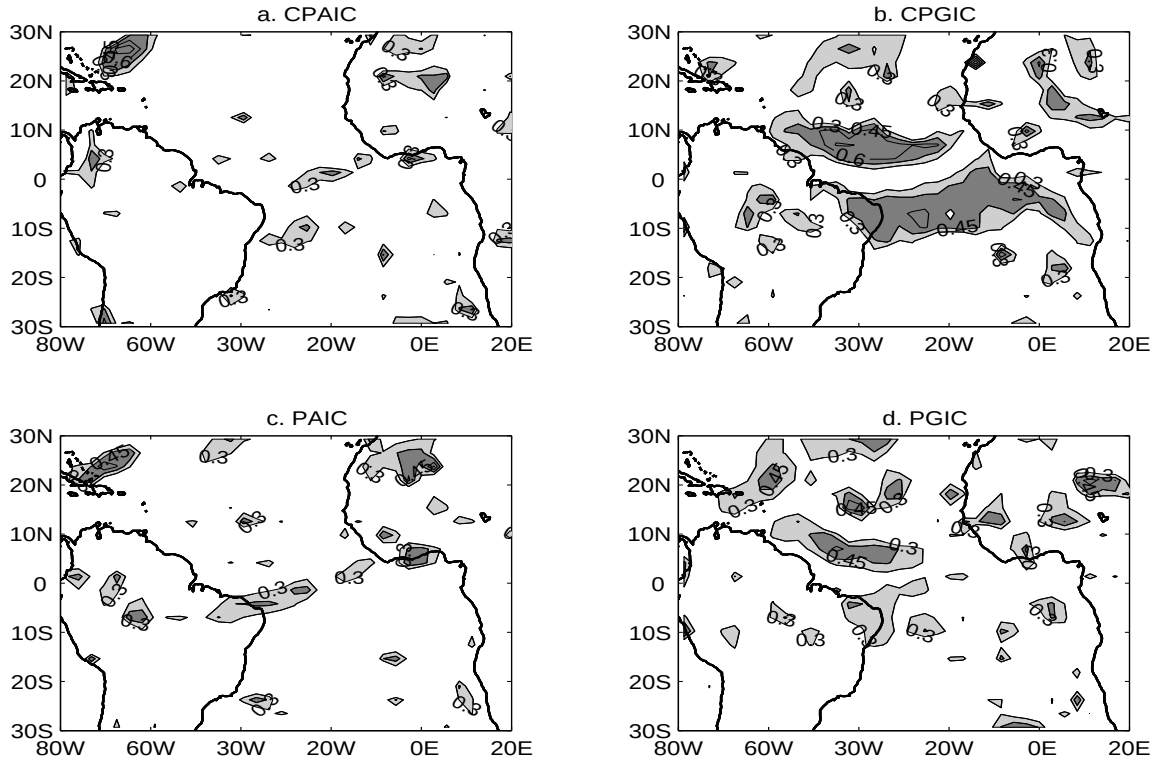

Fig. 41. Correlation between predicted and observed rainfall for (a) CPAIC, (b) CPGIC, (c) PAIC, and (d) PGIC. The contour interval is 0.15. Light shading indicates values above $r = 0.3$, and dark shading indicates values above $r = 0.45$. Values larger than $r = 0.45$ are significant at the 95% level.

experiment with Atlantic-only initial conditions (CPAIC) is not able to capture the displacements and changes of intensity of the ITCZ (Figure 41a). The non-corrected experiment with Atlantic-only initial conditions (PAIC) also shows very poor skill in predicting rainfall over the ocean, but shows some skill in predicting rainfall over Northeastern Brazil (Figure 41c). Finally, the PGIC experiment shows some skill in predicting the rainfall variations associated with the ITCZ, mainly north of the equator (where SST is predicted with more skill), and in Northeastern Brazil.

According to Figure 37a, CPGIC predicts the cross-equatorial SST gradient with the best skill among the predictions, then PGIC, and finally the predictions initial-

ized with Atlantic-only SSTs. Thus, the better the cross-equatorial SST gradient is predicted, the better are predicted the rainfall anomalies in the ITCZ. This is consistent with a large body of literature showing the link between the ITCZ position (and intensity) and the cross-equatorial SST gradient, the main characteristic of the gradient mode of variability (see Figure 20). These results confirm that the corrected coupled model initialized with global SSTs is the configuration that better captures the dynamics of the gradient mode.

Different AGCMs simulate differently teleconnections and local processes. Thus, it is useful to have a measure of the maximum skill of a particular model to know how close predictions are able to forecast climate within the context of a particular model. To do so, we use a 10-member ensemble of GOGA integrations in which the CCM3 model is forced with global observed SSTs. The correlation between the rainfall simulated by this experiment and the observations gives an upper limit of the model's skill in predicting precipitation because SSTs are perfectly known in advance. The GOGA experiment covers the period 1950-1994. Since the Xie-Arkin data set is available from 1979 to 2000, the correlation is performed during the MAM seasons of 1979 to 1994. Although it is not the same time period as that covered by the prediction runs, the analysis allows identifying the regions where the CCM3 has skill in predicting rainfall. Figure 42 shows the map of maximum correlation skill of rainfall simulated by the CCM3 during MAM. The CCM3 shows large skill across the Atlantic ITCZ region, and in the Caribbean. Here, we focus on the ITCZ. The shape of the region with maximum precipitation skill is very similar to the region where the CPGIC shows high skill (compare Figures 42 and 41b)). However, the latter shows a maximum skill of $r = 0.65$, while the maximum skill reaches $r = 0.9$ in certain areas. Thus, although CPGIC does a good job predicting rainfall, there is still room to improve the skill of the coupled model (see next section).

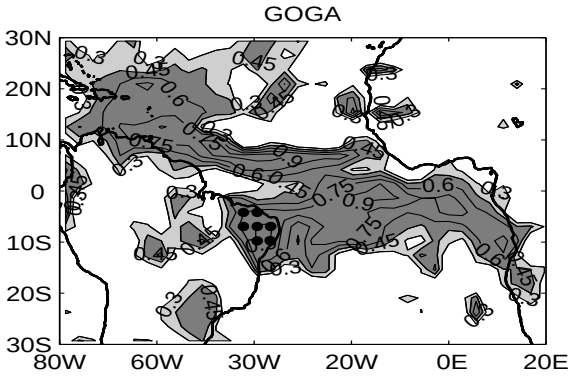

Fig. 42. Correlation between predicted and observed rainfall for GOGA experiment. Contours and shading as in Figure 41. Values larger than $r = 0.5$ are significant at the 95% level.

The Northeastern region of Brazil is the largest continental area where the CCM3 shows high skill in predicting rainfall during the MAM season. To further compare precipitation skill among the prediction runs we constructed an index over Northeastern Brazil as the average of the grid points shown in Figure 42. As expected from Figure 41, the CPGIC shows largest skill with $r = 0.59$, while the PGIC shows significant skill with $r = 0.48$. The predictions initialized with Atlantic-only SSTs do not show significant skill, mainly because they are not able to predict the cross-equatorial SST gradient during MAM (Figure 37). A secondary effect may be the absence of the direct ENSO influence on precipitation over Northeastern Brazil (see also below).

3. Covariability of errors in predicted precipitation and SST

In the previous section it was found that CPGIC has higher skill in predicting rainfall than any other prediction experiment. The first order explanation is that CPGIC is able to predict with largest skill the cross-equatorial SST gradient. Here we further address this issue looking at the structure and evolution of the SST prediction errors that covary with errors in the predicted precipitation. Rainfall prediction errors may

arise due to systematic errors in the model, and due to an incorrect prediction of SST. Here we want to identify those errors that arise due to errors in the predicted SST only. Thus, rainfall prediction errors are defined as the difference between the predicted rainfall and the simulated rainfall when perfect SSTs are imposed as boundary conditions to the CCM3. The latter is calculated as the simulated rainfall of the ensemble mean of a GOGA ensemble of integrations. For the SST field the error is defined as the predicted SST minus the observed SST (imposed in GOGA runs). The analysis is performed from 1982 to 1994, the common period shared by the prediction runs and the GOGA integrations. We used a joint singular value decomposition (SVD) analysis between the predicted SST error and the predicted rainfall error. The SVD analysis is designed to find the coupled patterns that maximize the temporal cross-covariance between two fields (see *Bretherton et al.* [1992] for an overview).

We compare the prediction errors of PGIC and CPGIC during MAM within the tropical Atlantic. Note that errors may arise from local processes as well as from remote teleconnections. Figures 43a and 43b show the leading covarying patterns of errors in the predicted SST and rainfall for PGIC. This SVD explains 61% of the squared covariance, and the time series associated with these patterns are correlated at $r = 0.95$. The SVD consists of a large cross-equatorial SST gradient confined to the deep tropics accompanied by a dipole of precipitation anomalies crossing the whole basin along the equator. Thus, errors in the predicted rainfall are, to a first order of approximation, dependent on the deep tropical SSTs, and the sign is consistent with a shift of the ITCZ toward the warmer hemisphere. The time series associated with this SVD are not correlated with SSTs outside the tropical Atlantic, showing that the SVD involves only local processes. The non-corrected slab ocean does not have any ocean dynamics, and thus, it is expected that it will tend to exaggerate the importance of feedbacks between the SST and surface heat fluxes. This will tend

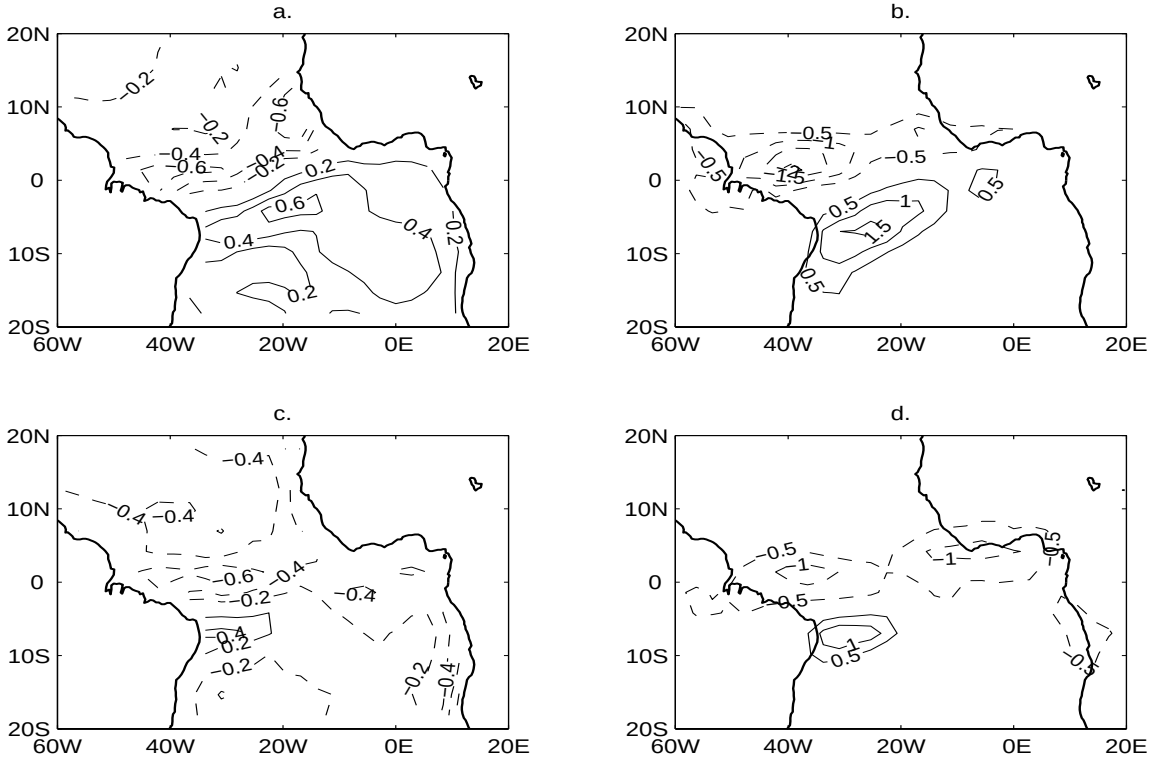

Fig. 43. Leading SVD of covarying errors in predicted SST and rainfall during MAM for (a), (b) PGIC, and (c), (d) CPGIC.

to favor an SST evolution with dipole-like characteristics, which may not be always present in reality (see also section E). Therefore, rainfall could be predicted with higher skill if the processes that govern the evolution of the SST in the deep tropics can be better modeled. This is at least partially attained introducing the correction in the SST equation of the slab ocean.

The leading SVD of prediction errors for the CPGIC is shown in Figures 43c and 43d. It explains 71% of the squared covariance, and the time series are correlated at $r = 0.84$. The error in the predicted rainfall no longer shows a dipolar pattern. The rainfall structure consists of a large anomaly that tends to be aligned along the equator, and a smaller anomaly between 5-10°S of opposite sign (Figure 43d). The SST error pattern has largest loading in the TNA, and presents an SST gradient

confined west of 20°W (Figure 43c). In the ETSA, particularly to the east of 20°W, the SST anomaly is relatively small and shows no clear structure, suggesting that SST errors there do not contribute much to the precipitation error. Overall, in the CPGIC, the first order source of rainfall errors is no longer a large cross-equatorial gradient as in PGIC. This is consistent with the notion that the correction improves the evolution of the SST gradient, as shown in the previous section. The correction is most successful in the eastern side of the basin, and less so in the western side. In the next section we show that the correction introduces a mode of SST variability with largest loading in the eastern side of the basin, that explains the better skill of CPGIC in predicting SST and rainfall.

The time series associated with the leading SVD of CPGIC are significantly correlated at 95% level with SST prediction errors in the tropical Pacific during MAM. Also, the symmetric rainfall pattern of Figure 43d is reminiscent of the direct influence of ENSO on the tropical Atlantic ITCZ through an anomalous Walker circulation [*Saravanan and Chang*, 2000; *Chiang et al.*, 2002]. This suggests that rainfall errors involve not only local processes, but also remote influences. Further support comes from the non-significant correlation between the time series of the leading SVDs for PGIC and CPGIC. Thus, particularly for the CPGIC experiment, an improvement of SST prediction in the tropical Pacific and a better representation of the Atlantic response to Pacific forcing may lead to a more skillful prediction of SSTs and rainfall in the Atlantic.

E. Modes of SST evolution

In this section we shed light on the oceanic processes that are parameterized in the correction matrix B. To do so we compare the EOFs of observed SST with the EOFs

of SST calculated for the ensemble mean of each prediction experiment. We focus on MAM season, because it is the peak of the gradient mode, and when the corrected model shows largest skill. Since the equation for the slab ocean in the corrected experiments includes the term BT the SSTs will evolve differently from those in the non-corrected ones, and thus their respective EOFs are expected to be different. We expect the EOFs of the corrected experiments to show larger similarity in spatial structure and temporal evolution with the observed ones, which would explain the higher skill in predicting SST and precipitation. It is worth noting, however, that the observed EOFs will include signal as well as noise variance, while the EOFs of the prediction experiments will mainly contain the signal part of the variance because the ensemble mean is used.

1. EOFs of observed SST

The EOFs of observed SST in the region (60°W-20°E,20°S-20°N), as well as their principal components are shown in Figure 44. The two EOFs are well separated from the rest and explain 44% and 32% of the total variance. The dipole structure of the leading EOF is very similar to the pattern of SST that characterizes the gradient mode (Figure 20), but with less weight in the TNA. There are two main centers of action, one next to the coast of Africa between 5°-20°S, and the other just south of the equator in the longitudinal band between 25°W-0°E. North of this last center of action there is a weaker SST anomaly of opposite sign next to the coast of Africa at about 10°N. The cross equatorial gradient of SSTs is accompanied by large cross-equatorial surface winds (Figure 44e) as in Figure 20. The second EOF has loading mainly in the TNA and is accompanied by northeasterly anomalies that support the notion of atmosphere to ocean forcing (Figure 44f). Weak cross-equatorial winds can also be seen in the westernmost side of the basin.

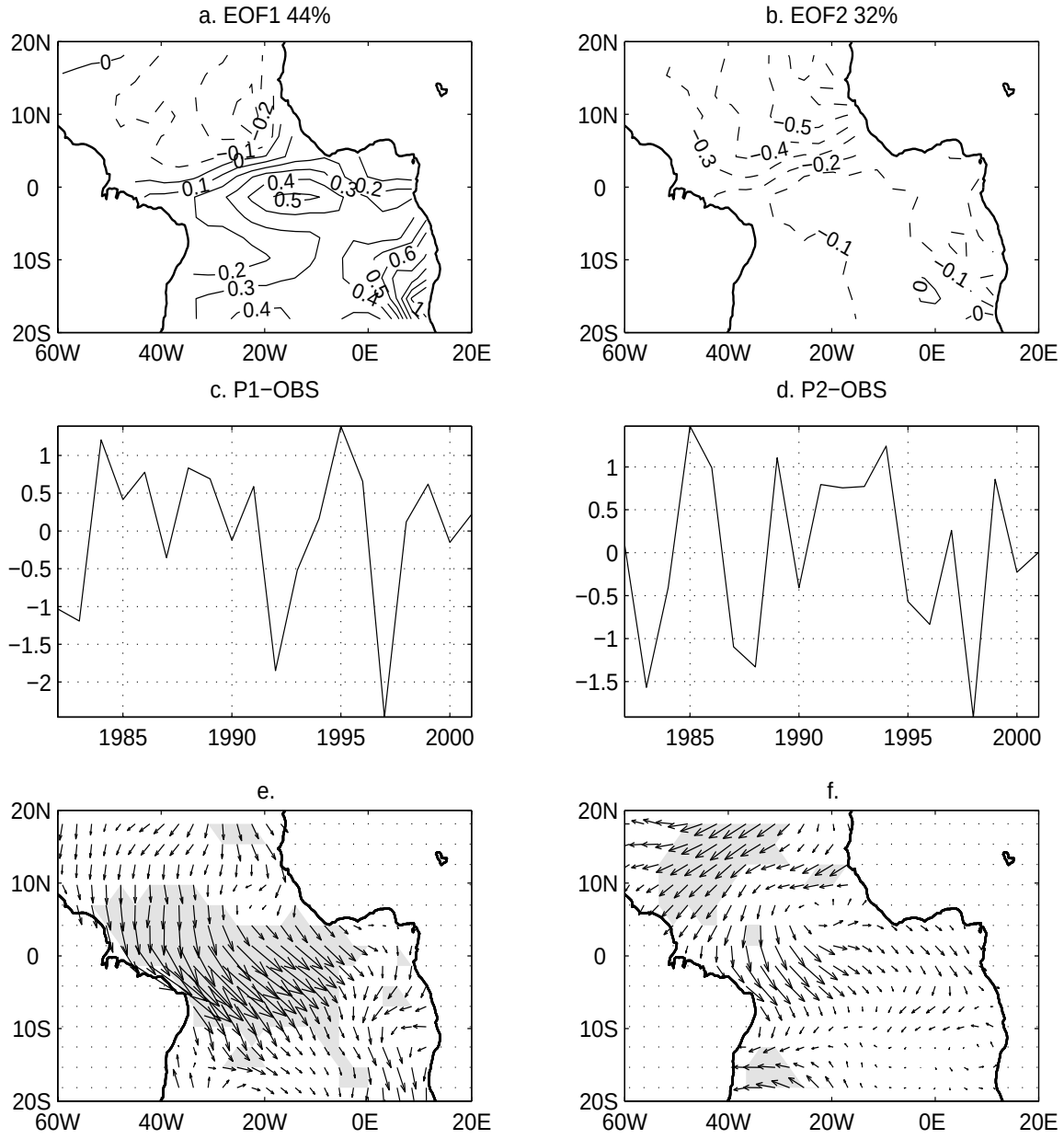

Fig. 44. Leading EOFs of observed SST during March-April-May. (a) Spatial pattern of leading EOF, and (b) spatial pattern of second EOF. Principal components associated to (c) leading EOF, and (d) second EOF. Regression of 925mb winds onto principal components associated to (e) leading EOF, and (f) second EOF. Shading in (e) and (f) indicate significance at 95% level.

A lag regression reveals large SST anomalies in the tropical Pacific and strong winds in the TNA forcing the SST below during the previous season. Thus, this second EOF appears to be the manifestation of ENSO influence on the TNA, in agreement with previous studies [*Enfield and Mayer*, 1997]. A similar lag regression for the leading EOF does not reveal a significant connection with the tropical Pacific. It shows SST anomalies in the ETSA developing simultaneously with large surface wind anomalies between the equator and 30°S in the Atlantic basin (not shown). Significant northeasterly winds are also present in the northern tropics (see also below). A simultaneous regression, on the other hand, shows significant correlation with the Pacific basin in the Niño3 region. Thus, this mode is largely locally generated, but may also be remotely connected to the equatorial Pacific.

To investigate how the leading mode of SST is generated and how it interacts with the atmosphere, we considered the terms of the linearized equation for the temperature tendency

$$\frac{\partial T'}{\partial t} = -\bar{u}\frac{\partial T'}{\partial x} - \bar{v}\frac{\partial T'}{\partial y} - \bar{w}\frac{\partial T'}{\partial z} - u'\frac{\partial \bar{T}}{\partial x} - v'\frac{\partial \bar{T}}{\partial y} - w'\frac{\partial \bar{T}}{\partial z} + Q'. \tag{4.11}$$

The net surface heat flux Q' includes the latent, sensible and radiative fluxes. In the previous chapter we have shown that the wind-induced latent heat flux is the dominant mechanism through which heat fluxes interact with SST in the tropical Atlantic, consistent with the literature. Thus, in this study, we consider the wind speed variability as a good indicator of surface heat flux.

The advective terms in equation (4.11) involve the velocity $\mathbf{u}$ of the upper ocean. The velocity can be decomposed into a geostrophic part and an Ekman part. Here we will only consider the latter because of the lack of hydrographic data. The horizontal Ekman currents $\mathbf{u_E^H}$ are that part of the total field that balances the wind stress. Since the balance depends on the Coriolis acceleration, it is singular at the equator

where the Coriolis parameter $f = 0$. To avoid this singularity a frictional term is included in the balance [*Zebiak and Cane*, 1987]. As a result the horizontal Ekman transport ($\mathbf{U_E^H} = \int_{-\mathbf{H}}^{\mathbf{0}} \mathbf{u_E^H dz}$, H the depth of the Ekman layer) can be written as

$$\mathbf{U_E^H} = (U_E, V_E) = \frac{1}{\rho(f^2 + \gamma^2)}(f\tau_y + \gamma\tau_x, -f\tau_x + \gamma\tau_y), \tag{4.12}$$

where ρ is the density of ocean water. The parameter γ is the damping time scale associated with the frictional term included in the balance. We used a value of $\gamma = 0.5 day^{-1}$ as in *Zebiak and Cane* [1987] and *Sterl and Hazeleger* [2003]. The Ekman pumping velocity is calculated assuming that the Ekman transport is non-divergent. Thus,

$$w_E = \nabla . \mathbf{U_E^H}. \tag{4.13}$$

Note that setting $\gamma = 0$ in equation (4.12) we recover the usual form of the Ekman transport. The equation for the SST tendency thus results in

$$\frac{\partial T}{\partial t} \simeq -\bar{u}_E \frac{\partial T'}{\partial x} - \bar{v}_E \frac{\partial T'}{\partial y} - u'_E \frac{\partial \bar{T}}{\partial x} - v'_E \frac{\partial \bar{T}}{\partial y} - w'_E \frac{\partial \bar{T}}{\partial z} + Q'. \tag{4.14}$$

The term involving $\bar{w}$ has been dropped because it involves knowledge of the vertical structure of the ocean that is not available to us. We do not imply that this term is not important in the generation of the leading EOF of SST, but its role will be addressed in future work. The climatological vertical temperature gradient is considered constant and we approximate $\frac{\partial \bar{T}}{\partial z} \simeq \frac{\Delta T}{H} \simeq \frac{2K}{50m}$ following *Sterl and Hazeleger* [2003], which is a conservative estimate for equatorial regions.

The SST variability is the time integral of the SST tendency. Thus, SST anomalies lag the terms of the SST tendency equation. Since we are trying to explain the origin of seasonally averaged SST anomalies, the SST variability may be related to the tendency terms within the same season (MAM), or be a response from the pre-

vious season (December-January-February, DJF). A lag regression of each tendency term indicates that only wind-speed anomalies and Ekman pumping during DJF are significantly correlated with the SST anomalies of the leading EOF (not shown). The lag regression reveals significant wind speed anomalies on both hemispheres suggesting an atmospheric forcing origin to the off-equatorial SST anomalies seen in Figure 44a. These wind anomalies weaken in MAM (see below). On the other hand, on the equatorial region wind speed and Ekman pumping anomalies in DJF are similar but weaker than during MAM. Thus, the SST anomaly there is related to the tendency terms mainly within the MAM season, and is not likely to depend only on wind-induced heat fluxes.

The simultaneous regression of the six terms of the tendency equation (4.14) onto the time series associated with the leading EOF of observed SST during MAM are shown in Figure 45. In agreement with the wind pattern shown in Figure 44e there is a large anomaly in the wind speed in the western and central region mainly to the south of the equator. The wind speed anomaly is broad and further west from the maximum SST anomaly. Thus, we do not expect the heat flux to create such a localized SST anomaly, but it helps in sustaining the SST off the equator. The inspection of the advective terms shows that the Ekman pumping is the most important term generating the SST anomaly on the equatorial region associated with the leading EOF.

Large anomalous downwelling in a region of climatological upwelling creates the warm SST anomaly south of the equator. A separation of Ekman pumping into the contributions due to the wind stress components indicates that zonal wind stress anomalies are largely responsible for the SST anomaly with maximum just south of the equator at about 15°W. Meridional wind stress anomalies generate a weaker Ekman pumping with maximum next to the African coast at about 5°S (not shown).

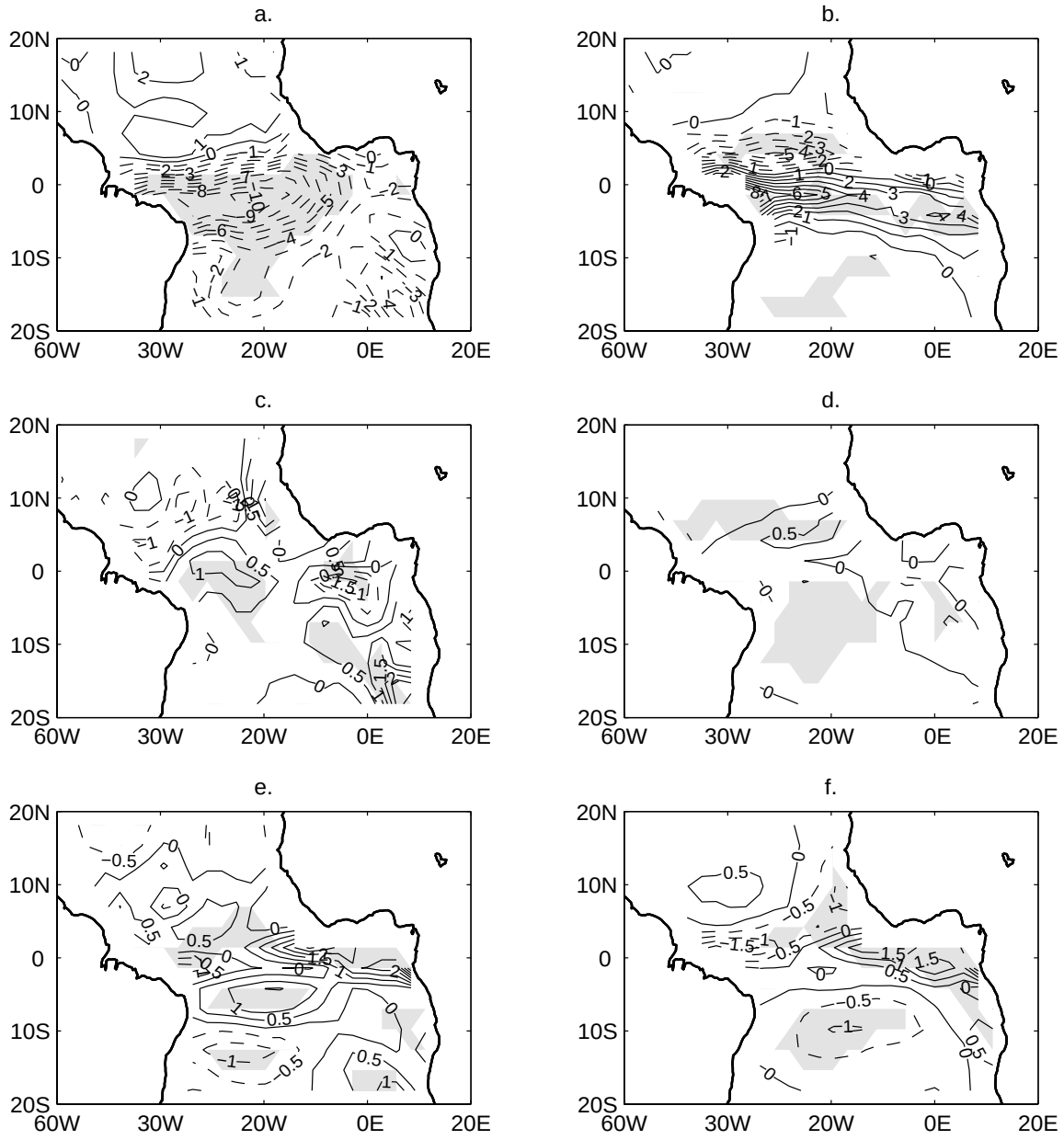

Fig. 45. Regression of (a) wind speed, (b) $-w'_E \frac{\partial \bar{T}}{\partial z}$, (c) $-\bar{u}_E \frac{\partial T'}{\partial x}$, (d) $-u'_E \frac{\partial \bar{T}}{\partial x}$, (e) $-\bar{v}_E \frac{\partial T'}{\partial y}$, (e) $-v'_E \frac{\partial \bar{T}}{\partial y}$ onto the principal component of the leading EOF of observed SST. Shading indicates significance at the 95% level. In (a) the units are $10^{-1} ms^{-1}$, and in (b)-(e) the units are $10^{-8} Ks^{-1}$. Note that in (b) contour interval is double from that of (c)-(e).

The other advective terms are relatively small. Advection of anomalous temperature by the mean zonal currents damps the equatorial SST anomaly to the east and strengthens it to the west, thus tending to shift it westward. The advection of mean temperatures by anomalous zonal currents is negligible. The advection of anomalous temperature by the mean meridional currents tends to help the development of eastern equatorial SST anomalies, and damp western equatorial SSTs. The term $-v'_E \frac{\partial \bar{T}}{\partial y}$ contributes to warming eastern equatorial SSTs, and damp SST anomalies poleward of about 5°S.

2. EOFs of predicted SST

Figure 46 shows the two leading EOFs during boreal spring calculated for the ensemble mean of each prediction experiment. The correlations of the associated principal components with the observed principal components are summarized in Table VI.

In all cases the EOFs explain together close to 80% of the total variance as in observations. The spatial structures and time evolutions are, however, dependent on the prediction experiments. In PAIC the SST evolution is largely dominated by the leading EOF that explains 60% of the total variance. The spatial pattern is dipole-like with largest weight in the western equatorial Atlantic (Figure 46a). The second EOF is close to a monopole (Figure 46b). The time series associated with these EOFs show no significant correlation with the time series of observed EOFs (Table VI).

In PGIC the two patterns explain similar amounts of variance (Figures 46c and 46d). The first EOF has SST anomalies of same sign across the basin with largest weight in the cold tongue region. Its corresponding principal component is correlated with the PC of the second observed EOF at $r = 0.48$. The pattern of the second EOF of PGIC looks very close to the leading EOF of PAIC, and shows no correlation with observed EOFs. The time series associated with the third EOF of PGIC is

Table VI. Correlation between principal components of EOFs of observed SST (P1-OBS, P2-OBS) and principal components associated with EOFs of predicted SST for each prediction experiment. The "*" indicate correlations not significant at the 95% level.

		P1-OBS	**P2-OBS**
PAIC	P1	*	*
	P2	*	*
PGIC	P1	*	0.48
	P2	*	*
CPAIC	P1	*	*
	P2	0.45	*
CPGIC	P1	*	0.55
	P2	0.64	*

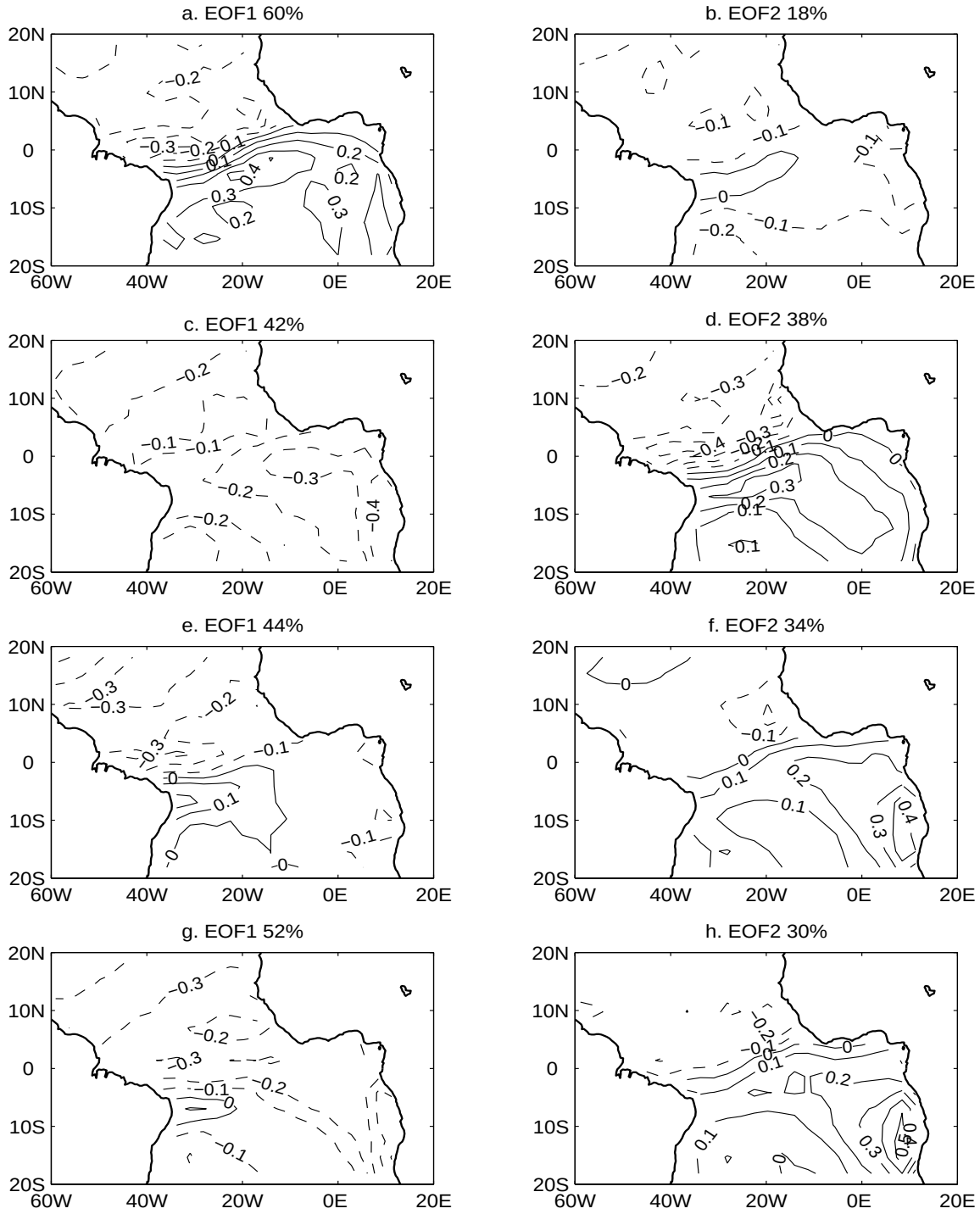

Fig. 46. Leading EOFs of predicted SSTs for PAIC (a,b), PGIC (c,d), CPAIC (e,f) and CPGIC (g,h).

significantly correlated at 95% level with the first observed EOF. However, it explains only 8% of the variance and SST anomalies are confined south of 5°S (not shown).

The corrected prediction experiments show very interesting results. The EOFs of the CPAIC explain 44% and 34% of the total variance respectively. The leading EOF resembles the first EOF of PAIC but the SST anomaly is confined to the western side of the basin. The spatial structure of the second EOF is more revealing. It is distinct from the EOFs of either of the non-corrected experiments. It shows a dipole-like structure with largest loading in the cold tongue region and a second maximum in the TNA at about 10°N next to the coast of Africa. This pattern is similar to the leading EOF of observed SST and their time series are significantly correlated at 95% significance level (Table VI). This EOF seems to include a representation of the interaction between the SSTs next to Africa and the central equatorial Atlantic, which increases the correlation skill of the corrected predictions in these regions.

The corrected experiment with global initial conditions (CPGIC) shows EOFs that are even more similar to the observed ones. The leading EOF explains 52% of the total variance. Its structure is similar to the second observed EOF and their time series are correlated with $r = 0.55$. The second EOF explains 30% of the total variance and looks very close to the second EOF of CPAIC. It is correlated to the first observed EOF with $r = 0.64$, significant at 99% level. The correlation between the principal component and the observed SSTs is largest in the deep tropical Atlantic, showing that the second EOF of CPGIC captures the variability of the cross-equatorial SST gradient.

In summary, the second EOFs of the corrected experiments are similar in structure and are significantly correlated to the leading observed EOF. Moreover, the non-corrected predictions do not show such a pattern, and none of their leading EOFs are correlated with the first EOF of observations. This points to the fact that

the non-corrected experiments lack the physics responsible for the generation of the SST anomalies associated with the first observed EOF, which in the previous section was found to be consistent with Ekman dynamics. This is particularly true for the SST anomaly in the equatorial region; off-equatorial SST anomalies are mainly driven by wind-induced heat fluxes. Therefore, we conclude that matrix B includes a parameterization of the Ekman dynamics. This is true to the extent that the analysis presented in section E.1 represents well the variability of observed SST. Matrix B could also include a parameterization of terms involving $\bar{w}$, which were not considered in our previous analysis.

It is worth noting that in the corrected experiments anomalous atmospheric heat fluxes are still the most important factor controlling the evolution of the SST (their leading EOF). The parameterized ocean dynamics appears mainly in the second EOF, contrary to observations, probably because of the indirect way it was introduced in the model. However, the parameterization of Ekman dynamics is still important because it allowed the corrected model to simulate better the evolution of SSTs, thus showing higher skill than the non-corrected experiments.

Finally, we found that CPAIC shows a second EOF related to ocean dynamics that is correlated to the leading EOF of observed SST. On the other hand, CPGIC shows a similar pattern but is better correlated to observations. Thus, this supports the idea that the processes generating the first EOF of SST are local, but can be influenced by remote SSTs. The mechanism involved deserves further study, but is beyond the scope of this work.

We next consider the difference between the predicted SST in CPGIC and PGIC. The difference in evolution is due to the correction term introduced in CPGIC (assuming the noise has been filtered). Figure 47 shows the leading EOF of the SST difference during boreal spring, which explains 52% of the total variance. The spatial

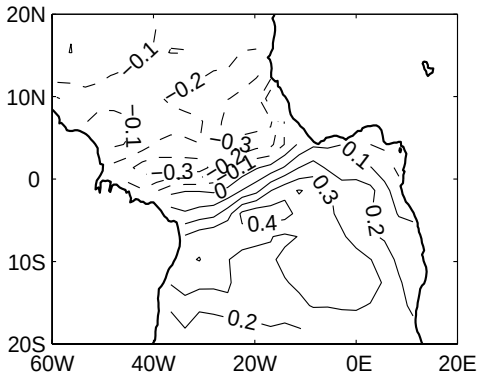

Fig. 47. Leading EOF of the SST difference between CPGIC and PGIC during MAM.

structure is very similar to the second EOF of PGIC and, in agreement with the EOFs shown in Figure 46, hints that PGIC tends to present stronger cross-equatorial SST gradients than CPGIC. This suggests that, during MAM, the role of the ocean (correction) is that of weakening the thermodynamic air-sea feedback between SST and the surface heat flux in the equatorial region.

To further investigate this, we constructed a composite of SST and surface winds for the extreme years of the time series associated with the pattern of Figure 47, and in which CPGIC is closer to observations than PGIC according to the AC. This results in the following positive years (1995, 1996, 1999), and negative years (1987, 1992, 1997, 1998). Figure 48 shows the composite of observations, PGIC and CPGIC for the months of December, February and May. In December the SST of the three data sets are very similar because the predictions are initialized with observed initial conditions. In February, the observations show northerly cross-equatorial winds accompanied with a weak SST gradient. On the contrary, PGIC has developed a large cross-equatorial SST gradient in the western side of the basin with southerly surface winds, that is, the opposed of observations. CPGIC also presents the wrong cross-equatorial gradient, but is much weaker. In May, observations show large positive

SST anomalies in the TSA with largest weight just south of the Equator, and negative SST anomalies in the TNA. The predicted SST and winds in PGIC during May have opposite sign from observations, thus tending to shift the ITCZ in the wrong direction. This is result of the strong positive feedback existing in PGIC that makes anomalies persist in the western side of the basin. In CPGIC, on the other hand, the predicted SST has the same sign and a similar shape as the observations. Consequently, the cross-equatorial winds are in the right direction and the ITCZ is shifted southward. This demonstrates that the ocean dynamics (correction) opposes the thermodynamic feedback, and is even able to change the sign of the cross-equatorial SST gradient. The initial conditions are fundamental to determine the relative importance of these two processes in the evolution of the SST.

The analysis of the leading observed EOF suggested that Ekman pumping is the most important term generating SST anomalies in the equatorial and cold tongue regions. We can test if Ekman pumping is responsible for the observed SST evolution shown in Figure 48 by constructing a composite of the SST evolution given only by the Ekman pumping term, that is,

$$T(t) = T(0) - \int_0^t w'_E \frac{\partial \bar{T}}{\partial z} dt, \tag{4.15}$$

with $T(0)$ the December SST. Figure 49 shows the composite of SST considering only the Ekman term, and the composite of observed SST.

Clearly, the evolution of the equatorial SST given by the Ekman pumping term only is very similar as that of the observed SST. The shape of the SST anomaly is very similar and has largest amplitude in May along the equatorial and cold tongue regions. The magnitude of the SST anomaly given by the Ekman pumping term is, however, about half of the observed one in May. This difference may be partly attributed to the chosen climatological value of the vertical temperature profile $\frac{\partial \bar{T}}{\partial z} = \frac{2}{50}\mathrm{Km}^{-1}$,

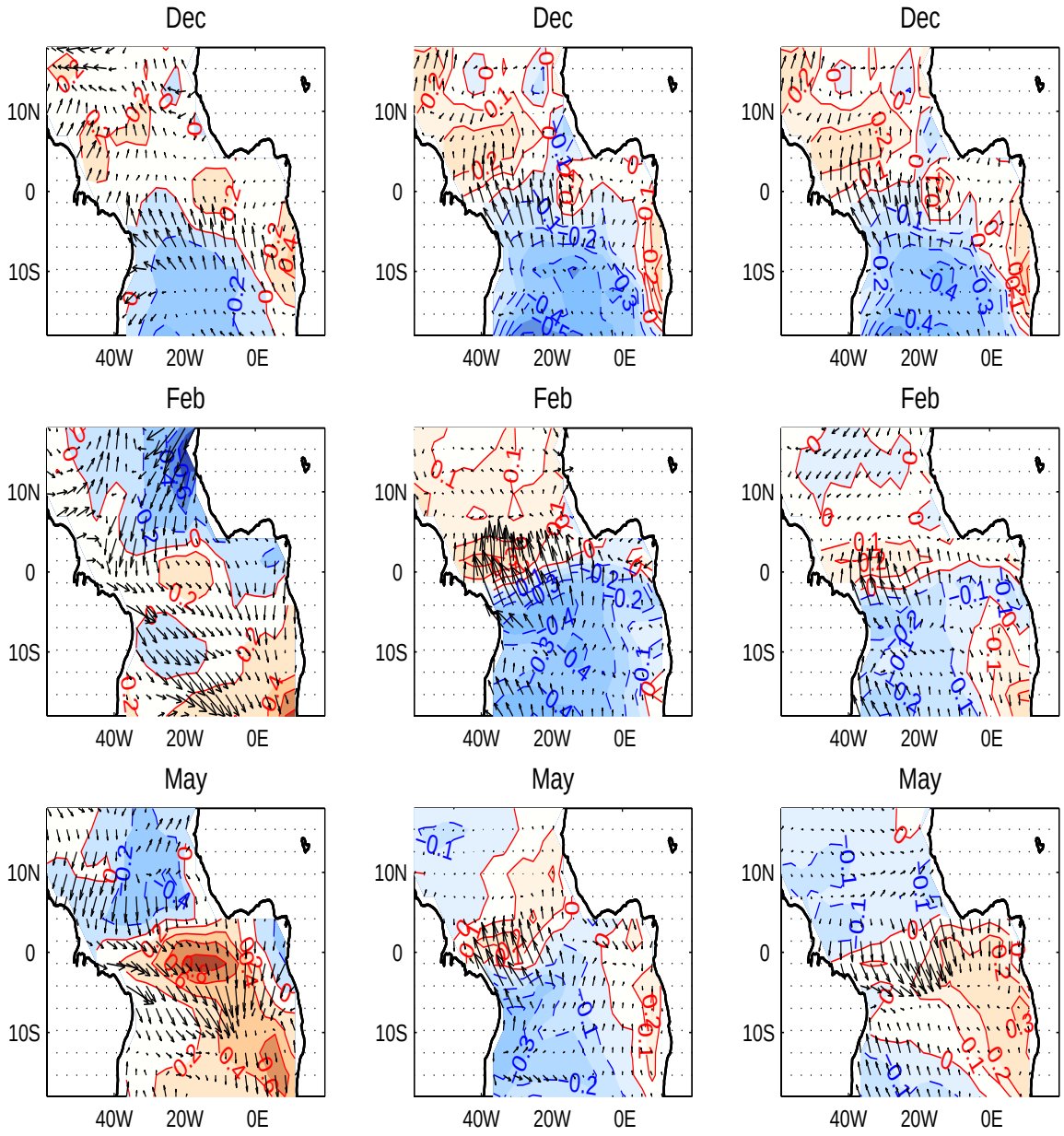

Fig. 48. Composite of SST and surface winds for observations (left panels), PGIC (middle panels) and CPGIC (right panels). The years used in the composite are extreme years of the EOF shown in Figure 47. Note that in the left panels the SST contours are 0.2K, while in the other panels the contours are 0.1K.

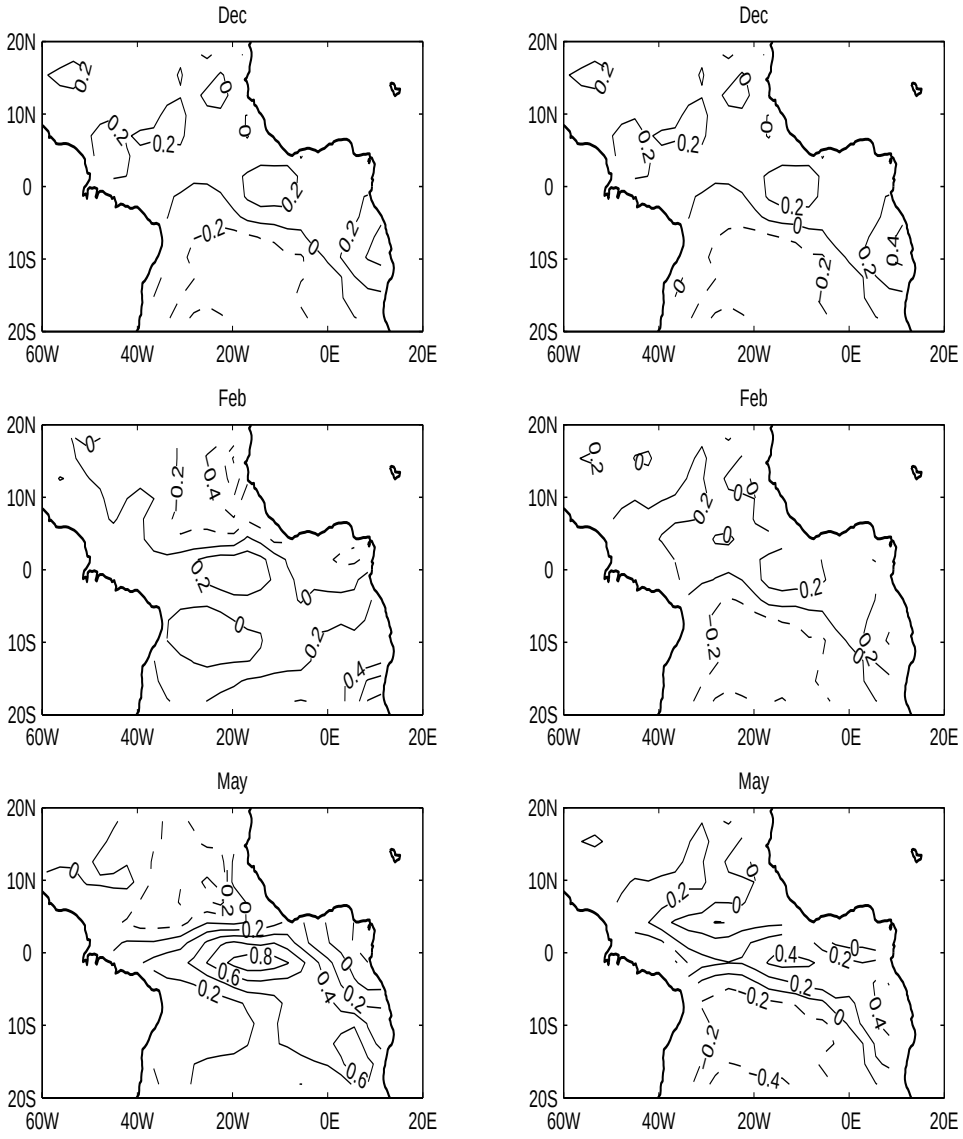

Fig. 49. Composite of observed SST (left panels), and the contribution of the Ekman pumping to SST evolution (right panels). The years used in the composite are extreme years of the EOF shown in Figure 47.

which is a conservative estimate for the equatorial region. Other ocean processes like meridional advection may also contribute to the generation of the SST anomaly. Note that, as expected, the Ekman pumping is not important in the off-equatorial regions, where surface heat flux dominates the SST variability. Overall, this analysis further supports the hypothesis that the correction includes a parameterization of Ekman dynamics, and particularly of the Ekman pumping term.

F. Summary

In this study we test the importance of ocean dynamics, and propose a new methodology to improve seasonal climate prediction in the tropical Atlantic. We use an AGCM coupled to a slab ocean, a configuration that was shown to have skill for prediction of SST in the tropical Atlantic, particularly in the TNA region [*Chang et al.*, 2003a]. We hypothesized that the low skill of the model in the equatorial and cold tongue regions can be attributed to the absence of ocean dynamics in the slab ocean. To improve the coupled model we developed a technique to introduce a statistical correction to the slab ocean that parameterizes the heat transport due to anomalous linear ocean dynamics. The main results are:

- The corrected predictions outperform the non-corrected predictions in the ETSA particularly at long lead times. This result indicates that the correction introduced in the slab ocean is successful in improving the prediction in that area, and points to the importance of ocean dynamics in the prediction of tropical Atlantic SSTs.

- The ATL3 index, which characterizes the zonal mode, is predicted in the corrected experiments with higher skill than in the non-corrected experiments. However, persistence is a better forecast model up to May, suggesting that the

correction does not parameterize all the processes governing the dynamics of the zonal mode.

- The predicted gradient index is better than persistence for almost all lags if the system is initialized with global SSTs, pointing to the importance of the remote influence from ENSO. Furthermore, highest skills are obtained for the corrected experiment (CPGIC). The correlation skill of CPGIC peaks in MAM reaching values close to $r = 0.7$, showing that this experiment represents very well the dynamics of the gradient mode. As result of the good prediction of the cross-equatorial SST gradient, CPGIC shows high skill in predicting rainfall anomalies in the ITCZ region during MAM across the Atlantic basin.

G. Discussion

The processes identified to be responsible for the evolution of equatorial SST anomalies associated with the leading EOF of observed SST during MAM are consistent with Ekman dynamics. Ekman pumping is particularly important for the observed evolution of the SST in the equatorial and cold tongue regions. We hypothesize that an Ekman feedback may be present, and that it may lead to enhance SST predictability in the TSA. This process requires a coupling between the surface winds and ocean currents, such that anomalous (mainly zonal) winds drive anomalous currents creating an horizontal divergence and thus anomalous Ekman pumping. The Ekman pumping (with the additional help of other advective terms) changes the SST. Subsequently, the winds respond to the hydrostatic pressure gradient generated by changes in SST, closing the loop. Matrix B seems to include a parameterization of this process, allowing the corrected model to better represent the evolution of SST anomalies. Further investigation with ocean models that explicitly incorporate Ekman dynamics

is needed.

We also found that, during MAM, the role of the ocean (correction) in the predictable dynamics of TAV is that of weakening the thermodynamic air-sea coupling between SST and heat flux in the equatorial region. This is consistent with previous studies of the role of ocean dynamics in regulating the SSTs associated with the gradient mode of variability. In an observational study *Chiang et al.* [2002] propose that while the role of the positive feedback is to sustain the SST gradient during boreal spring, the ocean heat transport in the equatorial region works against it preventing the gradient to persist into the next season. Recent modeling studies with ocean GCMs also support this notion. Studies by *Chang et al.* [2001], and *Seager et al.* [2001] suggest that the heat transport associated with the mean ocean circulation opposes the positive feedback and weakens the cross-equatorial SST gradient during MAM.

A better understanding of the importance of upper ocean processes in the prediction of SST anomalies requires the use of a hierarchy of coupled modes. This will allow a systematic separation of the different mechanisms operating in TAV. Nevertheless, the prediction experiments presented here demonstrate that coupled with a corrected slab ocean, an AGCM has large skill for prediction of SST and precipitation in the tropical Atlantic several months in advance. This is very encouraging for seasonal climate prediction in the tropical Atlantic during boreal winter and spring.

CHAPTER V

SUMMARY AND OPEN ISSUES

The overall goal of this study is to shed light on the physical processes that govern the variability and those that may enhance climate predictability in the Atlantic basin. The focus is on ocean-atmosphere interactions on seasonal-to-interannual time scales. Two main regions are studied: the South Atlantic convergence zone (SACZ), and the tropical Atlantic. In this section we summarize our findings and discuss some open issues that are desirable be addressed in future studies.

A. South Atlantic convergence zone

In Chapter II we investigated the interannual variability of the SACZ region during austral summer. An attempt was made to separate the total variance of the region into a forced component due to SST forcing (signal), and an internal component due to atmosphere internal variability and land-atmosphere interactions (noise).

Two main signals were detected: a locally forced signal located mainly in the oceanic portion of the SACZ consisting in a shift and strengthening of the SACZ toward anomalously warm waters, which varies on interannual-decadal time scales. The second signal is related to ENSO, and consists in a northeastward shift of the SACZ during warm events.

The leading mode of interannual internal variability of rainfall in the SACZ region shows a strengthening/weakening of the SACZ with an anomaly of opposite sign to its southwest. A potential predictability analysis reveals that the land portion of the SACZ is primarily dominated by internal variability, thereby having limited predictability at seasonal time scales. This result can be tested using the prediction

experiments of Chapter IV. An index for precipitation in the SACZ was constructed over the land portion of the region (40°-48°W,15°-22°S), which is the area of maximum observed variability (see Figure 2f). None of the experiments, either corrected or non-corrected, shows significant skill in predicting rainfall over that region during March. The correlation skill during January-February is largely independent on the introduction of the correction. The prediction experiments with global initial conditions have a correlation skill of 0.43 (PGIC), and of 0.46 (CPGIC), which are very close to the 95% significance level (0.45). The prediction experiments with Atlantic-only initial conditions (PAIC, CPAIC) show non-significant skill. These results clearly show that rainfall in the SACZ is very difficult to predict. Also, while local SSTs may add some predictability, the majority of the predictability in the region tends to come from the ENSO forced signal.

There are several open issues that need to be addressed to further understand the SACZ variability and predictability:

1. Two precipitation forced signals were identified in the SACZ during austral summer. Is there a subseasonal dependence in the occurrence of the signals? In the prediction experiments of Chapter IV the ENSO forced signal tends to occur at the beginning of the season. This may indicate a subseasonality in the signal, or may be due to a wrong representation of the teleconnection from the Pacific due to a non-perfect SST prediction there. We performed a preliminary signal-to-noise analysis for each month of the summer separately using the output from the CCM3. The analysis suggests that the ENSO-forced signal tends to be largest in January, while the local SST-forced signal dominates in February-March. Further investigation is needed.

2. The SACZ has been shown to have large intraseasonal variations linked to the

propagation of mid-latitude disturbances into the region [*Liebmann et al.*, 1999], and to the Madden-Julian Oscillation [*Paegle et al.*, 2000]. In this study we focused on the forced atmospheric response to the varying SSTs, because we are interested in the predictable part of the variance on interannual time scales. Also, the forced response can be considered in a first order approximation to be separated from the intraseasonal variability which mainly comes from internal dynamics. It is, however, worth exploring if the intraseasonal variability, mainly those associated to the Madden-Julian Oscillation, can add predictability on a monthly time scale to the SACZ.

3. Throughout this study we have not considered the impact of soil moisture on the predictability of precipitation in the SACZ. A high soil moisture content (may be product of anomalous rainfall) can produce higher evaporation, which in turn can induce additional precipitation through both local recycling and changes in the global circulation. If this land-atmosphere feedback does in fact operate, it may allow the translation of soil moisture anomalies into seasonal predictions of precipitation [*Koster et al.*, 2002]. *Koster et al.* [2000] have shown that the SACZ is in fact one of the regions in which the foreknowledge of the soil moisture state increases the predictability of precipitation. Thus, the study of land-atmosphere interaction may hold the key to improve rainfall prediction in the continental part of the SACZ.

B. Tropical Atlantic

Chapter III investigates the role of extratropical atmospheric variability on tropical Atlantic variability. It is found that the IAV of the SH can play a pre-conditioning role on the onset of the gradient mode, the main mode of coupled ocean-atmosphere

variability in the tropical Atlantic. The strong SH winter IAV generates an SST anomaly with maximum amplitude in the subtropical region through anomalous heat fluxes. After that initial kick, a positive air-sea feedback maintains and moves the center of maximum SST anomalies equatorward. As result, an SST dipole develops in the deep tropics in the following boreal spring, while the subtropical SST anomalies are damped out by heat losses.

A similar behavior results from the remote effect of the NAO, which peaks in austral summer. The differences are (1) that the SST anomalies created by the NAO in the TNA are larger than those created by the SH IAV in the TSA, and (2) the positive air-sea feedback does not seem to be able to induce an SST anomaly of opposite sign in the TSA.

These findings emphasize the large influence that remote processes have in TAV. However, they also indicate that the positive air-sea thermodynamic feedback is instrumental to "move" the SST anomalies equatorward and create a cross-equatorial SST gradient (which will affect the position and intensity of the ITCZ). In the case of the influence of SH IAV on TAV, this mechanism could be of fundamental importance for enhancing seasonal climate predictability in the tropical Atlantic, since it would allow prediction of SST anomalies several seasons in advance. A number of issues, however, need to be addressed before this potential for prediction can be used in actual forecasts. One of particular interest is:

1. Which are the SST precursor patterns during austral winter-spring that will excite the air-sea feedback in the deep tropics? Our results indicate that SST anomalies in the western side of the basin are very important, because it is on this side that the positive air-sea feedback is present. Is this a model-dependent result? Why is the local positive air-sea feedback localized on the western side

of the basin? *Chang et al.* [2000] argue this is because that is the location of the western Atlantic warm pool where the atmosphere is coupled to the SST and strong convective activity is possible. There, latent heat dominates surface heat flux variability, and the positive feedback occurs between the wind-induced latent heat flux and the SST. The extension of deep convection from the South American continent into the tropical Atlantic may also be a factor. Sensitivity experiments are needed to address this issue.

Besides the local positive air-sea feedback, the tropical Atlantic SST has at least one more source of predictability: the ENSO phenomenon [*Chang et al.*, 2003a]. In Chapter IV we investigated the seasonal predictability of TAV using an AGCM coupled to a mixed layer, a model that incorporates both mechanisms. We developed a methodology to introduce some of the effect of linear ocean dynamics into the slab ocean as an anomalous Q-flux. The objective was to test the importance of ocean dynamics in TAV and improve the prediction of SSTs. Results show that when initialized with global SSTs the corrected coupled system (CPGIC) shows large skill in predicting SSTs in the tropical Atlantic up to six months in advance. The skillful SST prediction translates to a skillful forecast of rainfall in the ITCZ region during boreal spring. In addition, the corrected predictions outperform the non-corrected ones in the ETSA at all lags. These results underscore the importance of ocean dynamics in the predictable dynamics of TAV, and raise the following questions:

1. What ocean dynamical processes are included in the correction? Analyses suggest that the correction represents mainly a parameterization of Ekman dynamics. We hypothesize that an Ekman feedback involving the coupling between surface winds, ocean currents and SST may be present during MAM. A way to test this hypothesis is to include a new term in the equation of the slab ocean

that explicitly calculates the Ekman pumping (the most important term) using the predicted winds at each time step.

What about the ocean processes related to the zonal mode? Although the corrected experiments outperform the non-corrected experiments in predicting the ATL3 index, they are not able to beat persistence before June. Why does the ATL3 persist for so long? Interestingly, the persistence of ATL3 is very large up to May, and afterwards decreases very fast. On the other hand, in the corrected experiments the correlation skill of ATL3 is almost constant from February to August. These results may point to different ocean processes being relevant in the different seasons in the equatorial Atlantic, and the correction parameterizes only some of them. Experiments with ocean GCMs are needed to further address these issues. This investigation will hopefully determine which is the relevant ocean dynamics in TAV in the different seasons, hence guiding the development of future coupled system for dynamical seasonal prediction in the Atlantic basin.

2. The leading EOF of observed SST in the tropical Atlantic during MAM shows significant correlation with tropical Pacific SSTs in the same season. How do ocean basins interact? Can the Atlantic Ocean force Pacific SSTs? How does the ENSO signal interfere with local Atlantic Ocean dynamics?

REFERENCES

Aceituno, P., On the functioning of the Southern Oscillation in the South American sector, Part I, Surface climate, *Mon. Weather Rev.*, *116*, 505–524, 1988.

Allen, M. R., and L. A. Smith, Optimal filtering in singular spectrum analysis, *Phys. Lett.*, *234*, 419–428, 1997.

Anderson, J., H. van den Dool, A. Barnston, W. Chen, W. Stern, and J. Ploshay, Present-day capabilities of numerical and statistical models for atmospheric extratropical seasonal simulation and prediction, *Bull. Am. Meteorol. Soc.*, *80*, 1349–1362, 1999.

Arakawa, A., and W. H. Shubert, Interaction of a cumulus cloud ensemble with the large-scale environment, Part I, *J. Atmos. Sci.*, *31*, 674–701, 1974.

Barnston, A. G., and Coauthors, Long lead seasonal forecasts-where do we stand?, *Bull. Am. Meteorol. Soc.*, *75*, 2097–2114, 1994.

Barreiro, M., P. Chang, and R. Saravanan, Precipitation response to SST forcing and potential predictability in the region of the South Atlantic Convergence Zone, *J. Geophys. Res. (submitted)*, 2003a.

Barreiro, M., A. Giannini, P. Chang, and R. Saravanan, On the role of the Southern Hemisphere atmospheric circulation in Tropical Atlantic Variability, in *Ocean-atmosphere interaction and climate variability (submitted)*, American Geophysical Union, 2003b.

Barsugli, J. J., and D. S. Battisti, The basic effects of atmosphere-ocean thermal coupling on midlatitude variability, *J. Atmos. Sci.*, *55*, 477–493, 1998.

Blade, I., The influence of midlatitude ocean-atmosphere coupling on the low frequency variability of a GCM, Part I: No tropical SST forcing, *J. Clim.*, *10*, 2087–2106, 1997.

Bonan, G. B., The land surface climatology of the NCAR Land Surface Model coupled to the NCAR Community Climate Model, *J. Clim.*, *11*, 1307–1326, 1998.

Bretherton, C. S., C. Smith, and J. M. Wallace, An intercomparison of methods for finding coupled patterns in climate data, *J. Clim.*, *5*, 541–560, 1992.

Cane, M. A., S. E. Zebiak, and C. Dolan, Experimental forecasts of El Niño, *Nature*, *321*, 827–832, 1986.

Carton, J. A., and B. H. Huang, Warm events in the tropical Atlantic, *J. Phys. Oceanogr.*, *24*, 888–903, 1994.

Carton, J. A., X. Cao, B. S. Giese, and M. da Silva, Decadal and interannual SST variability in the tropical Atlantic, *J. Phys. Oceanogr.*, *26*, 1165–1175, 1996.

Chang, P., L. Ji, and H. Li, A decadal climate variation in the tropical Atlantic Ocean from thermodynamic air-sea interactions, *Nature*, *385*, 516–518, 1997.

Chang, P., L. Ji, and R. Saravanan, A hybrid coupled model study of Tropical Atlantic Variability, *J. Clim.*, *14*, 361–390, 2001.

Chang, P., R. Saravanan, and L. Ji, Tropical Atlantic seasonal predictability: The roles of El Niño remote influence and thermodynamic air-sea feedback, *Geophys. Res. Lett.*, *30*, 10.129/2002GL016119, 2003a.

Chang, P., R. Saravanan, L. Ji, and G. Hegerl, The effect of local sea surface temperature on atmospheric circulation over the tropical sector, *J. Clim.*, *13*, 2195–2216, 2000.

Chang, P., R. Saravanan, F. Wang, and L. Ji, Predictability of linear coupled systems. Part II: An application to a simple model of tropical Atlantic variability, *J. Clim. (in press)*, 2003b.

Chiang, J. C. H., Y. Kushnir, and A. Giannini, Deconstructing Atlantic ITCZ variability: Influence of the local cross-equatorial SST gradient, and remote forcing from the eastern equatorial Pacific, *J. Geophys. Res.*, *107*, 1–19, 2002.

Cook, K. H., The South Indian Convergence Zone and interannual rainfall variability over southern Africa, *J. Clim.*, *13*, 3789–3804, 2000.

Curtis, S., and S. Hastenrath, Forcing of anomalous sea surface temperature evolution in the tropical Atlantic during Pacific warm events, *J. Geophys. Res.*, *100*, 15835–15847, 1995.

Czaja, A., P. van der Vaart, and J. Marshall, A diagnostic study of the role of remote forcing in tropical Atlantic variability, *J. Clim.*, *15*, 3280–3290, 2002.

Dommenget, D., and M. Latif, Interannual to decadal variability in the tropical Atlantic, *J. Clim.*, *13*, 777–792, 2000.

Enfield, D. B., and D. A. Mayer, Tropical Atlantic sea surface temperature variability and its relation to El Niño-Southern Oscillation, *J. Geophys. Res.*, *102*, 929–945, 1997.

Figueroa, S. N., P. Satyamurty, and P. L. S. Dias, Simulations of the summer circulation over the South American region with an eta coordinate model, *J. Atmos. Sci.*, *52*, 1573–1584, 1995.

Frankignoul, C., and K. Hasselmann, Stochastic climate models. Part 2: Application to sea-surface temperature anomalies and thermocline variability, *Tellus*,

29, 284–305, 1977.

Giannini, A., J. C. H. Chiang, M. Cane, Y. Kushnir, and R. Seager, The ENSO teleconnection to the tropical Atlantic ocean: Contributions of the remote and local SSTs to rainfall variability in the tropical Americas, *J. Clim.*, *14*, 4530–4544, 2001.

Giannini, A., R. Saravanan, and P. Chang, The preconditioning role of the Tropical Atlantic Variability in the prediction of Nordeste rainfall during ENSO events, *(Manuscript in preparation)*, 2003.

Goddard, L., S. J. Mason, S. E. Zebiak, C. F. Ropelewsky, R. Basher, and M. A. Cane, Current approaches to seasonal-to-interannual climate predictions, *Int. J. Climatol.*, *21*, 1111–1152, 2001.

Gruber, A., X. Su, M. Kanamitsu, and J. Schemm, The comparison of two merged raingauge-satellite precipitation datasets, *Bull. Am. Meteorol. Soc.*, *81*, 2631–2644, 2000.

Hack, J. J., Parameterization of moist convection in the National Center for Atmospheric Research Community Climate Model (CCM2), *J. Geophys. Res.*, *99*, 5551–5568, 1994.

Hasselmann, K., Stochastic climate models: I. Theory, *Tellus*, *28*, 473–485, 1976.

Hasselmann, K., On the signal-to-noise problem in atmospheric response studies, in *Meteorology of the Tropical Oceans*, edited by D. B. Shaw, pp. 251–259, Royal Meteorological Society, Berkshire, UK, 1979.

Hastenrath, S., *Climate and Circulation of the Tropics*, 455 pp., D. Reidel, Boston, 1985.

Hastenrath, S., and L. Greishar, Circulation mechanisms related to northeast Brazil rainfall anomalies, *J. Geophys. Res.*, *98*, 5093–5102, 1993.

Hastenrath, S., and L. Heller, Dynamics of climate hazards in northeast Brazil, *Q. J. R. Meteorol. Soc.*, *103*, 77–92, 1977.

Hess, P. G., D. S. Battisti, and P. J. Rash, Maintenance of the intertropical convergence zones and the large scale tropical circulation on a water-covered Earth, *J. Atmos. Sci.*, *50*, 691–713, 1993.

Hoskins, B. J., and D. J. Karoly, The steady linear response of a spherical atmosphere to thermal and orographic forcing, *J. Atmos. Sci.*, *38*, 1179–1196, 1981.

Huffman, G. J., et al., The Global Precipitation Climatology Project (GPCP) combined precipitation dataset, *Bull. Am. Meteorol. Soc.*, *78*, 5–20, 1997.

Kalnay, E., K. C. Mo, and J. Paegle, Large amplitude, short scale stationary Rossby waves in the Southern Hemisphere: Observations and mechanistics experiments to determine their origin, *J. Atmos. Sci.*, *43*, 252–275, 1986.

Kiehl, J. T., J. Hack, G. B. Bonan, B. P. Boville, D. L. Williamson, and P. J. Rasch, The National Center for Atmospheric Research Community Climate Model: CCM3, *J. Clim.*, *11*, 1131–1149, 1998.

Kiladis, G. N., and K. M. Weickmann, Circulation anomalies associated with tropical convection during northern winter, *Mon. Weather Rev.*, *120*, 1900–1923, 1992.

Kodama, Y.-M., Large scale common features of subtropical convergence zones (the Baiu frontal zone, the SPCZ and the SACZ). Part I: Characteristics of subtropical frontal zones, *J. Meteor. Soc. Japan*, *70*, 813–836, 1992.

Kodama, Y.-M., Large scale common features of subtropical convergence zones (the Baiu frontal zone, the SPCZ and the SACZ). Part II: Conditions of the circulation for generating the STCZs, *J. Meteor. Soc. Japan*, *71*, 581–610, 1993.

Koster, R. D., P. A. Dirmeyer, A. N. Hahmann, R. Ijpelaar, L. Tyahla, P. Cox, and M. J. Suarez, Comparing the degree of land-atmosphere interaction in four atmospheric general circulation models, *J. Hydrometeorol.*, *3*, 363–375, 2002.

Koster, R. D., and M. J. Suarez, Modeling the land surface boundary in climate models as a composite of independent vegetation stands., *J. Geophys. Res.*, *97*, 2697–2716, 1992.

Koster, R. D., and M. J. Suarez, Energy and water balance calculations in the Mosaic LSM, *Tech. Rep. 104606*, 58 pp., National Aeronautics and Space Administration, Greenbelt, MD, 1996.

Koster, R. D., M. J. Suarez, and M. Heiser, Variance and predictability of precipitation at seasonal-to-interannual time scales, *J. Hydrometeorol.*, *1*, 26–64, 2000.

Lamb, P. J., Large-scale tropical Atlantic circulation patterns associated with sub-Saharan weather anomalies, *Tellus*, *30*, 240–251, 1978.

Lau, N.-C., and M. J. Nath, Impact of ENSO on SST variability in the North Pacific and North Atlantic: Seasonal dependence and role of extratropical sea-air coupling, *J. Clim.*, *14*, 2846–2866, 2001.

Lenters, J. D., and K. H. Cook, Simulations and diagnosis of the regional South American precipitation climatology, *J. Clim.*, *8*, 2988–3005, 1995.

Levitus, S., World ocean atlas CD-ROM data sets, National Oceanographic Data Center Ocean Climate Laboratory, 1994.

Liebmann, B., G. N. Kiladis, J. A. Marengo, T. Ambrizzi, and J. D. Glick, Submonthly convective variability over South America and the South Atlantic convergence zone, *J. Clim.*, *12*, 1877–1891, 1999.

Lindzen, R. S., and S. Nigam, On the role of sea surface temperature gradients in forcing low level winds and convergence in the tropics, *J. Atmos. Sci.*, *44*, 2418–2436, 1987.

Lorenz, E. N., Deterministic nonperiodic flow, *J. Atmos. Sci.*, *20*, 130–141, 1963.

Marshall, J., Y. Kushnir, D. Battisti, P. Chang, A. Czaja et al., North Atlantic climate variability: Phenomena, impacts and mechanisms, *Int. J. Climatol.*, *21*, 1863–1898, 2001.

Matthews, A. J., and G. N. Kiladis, Interaction between ENSO, transient circulation, and tropical convection over the Pacific, *J. Clim.*, *12*, 3062–3086, 1999.

Moorthi, S., and M. J. Suarez, Relaxed Arakawa-Shubert: A parameterization of moist convection for general circulation models, *Mon. Weather Rev.*, *120*, 978–1002, 1992.

National Research Council, *Decade-to-Century-Scale Climate Variability and Change: A Science Strategy*, 142 pp., Panel on Climate Variability on Decade-to-Century Time Scales, National Academy Press, Washington, D.C., 1998.

Neelin, J. D., The slow sea surface temperature mode and the fast-wave limit: Analytic theory for tropical interannual oscillations and experiments in a hybrid coupled model, *J. Clim.*, *48*, 584–606, 1991.

Neelin, J. D., D. S. Battisti, A. C. Hirst, F.-F. Jin, T. Yamagata, and S. Zebiak, Enso theory, *J. Geophys. Res.*, *103*, 14261–14290, 1998.

Nobre, P., and J. Shukla, Variations of sea surface temperature, wind stress, and rainfall over the tropical Atlantic and South America, *J. Clim.*, *9*, 2464–2479, 1996.

North, G. R., T. L. Bell, R. F. Cahalan, and F. J. Moeng, Sampling errors in the estimation of empirical orthogonal functions, *Mon. Weather Rev.*, *110*, 699–706, 1982.

Paegle, J. N., L. A. Byerle, and K. C. Mo, Intraseasonal modulation of South American summer precipitation, *Mon. Weather Rev.*, *128*, 837–850, 2000.

Peixoto, J. P., and A. H. Oort, *Physics of Climate*, 520 pp., American Institute of Physics, New York, 1992.

Penland, C., and P. Sardesmukh, The optimal growth of tropical sea surface temperature anomalies, *J. Clim.*, *8*, 1999–2024, 1995.

Philander, S. G. H., *El Niño, La Niña, and the Southern Oscillation*, 293 pp., Academic Press, San Diego, CA, 1990.

Rayner, N. A., E. B. Horton, D. E. Parker, C. K. Folland, and R. B. Hackett, Version 2.2 of the Global Sea-Ice and sea surface temperature data set, 1931-1994, *Tech. Rep. 74*, Hadley Centre, Meteorological Office, United Kingdom, 1996.

Reynolds, R. W., and T. M. Smith, Improved global sea surface temperature analyzes using optimum interpolation, *J. Clim.*, *7*, 929–948, 1994.

Robertson, A. W., and C. Mechoso, Interannual and decadal variability of the South Atlantic Convergence Zone, *Mon. Weather Rev.*, *128*, 2947–2957, 2000.

Robertson, A. W., C. Mechoso, and Y.-J. Kim, The influence of Atlantic sea-surface temperature anomalies on the North Atlantic Oscillation, *J. Clim.*, *13*, 122–138, 1999.

Rowell, D. P., Assessing potential seasonal predictability with an ensemble of multidecadal GCM simulations, *J. Clim.*, *11*, 109–120, 1998.

Ruiz-Barradas, A., J. A. Carton, and S. Nigam, Structure of interannual-to-decadal climate variability in the tropical Atlantic sector, *J. Clim.*, *13*, 3285–3297, 2000.

Saravanan, R., Atmospheric low frequency variability and its relationship to midlatitude SST variability: studies using the NCAR Climate System Model, *J. Clim.*, *11*, 1386–1404, 1998.

Saravanan, R., and P. Chang, Interaction between tropical Atlantic variability and El Niño-Southern Oscillation, *J. Clim.*, *13*, 2177–2194, 2000.

Satyamurty, P., C. A. Nobre, and P. L. S. Dias, South America, in *Meteorology of the Southern Hemisphere, Meteorol. Monog.*, pp. 119–139, Amer. Meteor. Soc., Boston, 1998.

Schneider, T., and S. M. Griffies, A conceptual framework for predictability studies, *J. Clim.*, *12*, 3133–3155, 1999.

Seager, R., Y. Kushnir, P. Chang, N. Naik, J. Miller, and W. Hazeleger, Looking for the role of the ocean in tropical Atlantic decadal climate variability, *J. Clim.*, *14*, 638–655, 2001.

Seager, R., Y. Kushnir, M. Visbeck, N. Naik, J. Miller, G. Krahmann, and H. Gullen, Causes of Atlantic Ocean climate variability between 1958 and 1998, *J. Clim.*, *13*, 2845–2862, 2000.

Smith, T. M., R. W. Reynolds, R. E. Livezey, and D. C. Stokes, Reconstruction of historical sea surface temperatures using empirical orthogonal functions, *J. Clim.*, *9*, 1403–1420, 1996.

Sterl, A., and W. Hazeleger, Coupled variability and air-sea interaction in the South Atlantic Ocean, *(Submitted to Clim. Dyn.)*, 2003.

Suarez, M. J., and L. L. Takacs, Documentation of the ARIES/GEOS dynamical core: version 2, *Tech. Rep. 104606*, National Aeronautics and Space Administration, Greenbelt, MD, 1995.

Tanimoto, Y., and S.-P. Xie, Inter-hemispheric decadal variations in SST, surface wind, heat flux and cloud cover over the Atlantic Ocean, *J. Meoteor. Soc. Japan*, *80*, 1199–1219, 2002.

Thompson, D. W. J., and J. M. Wallace, The Arctic Oscillation signature in the wintertime geopotential height and temperature fields, *Geophys. Res. Lett.*, *25*, 1297–1300, 1998.

Venegas, S. A., L. A. Mysak, and N. Straub, Atmosphere-ocean coupled variability in the South Atlantic, *J. Clim.*, *10*, 2904–2920, 1997.

Venzke, S., M. Allen, R. Sutton, and D. Rowell, The atmospheric response over the North Atlantic to decadal changes in sea surface temperature, *J. Clim.*, *12*, 2562–2584, 1999.

Visbeck, M., H. Cullen, G. Krahmann, and N. Naik, An ocean model's response to North Atlantic Oscillation-like wind forcing, *Geophys. Res. Lett.*, *25*, 4521–4524, 1998.

von Storch, H., and F. W. Zwiers, *Statistical Analysis in Climate Research*, 484 pp., Cambridge University Press, New York, 1999.

Wang, B., and T. Li, A simple model of relevance to short-term climate variations, *J. Atmos. Sci.*, *50*, 260–284, 1993.

Xie, P., and P. A. Arkin, Analyses of global monthly precipitation using gauge observations, satellite estimates, and numerical model predictions, *J. Clim.*, *9*, 840–858, 1996.

Xie, S.-P., A dynamic ocean-atmosphere model of the tropical Atlantic decadal variability, *J. Clim.*, *12*, 64–70, 1999.

Zebiak, S. E., Air-sea interaction in the equatorial Atlantic region, *J. Clim.*, *6*, 1567–1586, 1993.

Zebiak, S. E., and M. Cane, A model El Niño-Southern Oscillation, *Mon. Weather Rev.*, *115*, 2262–2278, 1987.

Zhang, G. J., and N. A. McFarlane, Sensitivity of climate simulations to the parameterization of cumulus convection in the Canadian Climate Centre general circulation model, *Atmos.-Ocean*, *33*, 407–446, 1995.

APPENDIX A

PREDICTABILITY AND SIGNAL DETECTION

1. Types of predictability problems

There are two types of predictability problems. Predictability studies of the first kind address how the uncertainties in an initial state of the climate system affect the prediction of a later state. For example, in weather forecasting the error in the initial state amplifies with time limiting the useful predictability to about two weeks. Because of the inability to forecast individual weather events beyond this limit, the goal of climate forecasting is to predict the statistical properties of weather. The first order factor in the first kind of predictability of climate is the specification of the initial state of the ocean, which may provide "memory" to the system. Other factors such as soil moisture and snow cover may also be important. Predictability studies of the second kind address the predictability of the climate system to changes in boundary conditions. Predictability of the second kind does not depend on the initial conditions. In this case, the predictability is limited by the fact that the boundary conditions do not uniquely determine the climate. For example, given a configuration of sea surface temperatures, the internal atmospheric variability renders a multitude of atmospheric states that are consistent with it. An SST anomaly results in a predictable atmospheric response only if it reduces the uncertainty as to which a certain atmospheric state may occur to less than the climatological uncertainty [*Schneider and Griffies*, 1999]. This is particularly true in the tropics where the

*Portions of this appendix are reprinted with permission from the lecture *Predictability and detection problems*, by R. Sutton, National Center for Atmospheric Research Summer Colloquium 2000. Available at http://www.asp.ucar.edu/colloquium/2000/lecturesTOC.html

atmosphere is strongly coupled to the ocean, and SST anomalies are able to induce an atmospheric response. Both kinds of predictability studies require of a model to provide a prediction.

But, how can we define predictability? Predictability is concerned with the reduction of uncertainties, in other words, we hope that our prediction will tell us more than we already knew. We must therefore ask to what extent does a forecast reduce our uncertainty? To answer that question we need to define a quantitative measure that compares our knowledge before (prior uncertainty) and after the forecast (posterior uncertainty).

For Gaussian systems the standard deviation, σ, is the appropriate measure of uncertainty. Assume x is a univariate gaussian variable. Then, if x_f is an unbiased forecast of x with error $e = x - x_f$, then $< e >= 0$ and the uncertainty is $\sigma_f = \sqrt{< e^2 >}$ ("<>" denote mean). The prior knowledge is usually the climatological mean with associated uncertainty σ_c. Following *Schneider and Griffies* [1999] the predictive power of the forecast can be defined as

$$Predictive\ Power = 1 - \frac{\sigma_f}{\sigma_c}. \tag{A.1}$$

Thus, the smaller the posterior uncertainty (σ_f) the larger the predictive power. A perfect forecast has $\sigma_f = 0$, while the climatological mean forecast has $\sigma_f = \sigma_c$. A more general definition of the predictive power for multivariate and non-gaussian systems can be found in *Schneider and Griffies* [1999].

2. Predictability of the first kind

The evolution of the system can be represented by a trajectory in the phase space. Then, the growth of forecast errors is related to the divergence of initially close trajectories. Chaotic systems, like the extratropical atmosphere, exhibit sensitivity

to initial conditions that leads to forecasting errors growing exponentially with lead time.

To make a prediction of the first kind two things are needed: knowledge of the current state of the system, and a model. Since observations provide an uncertain estimate of the current state, we can locate the system only within some finite region of the phase space. Thus, the initial condition is not uniquely determined. The best way to circumvent this difficulty is to make several predictions starting from very close but different initial conditions. This is called an ensemble forecast. As result, the ensemble forecast produces an ensemble of states that form a sample of the distribution representing uncertainties in the prediction at different lead times.

On seasonal-to-interannual time scales the initial state of the ocean is fundamental in determining the evolution of the climate system. This is because the ocean varies on longer time scales than the atmosphere, thus providing the memory to the coupled system. In the tropics coupled ocean-atmosphere interactions can amplify initial anomalies, and produce large spatially coherent SST anomalies that will force the atmosphere. Examples of ocean-atmosphere coupling are those characteristic of ENSO in the Pacific [*Philander*, 1990], and the thermodynamic air-sea interaction in the Atlantic [*Chang et al.*, 1997]. The result of the atmosphere-ocean coupling is a climatic signal that can be predicted several seasons in advance [*Goddard et al.*, 2001]. To detect the signal, and therefore the predictable part of the evolution of the climate system, the ensemble mean of an ensemble forecast is calculated. The ensemble mean is usually considered the best climate prediction because it averages over the many possible initial states and filters out the noise always present in the system. If the system is linear, and in the hypothetical case of an infinite ensemble, the ensemble mean will only contain the evolution of the coupled signal. A measure of the uncertainty of the prediction is given by the spread of the ensemble members

around the mean.

3. Predictability of the second kind and detection of the climate response to external forcing

Consider a covariance stationary climate. Then, its statistics do not depend on the initial conditions, and are entirely determined by the boundary conditions and the laws of physics. Hence, we can express the climate statistics c as a function of some external parameters:

$$c = f(external\ parameters)$$

The parameters may correspond to physical variables like SST, or model variables. The problem of understanding climate, can then be viewed as the determination of the function f.

a. Time independent problem

Consider two climate model simulations which differ only in the value of a single external parameter α

$$c_1 = f(..., \alpha_1)$$
$$c_2 = f(..., \alpha_2)$$

To identify any response we must determine how precisely the statistic of interest can be estimated. Or, similarly, how much data do we need to achieve a desired level of confidence?

For gaussian variables the response to changes in external parameters can be of three types: a change in the mean, a change in the variance, or a change in both of these two quantities. For non-gaussian variables the response may also consist in

introducing a bias in the possible regimes, thus favoring some regimes against others. Here we will consider changes in the mean, but other statistics of the response may also be of importance.

Consider an univariate random variable x with (unknown) mean value $\mathbf{x}$ and variance σ^2. Suppose we take n measurements x_i, $i = 1...n$. The sample mean, $\bar{x}$, is an unbiased estimate of $\mathbf{x}$. The expected error in the calculation of the mean, σ_m can be estimated as follows

$$\hat{\sigma}_m^2 = \frac{1}{n}\hat{\sigma}^2 = \frac{1}{n(n-1)}\sum_{i=1}^{n}(x_i - \bar{x})^2 \tag{A.2}$$

where $\hat{\sigma}^2$ is an estimate of the population variance (the "hat" denotes estimated quantities).

Suppose now that some variable x in climates c_1 and c_2 has mean values $\mathbf{x_1}$ and $\mathbf{x_2}$, and the same variance σ^2. To detect a change in the mean value of x we require that the ratio $\frac{\bar{x}_2 - \bar{x}_1}{\hat{\sigma}_m}$ be above a certain threshold. A student's t-test can be used to assess statistical significance. Note that $\hat{\sigma}_m$ depends on the sample size n. Therefore, the more data we have the weaker the signal we can detect at a given level of confidence.

The ratio defined above is not an intrinsic property of the system because it depends on sample size. Instead, we can define the signal-to-noise ratio, which is a physical measure of signal strength, and can be estimated as $\frac{\bar{x}_2 - \bar{x}_1}{\hat{\sigma}}$.

b. Time dependent problem

i. Signal-to-noise optimization technique

In this section we present a methodology for characterizing the time-varying response to a time-varying external forcing in a system subject to internal chaotic dynamics. The technique is a signal-to-noise optimization procedure developed by

Venzke et al. [1999] and *Allen and Smith* [1997].

We define the forced response to a time-varying external forcing (here, SST) as the component of the evolution of the system that is independent of the initial conditions and is therefore common to all members of a hypothetical infinite ensemble. We assume that on the time scales of interest the evolution of the system can be considered as a linear superposition of the forced signal and the internal variability. Interaction between the two components is not considered. The methodology also assumes that variables have gaussian distributions.

In this work we apply this technique mainly to AMIP-type of simulations. In these experiments the SST is imposed, but the land surface interacts freely with the atmosphere. Thus, the internal part includes internal atmospheric variability as well as variability of the land surface and its effects on the atmosphere. The external signal is due to SST forcing alone. During this study we will usually refer the internal variability as atmospheric internal variability. However, it is important to keep in mind that is also includes land-atmosphere interaction.

Suppose we construct a K-member ensemble of model simulations using an AGCM forced with observed time-varying SST. Let $\vec{x}$ be a state vector of dimension m and X a mxn matrix describing the evolution of $\vec{x}$ (the index $n = 1...N$ denotes time). Due to the linearity assumption we can write for each ensemble member k

$$X^k = X_F + X_N^k \qquad\qquad k = 1...K. \tag{A.3}$$

The forced atmospheric response X_F to SST forcing is assumed to be the same for all ensemble members, while the internal atmospheric variability denoted as X_N^k is different for all members. The ensemble mean X_M is

$$X_M = \frac{1}{K}\sum_{k=1}^{K} X^k = X_F + \frac{1}{K}\sum_{k=1}^{K} X_N^k. \tag{A.4}$$

Although the actual realizations of the internal variability (or noise) are different for all members, their statistics are assumed to be the same. Here we consider that the internal variability is white in time. Since the noise is by definition independent of the forced signal we can write

$$C_M = C_F + \frac{C_N}{K}, \tag{A.5}$$

where C_M is the covariance matrix of the ensemble mean, C_F is the covariance matrix of the forced signal, and C_N is the covariance matrix of the noise. The latter can be estimated as the covariance matrix of the deviations of the ensemble members respect to the ensemble mean. Alternatively, C_N can be estimated from the output of an atmospheric GCM forced with climatological SSTs.

An EOF analysis can be applied on C_M. But, are the eigenvectors of C_M equal to the eigenvectors of C_F? Suppose $\vec{v}$ is an eigenvector of C_F with eigenvalue λ_F. Then,

$$C_M\vec{v} = C_F\vec{v} + \frac{C_N}{K}\vec{v} = \lambda_F\vec{v} + \frac{C_N}{K}\vec{v}. \tag{A.6}$$

If and only if the noise is white in space, that is $C_N = K\sigma_N^2 I$, then $C_M\vec{v} = (\lambda_F + \sigma_N^2)\vec{v}$, and $\vec{v}$ is an eigenvector of C_M. In reality, the internal atmospheric variability is highly correlated in space and therefore the EOFs are strongly influenced by the noise. The main idea behind the technique presented below is the use of the information about the spatial structure of the noise to calculate a more accurate representation of the forced signal.

The objective of the signal-to-noise optimization procedure is to find a vector $\vec{S}$ such that the variance of the forced response along $\vec{S}$ is maximized relative to the noise variance along the same direction. Hence, we need $\vec{S}$ such that the signal-to-noise ratio $\frac{\sigma_F^2}{\sigma_N^2}$ is maximum. But, using (A.5), $\frac{\sigma_M^2}{\sigma_N^2} = \frac{\sigma_F^2}{\sigma_N^2} + \frac{1}{K}$. Thus, given K, maximizing

$\frac{\sigma_F^2}{\sigma_N^2}$ is equivalent to maximizing $\frac{\sigma_M^2}{\sigma_N^2}$.

Let F be such that $F^t C_N F = KI$ ("t" denotes transpose of a matrix). F is a "pre-whitening" filter, which removes the spatial correlations making the noise spatially white (it was assumed temporally white already). The covariance matrix of the noise can be written

$$C_N = \sqrt{K}(F^t)^{-1}\sqrt{K}F^{-1}, \tag{A.7}$$

and

$$\vec{S}^t C_N \vec{S} = \sqrt{K}\vec{S}^t(F^{-1})^t\sqrt{K}F^{-1}\vec{S} = \sqrt{K}(F^{-1}\vec{S})^t(F^{-1}\vec{S})\sqrt{K} = K\vec{S'}^t\vec{S'}, \tag{A.8}$$

where $\vec{S'} = F^{-1}\vec{S}$. Also,

$$\vec{S}^t C_M \vec{S} = (F\vec{S'})^t C_M F\vec{S'} = \vec{S'}^t F^t C_M F\vec{S'}. \tag{A.9}$$

Using Eqns. A.8 and A.9 the S/N ratio to maximize can be expressed as

$$\frac{\sigma_M^2}{\sigma_N^2} = \frac{\vec{S}^t C_M \vec{S}}{\vec{S}^t C_N \vec{S}} = \frac{\vec{S'}^t F^t C_M F\vec{S'}}{K\vec{S'}^t\vec{S'}} = \frac{\vec{S'}^t C'_M\vec{S'}}{K\vec{S'}^t\vec{S'}} = R(\vec{S'}). \tag{A.10}$$

Matrix $C'_M = F^t C_M F$ is the pre-whitened covariance matrix of the ensemble mean. Equation (A.10) is a Rayleigh quotient ($R(\vec{S'})$), and its stationary points can be obtained by taking its gradient respect to $\vec{S'}$ and equate to zero. Since

$$\frac{\partial(\vec{S'}^t\vec{S'})}{\partial\vec{S'}} = 2\vec{S'}, \tag{A.11}$$

$$\frac{\partial(\vec{S'}^t C_M\vec{S'})}{\partial\vec{S'}} = 2C'_M\vec{S'}, \tag{A.12}$$

we have that $\frac{\partial R}{\partial\vec{S'}} = 0$ only if

$$C'_M\vec{S'} - \frac{\vec{S'}^t C'_M\vec{S'}}{\vec{S'}^t\vec{S'}}\vec{S'} = 0. \tag{A.13}$$

Equation (A.13) states that in order to maximize the Rayleigh quotient we need

to find the largest eigenvalue of the system $C'_M\vec{S'} = \lambda\vec{S'}$. Transforming back to the original non-prewhitened space we get

$$\begin{aligned} C'_M\vec{S'} = \lambda\vec{S'} \Leftrightarrow \\ F^t C_M F\vec{S'} = \lambda\vec{S'} \Leftrightarrow \\ C_M F\vec{S'} = \lambda(F^t)^{-1}\vec{S'} \Leftrightarrow \\ C_M\vec{S} = \lambda(F^t)^{-1}F^{-1}\vec{S} = \lambda\frac{C_N}{K}\vec{S}. \end{aligned} \tag{A.14}$$

Thus solving for the largest eigenvalue of the eigenproblem

$$C_M\vec{S} = \frac{\lambda}{K}C_N\vec{S} \tag{A.15}$$

gives the direction $\vec{S}$ in phase space that defines the pattern which maximizes the S/N ratio of equation (A.10). Along $\vec{S}$ the S/N ratio is $\frac{\sigma_M^2}{\sigma_N^2} = \frac{\lambda}{K}$. In *Venzke et al.* [1999] $\vec{S}$ is called a "spatial filter" because it provides the optimal filter to discriminate between the forced response and the internal atmospheric variability. In the original derivation of the algorithm by *Venzke et al.* [1999], the technique was not posed as the solution of an eigenvalue problem. It required the explicit construction of the "pre-whitening" filter F previous to the finding of $\vec{S}$. We followed this procedure in section D of Chapter II. The construction of the matrix F poses some complications because we have to decide the number of noise EOFs used to construct it (see also *Venzke et al.* [1999]). Therefore, during the rest of our work we used (A.15) to find the spatial filters $\vec{S}$ because it does not require of the intermediate step of finding F and is more straightforward to use. Both procedures yield, however, same results.

The set of eigenvectors $\vec{S}$ is generally not orthogonal. Instead, the $\vec{S}$ are orthogonal with respect to C_N, that is $\vec{S}_i C_N \vec{S}_j = 0$ if $i \neq j$. This is equivalent to say that $\vec{y} = C_N\vec{S}$ and $\vec{S}$ are biorthogonal. The vectors $\vec{y}$ are the physical patterns

(besides a constant): applying an inverse pre-whitening on $\vec{S}'$ we get $\vec{p} = (F^t)^{-1}\vec{S}' = (F^t)^{-1}F^{-1}\vec{S} = \frac{C_N}{K}\vec{S}$. Or equivalently from equation (A.15) the physical patterns associated to a particular filter $\vec{S}$ can be calculated as $\vec{p} = \frac{1}{\lambda}C_M\vec{S}$. The physical patterns are usually called S/N-optimals. The time series associated to the S/N-optimals are calculated as $pc = \vec{S}^t X_M$.

If C_N is non-singular then the generalized eigenvalue problem of equation (A.15) can be reduced to $KC_N^{-1}C_M\vec{S} = \lambda\vec{S}$, which is a regular eigenvalue problem. If C_N is singular the solution is to do a regularization by truncated principal components: set to zero the eigenvalues not significantly different from zero and their inverses. Zeroing these contributions to the inverse of C_N amounts to replacing the ill-defined inverse C_N^{-1} by a Moore-Penrose pseudo-inverse (see *Schneider and Griffies* [1999]).

Once the S/N-optimals are calculated, there are two ways to proceed. The first straightforward way is considering the leading S/N-optimals as the forced signals.

A second way, which may be physically more sound, consists of two steps. First, construct a total forced signal by summing up all the optimals that have a S/N-ratio larger than unity. (Note that by construction the mean S/N-ratio of individual noise realizations in ensemble members -the noise-to-noise ratio- is unity. However, due to limited sampling this is not true for individual noise realizations and an interval of confidence around unity can be constructed for each optimal given by the dispersion of the noise-to-noise ratios. The signal was constructed using those optimals that have S/N-ratios lying outside this interval.) Second, the dominant forced patterns are calculated as the EOFs of the total signal variance. This method is preferred because the optimization method does not assure a priory that the first optimal is the pattern that explains the most signal variance. Theoretically, it may happen that the first optimal is a pattern that seldom occurs (then a small signal variance), but it is a pattern that is nearly orthogonal to the noise, thus giving a large S/N-ratio.

By constructing the total signal variance and then performing an EOF analysis, we assure that the pattern is the one that explains most of the signal variance. We used both ways to find the forced responses. Our results indicate that the first EOF of the total signal and the first optimal are in fact very similar in both spatial and temporal structures for the data sets we have considered.

Since the constructed signal is by definition common to all ensemble members, it is possible to construct the noise part of the model evolution by subtracting the signal from each ensemble member. The spatial structure of the dominant internal mode can then be found by performing an EOF analysis on the noise variance.

Moreover, by comparing the relative strength of the signal (σ_s^2) and of the noise (σ_n^2) variance, one can also obtain an estimate of potential predictability. To do so, we define a potential predictability measure PP as the ratio between signal variance and total variance, i.e., $PP = \sigma_s^2/(\sigma_s^2 + \sigma_n^2) = \sigma_s^2/\sigma_t^2$, where σ_t^2 is the total variance. It is important to realize that the word "potential" means that the model is assumed perfect and that the surface state of the ocean is known in advance. Thus, potential predictability gives an upper limit of the predictability of the atmospheric response to changes in SST.

In sum, the signal-to-noise optimization procedure is a powerful tool that allows the separate study of the forced response and the noise, under the assumption of linearity, in a systematic way.

ii. Analysis of Variance

The Analysis of Variance (ANOVA) provides a second method to estimate potential predictability. Here we only give a brief summary of ANOVA. A detailed description of the technique can be found in *Rowell* [1998] and *von Storch and Zwiers* [1999].

Consider a K-member ensemble of AMIP-type simulations as in the previous section. The ANOVA model assumes that the simulated evolution of an atmospheric variable at each grid point can be approximated as the sum of two independent components:

$$x_{nk} = \mu_n + \epsilon_{nk}, \quad k = 1...K, \;\; n = 1...N. \tag{A.16}$$

where μ_n is the component due to ocean forcing and ϵ_{nk} is the component due to internal variability. This is called a 1-way ANOVA model. The assumptions are: (1) ϵ_{nk} are independent and identically distributed normal random variables with zero mean and variance σ_N^2, and (2) μ_n are independent and identically distributed normal random variables with zero mean and variance σ_F^2.

The variance of the internal variability can be estimated by computing the deviations from the ensemble mean

$$\hat{\sigma}_N^2 = \frac{1}{N(K-1)} \sum_{n=1}^{N} \sum_{k=1}^{K} (x_{nk} - \bar{x}_n)^2, \tag{A.17}$$

where

$$\bar{x}_n = \frac{1}{K} \sum_{k=1}^{K} x_{nk}, \tag{A.18}$$

is the ensemble mean. The variance of the ensemble mean is in turn estimated as

$$\hat{\sigma}_{EM}^2 = \frac{1}{N-1} \sum_{n=1}^{N} (\bar{x}_n - x)^2, \tag{A.19}$$

where

$$x = \frac{1}{NK} \sum_{k=1}^{K} \sum_{n=1}^{N} x_{nk}, \tag{A.20}$$

is the mean over all the data. Now, as in the previous chapter we can write

$$\sigma_{EM}^2 = \sigma_F^2 + \frac{\sigma_N^2}{K}, \tag{A.21}$$

which states that the variance of the ensemble mean is a biased estimate of the

signal variance. The variance due to the ocean forcing can thus be estimated as $\hat{\sigma}_F^2 = \hat{\sigma}_{EM}^2 - \frac{\hat{\sigma}_N^2}{K}$, while the total variance is estimated as $\hat{\sigma}_T^2 = \hat{\sigma}_F^2 + \hat{\sigma}_N^2$. The potential predictability can then be computed as the ratio $PP_A = \frac{\hat{\sigma}_F^2}{\hat{\sigma}_T^2}$. Note that if SSTs are assumed to be known in advance this ratio is analogous to the predictive power.

Next, we show how to compute the statistical significance of the potential predictability. A test to measure if there are significant SST effects can be posed as follows:

The hypothesis of no SST effects is $H_0 : \sigma_F^2 = 0$.

The alternative hypothesis is $H_a : \sigma_F^2 > 0$.

Thus, from equation A.21 the F-ratio $F = \frac{\hat{\sigma}_{EM}^2}{\hat{\sigma}_N^2/K}$ is a suitable statistics to test H_0. It can be shown that F follows an F-distribution with $(N-1, N(K-1))$ degrees of freedom. Using the F-ratio we can rewrite PP_A

$$PP_A = \frac{F-1}{F+(K-1)}, \tag{A.22}$$

and critical values of F can be used to assess the statistical significance of ANOVA's estimate of potential predictability.

APPENDIX B

DERIVATION OF SST EQUATION

We follow *Penland and Sardesmukh* [1995] to derive equations (4.1)-(4.3). Let $\mathbf{X_a}$ represent the state vector of the atmosphere. The evolution of $\mathbf{X_a}$ is given by $\frac{\partial \mathbf{X_a}}{\partial t} = f(\mathbf{X_a}, T)$, where $f(\mathbf{X_a}, T)$ is a nonlinear function, and T represents the SST. Linearizing the equation around the climatology $(\bar{\mathbf{X}}_\mathbf{a}, \bar{T})$, the equation for the anomalies $\mathbf{X}'_\mathbf{a}$ may be written

$$\frac{\partial \mathbf{X}'_\mathbf{a}}{\partial t} = \left.\frac{\partial f}{\partial \mathbf{X}'_\mathbf{a}}\right|_{\bar{\mathbf{X}}_\mathbf{a}} \mathbf{X}'_\mathbf{a} + \left.\frac{\partial f}{\partial T}\right|_{\bar{T}} T' + N_a = L_a \mathbf{X}'_\mathbf{a} + L_o T' + N_a \tag{B.1}$$

On the time scales of SST evolution the atmosphere adjusts quickly to SST changes, therefore $\frac{\partial \mathbf{X}'_\mathbf{a}}{\partial t} = 0$, and the atmospheric variability can be divided into a quasi-equilibrium response to SST changes, and a quasi-random part due to nonlinear processes (N_a)

$$\mathbf{X}'_\mathbf{a} = -(L_a^{-1} L_o) T' - L_a^{-1} N_a \tag{B.2}$$

Now, the evolution equation for the SST is (neglecting the small diffusion term)

$$\frac{\partial T}{\partial t} = -u\frac{\partial T}{\partial x} - v\frac{\partial T}{\partial y} - w\frac{\partial T}{\partial z} + Q \tag{B.3}$$

We assume that the net surface heat flux Q can be written as a linear function of the air-sea temperature difference, that is, $Q = L_q(T_a - T)$, where T_a is the atmospheric temperature. Then, using equation (B.2), the anomalous heat flux Q' can be expressed as the sum of a linear term depending on the SST alone, and a term that is due to nonlinear processes that are approximated as white noise: $Q' = AT' + Q_N$. Note that matrix A depends not only on the local SST but also on winds that adjust to SST gradients.

We now look into the advective terms of the SST equation. The vertical derivative in equation (B.3) can be simplified as $\partial T/\partial z = (T - (T_S + \Gamma h))/H$, where H is a characteristic depth, h is the thermocline displacement, T_S a characteristic temperature that would that would be upwelled from a thermocline undisturbed by dynamics and Γ a positive constant [*Neelin*, 1991]. Linearizing the SST equation about the climatology we get

$$\frac{\partial T'}{\partial t} = -\bar{u}\frac{\partial T'}{\partial x} - \bar{v}\frac{\partial T'}{\partial y} - \bar{w}\frac{T'}{H} + Q' - u'\frac{\partial \bar{T}}{\partial x} - v'\frac{\partial \bar{T}}{\partial y} - w'\frac{\partial \bar{T}}{\partial z} + \bar{w}\frac{\Gamma h}{H} + N_o, \quad \text{(B.4)}$$

where N_o are nonlinear terms. The first three terms on the right hand side of equation (B.4) are of the form of a matrix B_1 operating on the SST anomaly. Note that matrix B_1 involves spatial derivatives. If the anomalous currents and thermocline depth evolve in response to the anomalous winds, then the remaining linear terms of equation (B.4) can be written as a matrix operating on the winds. But the winds are themselves a response to the SST (equation (B.2)). Thus, these terms can be written as a matrix B_2 operating on the SST. Then, equation (B.4) becomes analogous to equation (4.1)-(4.3)

$$\frac{\partial T'}{\partial t} = AT' + B_1T' + B_2T' + \xi = AT' + BT' + \xi = \hat{A}T' + \xi, \quad \text{(B.5)}$$

where the nonlinear terms have been approximated as gaussian white noise ξ. Equation (B.5) states that the evolution of SSTs is governed by a multivariate linear Markov process. The matrix $B = B_1 + B_2$ parameterizes the effects of the advective terms in the evolution of the SST anomaly. Matrix $\hat{A}$ includes both thermodynamical and dynamical ocean processes affecting the SST evolution.

VITA

Marcelo Barreiro was born in Montevideo, Uruguay, on August 14, 1971. He received his B.S. degree in physics in 1994, and his M.S. degree in physics in 1998, both from the University of the Republic, Uruguay. In January 1999 he went to Texas A&M University to pursue a Ph.D. in oceanography with special interest in climate studies. He received his Ph.D. in December 2003.

He can be reached at Av. Dr. Francisco Soca 1375, Montevideo 11300, Uruguay.